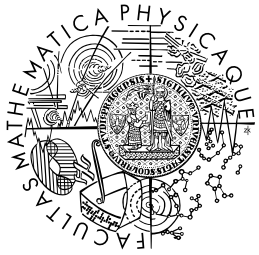

FACULTY
OF MATHEMATICS
AND PHYSICS
Charles University

DOCTORAL THESIS

Mgr. Nicola Burianová

Use of reactors and quasi-monoenergetic neutron sources in the study of reaction cross-sections important for advanced nuclear systems

Institute of Nuclear and Particle Physics

Supervisor of the doctoral thesis: RNDr. Vladimír Wagner, CSc.
Study programme: Particle and Nuclear Physics
Study branch: P4F9

Prague 2024

I declare that I carried out this doctoral thesis independently, and only with the cited sources, literature and other professional sources. It has not been used to obtain another or the same degree.

I understand that my work relates to the rights and obligations under the Act No. 121/2000 Sb., the Copyright Act, as amended, in particular the fact that the Charles University has the right to conclude a license agreement on the use of this work as a school work pursuant to Section 60 subsection 1 of the Copyright Act.

In Prague date ....

Mgr. Nicola Burianová

Since my family comes first, I would like to thank them first. Many thanks go to my grandfather, Ladislav, who is unfortunately no longer alive. He always supported me in physics from my early childhood. He also supported me financially during my studies at the MFF and he hoped that one day there will be a PhD in his family. Unfortunately, he did not live to see this reality, but although I went through a difficult period of time during my studies when I wanted to give it up and I did not think that one day I would actually finish the doctorate, it is now becoming a reality.

I would also like to thank my mother, Iveta, who also supported me not only financially, but especially morally. Thank you for raising me to be the person I am today. My thanks also go to my two younger brothers, Jiří and Tomáš, without their help I could not have imagined it either. Of course, my thanks also go to my grandmother, Marie, and also to my dog Atom, who welcomes me at home from work every day with sincere love and gives me the positive energy.

I would like to thank all my colleagues who worked with me and participated in the preparation of this thesis, all the teachers who taught me at the MFF and thus passed on their valuable knowledge to me. I thank my supervisor, RNDr. Vladimír Wagner, CSc., for his professional guidance and patience.

Last but not least, I would like to thank to my closest friends - Honza, Nela, Martin, Martin, Radek, Jakub, Kristýna, Jitka, Carlos and Bára, whose help was also very essential on my study journey, which was completed by this doctoral thesis.

Finally, I would like to place my favorite quote here:

"Be a hard master to yourself – and be lenient to everybody else."
— Henry Ward Beecher

Title: Use of reactors and quasi-monoenergetic neutron sources in the study of reaction cross-sections important for advanced nuclear systems

Author: Mgr. Nicola Burianová

Institute: Institute of Nuclear and Particle Physics

Supervisor: RNDr. Vladimír Wagner, CSc., Nuclear Physics Institute of the CAS

Abstract: Measurement of effective cross-sections is important for nuclear data validation. Whether it is spectral averaged cross-sections (SACS) i.e. the cross-sections averaged over the neutron spectrum (measured at reactors) or differential cross-sections (measured at accelerator neutron sources). Spectral averaged cross-sections usually have the advantage of less uncertainty than differential cross-sections and are thus used for validation of programs describing neutron field transport and interactions. This doctoral thesis describes a method for measuring both the differential cross-sections measured at the accelerator and the method for measuring the spectral averaged cross-sections at the reactor. It includes several experiments and results that have also been published. Both methods used are based on gamma spectrometry of activation foils. The thesis aims to show significant synergies in their joint use.

Keywords: cross-section, measurement, neutron sources, advanced nuclear systems, nuclear data libraries, gamma spectrometry, activation method, nuclear data validation, experiment, accelerator, nuclear reactor.

Contents

Introduction

It is important to mention a necessity of the nuclear databases, especially on the neutron cross-sections data. Those data can be obtained experimentally or from the theoretical models. But theoretical models need a precise knowledge of a nucleus and its interactions, which are still unknown in such a detail we need it. In this case the obtaining new nuclear data and their verification and evaluation have an important role. The knowledge of cross-sections is significant for the nuclear theory and the calculation codes quality is strongly dependent on the amount of the available experimental data. For this reason the new cross-sections measurements are needed.

The main goal of my doctoral thesis is to obtain new experimental data in cross-section measurements, focusing not only on spectral averaged cross-sections but also on differential cross-sections. It was necessary to prepare a methodology for this goal, which I did during my Bachelor and Master studies, where I mainly focused on measurements in LR-0 reactor. But there was a question whether ^{238}U(n,f) fission neutrons affect these measurements. Therefore during my doctoral research I carried out the first experiment on VR-1 reactor, which has higher fuel enrichment. This experiment, as it is described later in this work, proved that even 5% of the ^{238}U(n,f) fission neutrons in LR-0 reactor spectrum does not have a significant influence on the ^{238}U spectral averaged cross-sections measurements. It also means that for SACS measurements can be used different experimental reactors. My colleagues followed up on my work and measured more samples in VR-1 reactor spectrum to validate my result. They also continue with the measurements in LVR-15 reactor spectrum, where the fuel burn up needs to be taken into account.

My experiments during doctoral research were focused on the measurement of various neutron cross-sections. In the neutron field of VR-1 nuclear reactor I measured Y, Ti, Fe, Nb and Cu reactions. In the accelerator neutron field I focused on Cu and Y reactions which were also measured in VR'1 reactor. In the case of the Y sample, I also measured the ^{89}Y(n,3n) reaction, which is impossible to measure in a reactor neutron field due to the high neutron energy reaction threshold. Those reactions were chosen due to the evaluation of ^{235}U(n,f) fission neutron spectrum under the auspices of the International Atomic Energy Agency (IAEA) and the lack of experimental data or effort to refine the existing data of experimental cross-sections. In my previous measurements in the LR-0 reactor during my Master study I also measured neutron cross-sections with Zr, Mn and I samples.

The precise knowledge of the integral cross-sections of (n,xn) reactions for ^{235}U neutron spectrum is practical also for reactor dosimetry, where those reactions are used for monitoring of the neutron flux behind a reactor vessel and determination of its damage, or for refining the ^{235}U neutron fission spectrum in a region of higher neutron energies. On the other hand, the differential cross-sections measured with accelerator-based neutron sources are important for advanced nuclear technology, such as the accelerator driven transmutors.

The High Priority Nuclear Data Request List (HPRL) [1] [2] is under the management of the Nuclear Energy Agency (NEA). This database is a compilation

of the most important nuclear data requirements. The purpose of this list is to provide a guide for those planning measurements, nuclear theory and evaluation programmers. In many cases, there is a lack of experimental data for the suitable reactions or there is a large amount of disparate data. For example ^{62}Cu, ^{89}Y(n,3n), ^{46}Ti and ^{48}Ti(n,p) reactions above 20 MeV do not have data at all and many of the data are below 20 MeV. Also, (n,3n) reactions for Au have larger amount of different data which need to be specified. For ^{175}Lu and ^{209}Bi(n,4n) reaction, there is a lack of data.

My Master thesis was focused on the study of the effective cross-sections of neutron reactions in the reactor neutron field [3]. This PhD thesis follows up on mentioned Master thesis and focuses on the cross-sections measurements of (n,xn) reactions not only using the nuclear reactor (the ^{235}U prompt fission neutron spectrum (PFNS)), but also using the quasi-mono-energetic neutron source produced at an accelerator. It brings together two separate groups of scientists working independently of each other and brings not only new data in the field of measurements of cross-sections, but also new knowledge, from which it follows that the enrichment of the nuclear fuel does not play a significant role in the measurement of SACS and thus a wide range of experimental reactors can be used for these experiments. The aim is also to use the synergy of different types of nuclear data.

1. Nuclear data

Nuclear data play an important role in the field of physical calculations and models not only in reactor physics. They are the building blocks of every model and simulation. As the physical models are used for reactor optimalization the nuclear data are subject to constant research and refinement. The precision of physical models is dependent on precision of nuclear data. In a field of reactor physics it plays a key role in a reactor safety and optimalization. Reactors are in operation in conservative approach when all safety criteria have to be met even in the worst case scenario. By minimazing the uncertainty of nuclear data one can minimaze economic losses and technical problems. Also due to the fact that reactor vessel is the only irreplaceable part of a nuclear power plant and damaging it means reactor shut down, it is important to calculate the reactor vessel radiation damage as precisely as possible.

Nuclear data are also important in the field of advanced nuclear systems such as generation IV reactors or fusion reactors and accelerator driven systems (ADS) [4]. In the process of new nuclear reactor designs, nuclear data are used for example in a criticality calculations and determination of reactivity coefficients which is essential for the reactor operation and its safety. These data are sensitive to nuclear data uncertainties. [5] Thanks to considerable effort in spectral averaged cross-sections experiments in the field of nuclear reactors we have a good basis for new reactors design. However in the case of more economical use of nuclear fuel and thus higher fuel burn up it is necessary to have more precise data. Also especially in the case of reactors which are cooled by liquid salts or liquid metals we do not have enough accurate data for neutron interactions with those coolant materials [4].

Another major problem is with the burned nuclear fuel. Used nuclear fuel contains transurans with a long half-life and thus causing problems with its storage and reprocessing. This problem can be solved by transmutation of nuclear fuel. This concept is described in more detail in 1.2.

Last but not least, accurate nuclear data are also needed for research in the field of fusion reactors, where 14 MeV neutrons are produced and effective cross-sections are needed for interactions with fusion reactor construction materials and for calculating of their radiation damage, as in the case of conventional nuclear reactors used in nuclear power plants [6].

1.1 Nuclear databases

On the basis of international cooperation, the libraries of nuclear data have been created and currently they are still being updated with new data and refined. The library of experimental data which were measured by physicist all around the world is EXFOR (Experimental Nuclear Reaction Data) library [7]. This library is compiled by the Nuclear Reaction Data Centres Network (NRDC) under the auspices of the International Atomic Energy Agency (IAEA). NRDC was established in 1966 to coordinate the collection, compilation and dissemination of nuclear reaction data in the universal EXFOR format. Data from this library are subsequently used for evaluation of cross-sections experimental data which

means they are compared to theoretical data obtained from calculated models. Those evaluated data then form libraries such are ENDF (Evaluated Nuclear Data File), which is the evaluated nuclear data library in the US [8], JEFF (The Joint Evaluated Fission and Fusion) [9], JENDL (Japanese Evaluated Neutron Data Library) [10], CENDL (Chinese Evaluated Nuclear Data Library) [11] or TENDL-2021, which is a nuclear data library which provides the output of the TALYS nuclear model code system for direct use in both basic physics and applications [12]. The code TALYS is deterministic nuclear calculation code capable of calculating many different quantities from the field of nuclear physics. [13]. These libraries differ in their results for the same reactions because the evaluation process is influenced not only by the used theoretical model but also by the evaluator itself, their experience and by the experimental data which are used for some of the model parameters. For the illustration, Figure 1.1 shows ^{46}Ti(n,p) reaction cross-sections from different data libraries.

Further it would be good to mention the existence of High Priority Request List (HPRL), which is a list which contains clarification requirements of selected nuclear data. These requirements come mainly from the nuclear data providers dealing with calculations for the industrial application of nuclear technologies. This database is managed by the Nuclear Energy Agency (NEA). This database is available online and usually serves as a basis for planning new measurements of cross-sections [14].

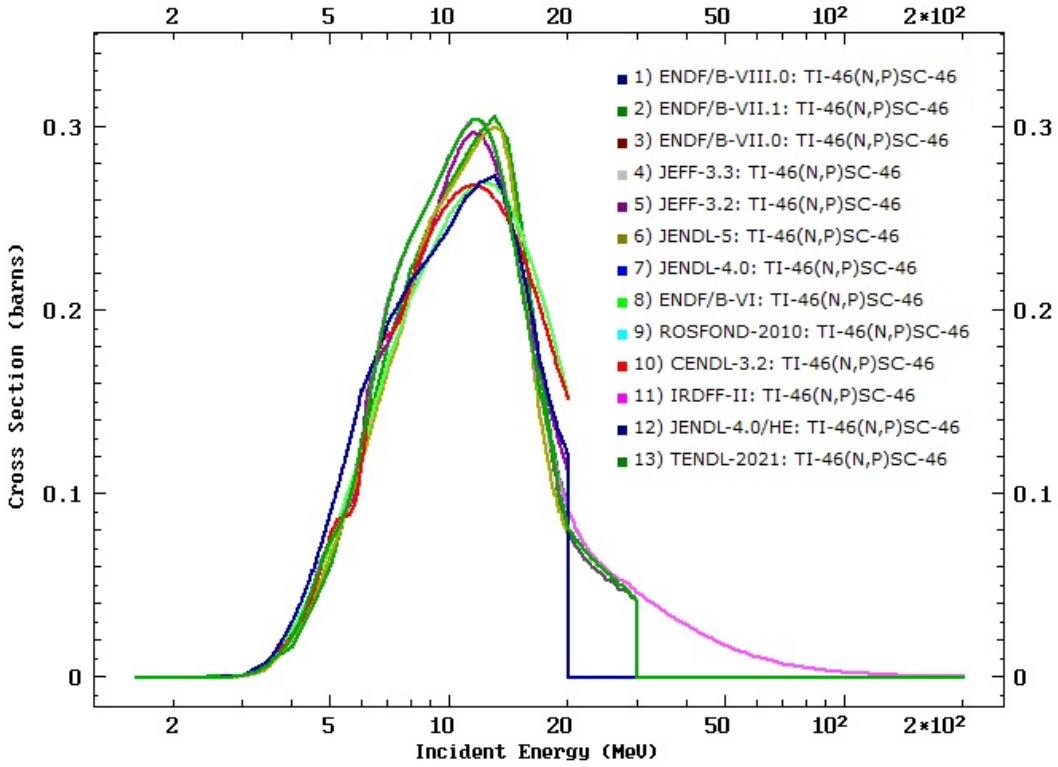

Figure 1.1: ^{46}Ti(n,p) reaction from different data libraries. [15]

1.2 Nuclear fuel transmutation

The spent nuclear fuel is mostly stored and its further use is not expected, mainly due to the economic and technical reasons. The Czech Republic is no exception and that is why the deep geological repository is being planned [16]. One of the key tasks of advanced nuclear systems is to close the nuclear fuel cycle and thereby we can not only obtain more energy but also minimize nuclear waste. Those advanced systems need new precise nuclear data and that is why their measurements and clarifications are necessary.

Even in classic nuclear reactors, transmutation can be achieved and the fuel cycle can thus be partially closed. VVER-1000 (Temelin nuclear power plant) or VVER-440 (Dukovany nuclear power plant) reactors are used in the nuclear power plants in the Czech Republic, which is a type of pressurized water reactor with 1000 MW (440 MW) electric power. The spent fuel from this type of reactor contains a lot of actinide isotopes and also fission products with a long half-life. Some of the actinide nuclides can be converted to fissionable ones of those fission products can be converted to radioisotopes with shorter half-life by transmutation. [17].

Fission products such are ^{90}Sr or ^{137}Cs are short-lived isotopes (half-life is about 30 years) and thus they can be simply stored until they decay. They also have a low neutron absorption cross-sections, so they can not be easily transmutated. On the other hand, fission product ^{129}I with the half-life 15.7 million years can be transmutated to isotopes with much shorter half-life. Table 1.1 summarizes some of the most common fission products in spent fuel (SF) with their half-life $T_{1/2}$.

The transmutation of spent nuclear fuel can allow us to reduce the volume of high-level nuclear waste and thus enables a significant reduction of storage of SF. Plutonium isotopes from SF can be recycled by MOX and REMIX fuel which can be subsequently used in standard reactors. Heavier isotopes can be transmuted in fast reactors or in sub-critical reactors. Those sub-critical reactors are based on a concept of ADS [18] [19] [20] [21] [22].

The concept of radioactive waste and spent nuclear fuel management of the Czech Republic is the key document that formulates the principles, procedures and goals of the state for the period until approximately 2030 in the field of spent fuel. In this document it is stated that spent nuclear fuel will be stored in deep geological depository and it is not planed for reprocessing it or using as MOX fuel. However this variant is not excluded in future [16].

1.2.1 MOX fuel

Mixed oxide fuel (MOX) is a nuclear fuel which contains more than one oxide of fissile material and it is manufactured from plutonium, recovered and used reactor fuel, mixed with depleted uranium. Using this fuel we can recycle nuclear fuel from current reactors and also reduce plutonium and uranium. It is also possible to use weapons-grade plutonium in MOX fuel and reduce its existing stockpile. This leads to closing of the nuclear fuel cycle. For using this type of fuel we also need to have precise data for cross-sections, especially for Pu, Am and Cm. This MOX fuel allow us to transmutate Pu from spent fuel in standard

Table 1.1: Actinides and the most common fission products in SF.

Nuclide	$T_{1/2}$
^{137}Cs	30.08 (9) y
^{90}Sr	28.79 (6) y
^{236}U	2.342×10^{7} (4) y
^{238}Pu	87.7 (1) y
^{239}Pu	24110 (30) y
^{240}Pu	6561 (7) y
^{241}Pu	14.329 (29) y
^{242}Pu	3.75×10^{5} (2) y
^{241}Am	432.6 (6) y
^{237}Np	2.144×10^{6} (7) y
^{242m}Am	141 (2) y
^{243}Am	7364 (22) y
^{242}Cm	162.8 (2) d
^{244}Cm	18.11 (3) y
^{99}Tc	0.211×10^{6} y
^{126}Sn	0.230×10^{6} y
^{79}Se	0.327×10^{6} y
^{93}Zr	1.53×10^{6} y
^{135}Cs	2.3×10^{6} y
^{107}Pd	6.5×10^{6} y
^{129}I	15.7×10^{6} y

nuclear reactors.

Plutonium isotopes are produced in every nuclear reactor. ^{239}Pu and ^{241}Pu are fissile and thus approximately half of ^{239}Pu is burned in reactor and provides one third of the total energy. So the higher burn-up of the fuel is, the less Pu is in the spent fuel. Typically about 1% of the spent fuel is Pu isotopes, so about 70 tonnes of Pu is removed from nuclear reactors worldwide each year. This Pu can be used to substitute the fresh fuel with ^{235}U enrichment. We also have a significant amount of Pu from ex-military sources [23].

To produce this MOX fuel, partitioning, which is a chemical process of separating the different elements in the spent nuclear fuel, is needed. More information about this fuel, its chemistry and Pu separation from the spent fuel can be found for example in [24], respectively in [25] or [26].

An alternative for the MOX fuel is a REMIX fuel (Regenerated Mixture). This REMIX fuel is produced directly from a non-separated mix of recycled uranium and plutonium from reprocessing of used fuel.

1.2.2 ADS and MYRRHA

Our society faces the increasing demand for electricity and renewable energy sources cannot fully satisfy the global demand, so the nuclear energy plays an important role. During the operation of nuclear power plants, high-level radioactive waste (HLRW) [27] is produced and technical and socially acceptable solution for this waste is necessary. Geological disposal of this waste is a good solution but the time scale needed for the radio-toxicity to drop to the natural uranium level

is very long. This problem can be solved by accelerator-driven reactors, which will make it possible to effectively transmute transuranics in the spent fuel. The development of such accelerator driven transmuters can be enabled by the project MYRRHA, which is Multi-purpose hybrid research reactor for high-tech applications [28] [29].

This sub-critical reactor is based on ADS. This concept produces fission without achieving criticality in reactor ($k_{eff} < 1$). In order to sustain the reaction an external source of neutrons is used, which is placed at the center of the core where the spallation reactions are used for neutron production. It means the high-energy protons from the accelerator are impinging on a target from a heavy metal such as lead. The neutron spectrum is made of two parts, the fission spectrum and high-energy tail up to the energy of the incident proton. The high energies of neutrons are needed because the probability that these neutrons induce a fission of the actinides in SF is higher than the neutron capture and then the actinides are trasmutated into fission products instead of just becoming heavier elements by neutron capture. This neutron capture cross-section is higher for slow, thermal neutrons, so this transmutation system needs a fast neutron spectrum. It also means, that those systems cannot be cooled by water, because water is a neutron moderator, so here, liquid metals like sodium and lead or gasses such He are used. In addition, these materials can provide much more efficient cooling, which is necessary in this case. This is also why we need as precise as possible nuclear data for those materials [30].

ADS reactors also have an advantage in comparison to fast critical reactors which is fuel loading of actinides up to 40% of the core inventory. The reactivity control of critical reactors is mainly driven by the delayed neutrons and actinides, which have a smaller value of those delayed neutrons compared to uranium isotopes. So the higher the amount of actinides in the core is, the faster the reactor become. Therefore those critical fast reactors can be loaded up to the maximum of 5% of actinides [28].

MYRRHA is a future project, the European first large scale research of ADS. On 7th September 2018 the Belgian Federal Government decided to build it on the SCK CEN (Belgian Nuclear Research Center) site in Mol. It will consist of 4 major components: the linear accelerator, the lead-bismuth eutectic cooled reactor, the proton target facility and the full power facility. It will be constructed in 3 phases, where phase 1 is a design and construction of the first linac section up to 100 MeV and it is scheduled for completion in 2026. Phase 2 will be the extension of the 100 MeV linac to 600 MeV and it is planned to be finished in 2033. Phase 3 is a reactor construction which is scheduled to be commissioned in 2036 [31]. The visualization of this MYRRHA reactor can be seen in Figure 1.2. This facility is conceived to work in both sub-critical and critical modes, so besides transmutation it will have a wide range of applications, from fuel and material developments for Gen IV systems and fusion reactors, to radioisotope production for medical applications allowing less invasive cancer treatment. The reactor core is going to be composed of a lattice with 183 hexagonal channels, Pu enrichment about 30% and liquid Pb-Bi cooling system.

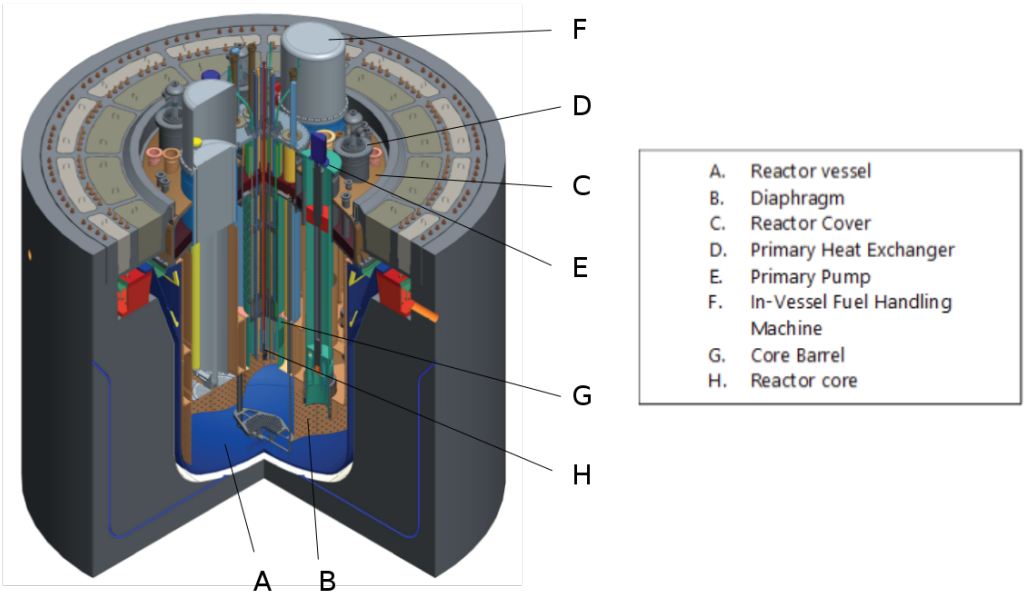

Figure 1.2: The sub-critical reactor MYRRHA schematic view. [28]

1.3 Neutrons cross-sections theory

The cross-section itself represents the probability that some reaction occurs and for neutron reactions the excitation function has three parts, as can be seen in Figure 1.3. The specific shape of the excitation function depends on the energy of the reaction, whether it is an exothermic or endoergic reaction. The first part is 1/v region with the neutron energy below 1 eV. In this area the cross-section is inversely proportional to velocity of the incident neutron. The second part is resonance region with neutron energy from 1 eV approximately up to tens of keV. In this region plays a crucial role the nucleus structure, because the resonances origin are the excited states of the nuclei which is produced. If the neutron energy corresponds to the energy of excited state of the produced compound nucleus, the cross-section is significantly higher. Those two parts of cross-section are measured by the online method where the prompt γ rays of scattered particles and other reaction products are measured during the irradiation itself. The used method of measurement is the Time-of-Flight principle (ToF). It is the measurement of the time taken by the particle to travel a distance through some sample. From this information we can obtain which energy the neutrons had when passing through the sample at that time. For this technique we need a neutron source which works in pulse mode, which is usually the spallation source. The well-known facility focused on this type of measurements is nTOF in CERN. [56]

The third cross-section part is the higher energies region, where the distance between resonances reaches the width of resonances and thus we can not distinquish them and the result is smooth excitation function. In this region also the threshold of (n,xn) reaction takes place. The method of cross-section measurement in this area is usually the offline measurement method, where the measurement takes place after the irradiation. There are various methods, which depend

on the studied material. In this work I will describe just one method which I used in my experiments, and it is a gamma spectrometry method. We can use this method due to the fact that the reaction pruducts are unstable and undergo the following decay which can be measured by the detector. In this work I focused on the study of (n,xn) reactions measurements not only in reactor neutron spectrum to obtain SACS but also in accelerator neutron spectra to obtain differential cross-sections. The cross-sections study in the nuclear reactor neutron spectrum is mainly used for the data validation and in my experiments I use the research reactors in the Czech republic, LR-0 [42] and also VR-1 [46] reactor. For the differential cross-sections study I used cyclotron with quasi-monoenergetic neutron spectrum. This spectrum contains monoenergetic peak and some background, which needs to be subtracted. The both types of used neutron sources for the cross-sections study are described later in this work as well as the background subtraction of neutron spectra in accelerator measurements or also the gamma ray spectrometry basis and the HPGe (High Purity Germanium) detector characterization, which is also essential for the cross-sections measurements.

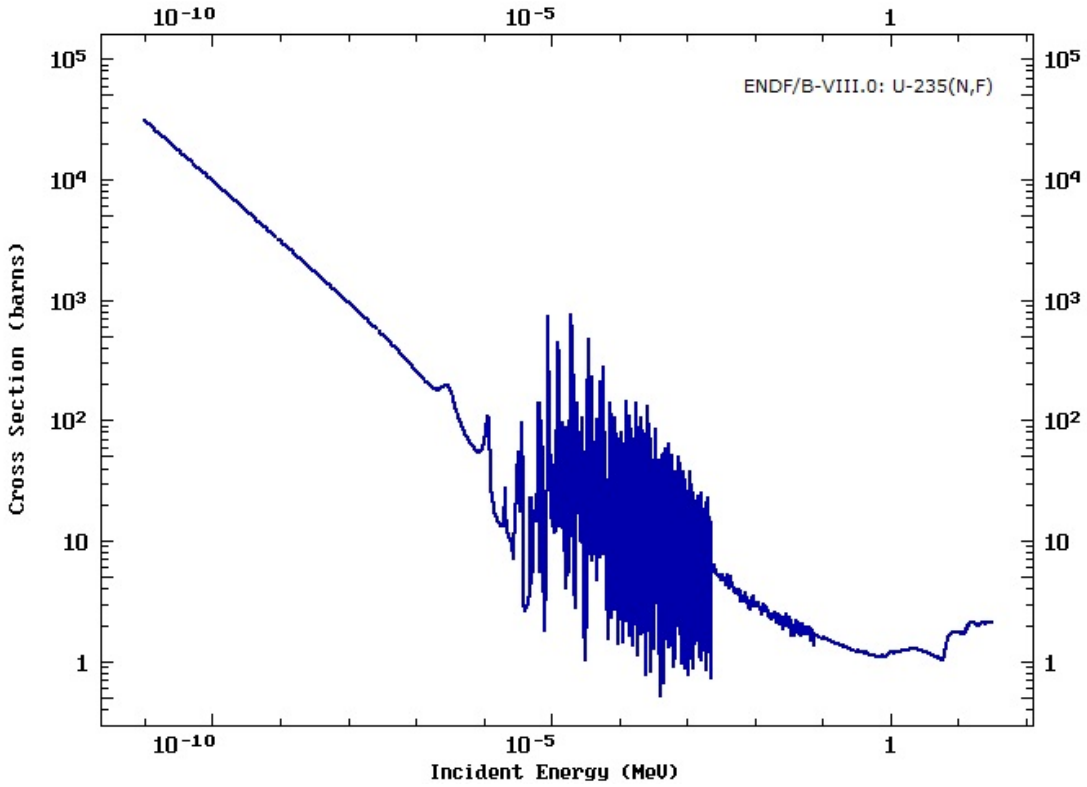

Figure 1.3: The ^{235}U(n,f) reaction cross-section. [15]

2. Gamma ray spectrometry theory

The gamma-ray spectrometry deals with the measurement of the energy and the intensity of gamma rays. From measured spectrum we can obtain the activity, which is the quantity that indicates the speed of nucleus decays. The unit is Becquerel [Bq].

$$A = \frac{dN}{dt} = -\lambda N, \tag{2.1}$$

where λ is the decay constant that is different for each radionuclide and $\frac{dN}{dt}$ is the change of radioactive nucleus quantity at the time. For my experiments are essential to measure the gamma ray. In all of my experiments the High Purity Germanium detector (HPGe) for the gamma ray measurement, which is a type of semiconductor detector, was used. The short description of the HPGe detector, the theory of gamma ray interaction with this type of detector and spectrum description will be described in following sections.

2.1 HPGe detector

For gamma ray measurement it is possible to use also scintillation detectors which has better efficiency, which is given by high proton number of crystal, further more it has shorter dead time in comparison to the HPGe detector. In my experiments I used a HPGe detector because of its energy resolution. Here I will describe only HPGe detector principles. In my bachelor thesis the description of the scintillation detector principles and semiconductor detectors as a whole can be found [32].

2.1.1 The construction of HPGe detector

HPGe detector has to be cooled down because of the energy band gap in semiconductors. Thus it typically has a liquid nitrogen reservoir. Its main part is Dewar vessel which contains liquid nitrogen with temperature 77 K. The preamplifier is placed with Ge crystal in vacuum and is cooled with detector.

The detector cup is mostly from aluminum and must be light to minimize the absorption of gamma rays that we want to measure by the detector.

For the more accurate measurement of a radioactive sample it is necessary to shield the detector with measured sample from natural background. The natural background include for example detector material itself, cosmic rays, rays from surrounding materials etc.

For attenuation of surrounding rays it is applicable to close the detector with the sample into the lead cover as is in the Figure 2.1. The inner side of the lead cover is covered by copper due to shielding the high lead X-rays. Copper itself has lower X-rays. Of course we can not shield our natural background perfectly. We measure the background spectrum first before the sample measurement and after it, this spectrum is subtracted from the spectrum of the sample. An example

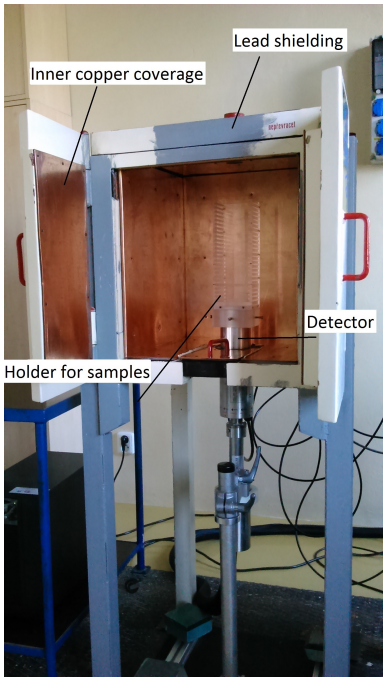

Figure 2.1: Example of HPGe detector shielding

of background spectrum in LR-0 laboratory is in the Figure 2.2. It contains some significant peaks. The biggest one is from potassium ^{40}K with the energy 1460.8 keV. Other peaks come from decay series of U and Th. At the low energies these are the peaks from X-rays of shielding materials as are Pb, Cu, Cd and Sn.

2.1.2 HPGe characteristic parameters

The main characteristics parameters of germanium semiconductor detector are efficiency of the detector, energy and time resolution and ratio of Peak/Compton.

We distinguish more than one detector efficiency. The main ones are the relative efficiency, intrinsic efficiency, absolute full efficiency and absolute peak efficiency [33] [34].

The relative efficiency is efficiency relative to the measurement at standard Na(Tl) scintillation detector and is set for point source ^{60}Co which is placed on the axis of detector in the distance 25 cm and is measured 1000 s. This value is specified by the manufacturer of the detector and the error must be less than 10%. The relative efficiency R_{eff} could be computes from the equation [33]

$$R_{eff} = \frac{P \cdot 100}{t \cdot A \cdot 1.2 \cdot 10^{-3}} \, [\%], \tag{2.2}$$

where P is net peak area at the energy 1332.5 keV of the source ^{60}Co, t is live time, A is activity of source in the time of measurement and $1.2 \cdot 10^{-3}$ is conversion coefficient. Using this equation, the efficiency specified by manufacturer should be verified.

Intrinsic efficiency of detector is ratio of detected quanta and number of quanta which go into the sensitive part of detector. This efficiency is only one, which is independent on measurement geometry.

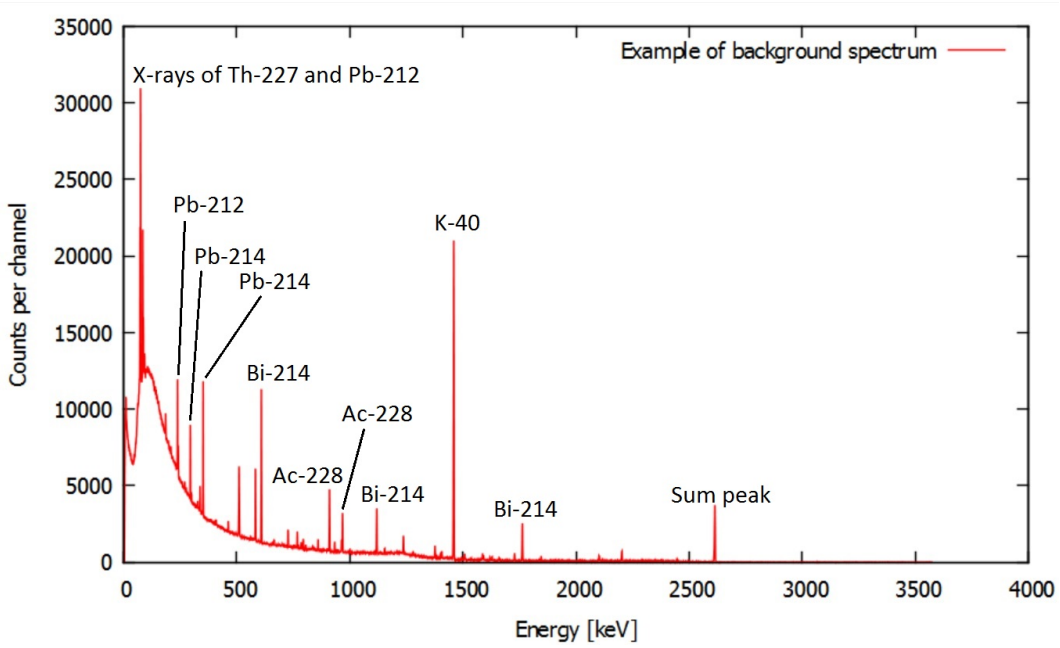

Figure 2.2: Example of background spectrum measured by shielded detector

The absolute efficiency is the ratio of all detected quanta in detector and number of quanta emitted by a source.

The absolute peak efficiency is a ratio of detected quanta in FEP and quanta emitted by source at same energy as FEP. This efficiency is dependent on energy and forming efficiency curve which is in the Figure 4.7.

We need to have a good HPGe model to have a good detector efficiency not only for a point souce, but also for a source with some volume, such are the measured samples. For a volume samples the efficiency is not measured, but calculated by the MCNP code. More about this problematic is written later in this thesis in the section 4.1.3.

The energy resolution of detector is described by Full Width at Half Maximum (FWHM). It is stated for photon energies 1332 keV and 122 keV by the manufacturer.The detector can usually distinguish two peaks which are 3 FWHM apart. If peaks are closer, the detector assess them as one peak as can be seen in Figure 2.3 (b).

This energy resolution is dependent on detector property and its electronics. Thus for FWHM hold in equation

$$FWHM = R_{total} = \sqrt{R_{det}^2 + R_{el}^2}, \tag{2.3}$$

where R_{det} is the resolution of detector and R_{el} is the resolution of electronics [34].

The time resolution of the detector is described by the dead time. It is a time interval during which the detector is insensitive and does not detect anything. The dead time depends on the physical processes in the detector crystal and also on its electronics and the intensity of gamma rays which come to the detector. The more intensive source is, the lower the detection efficiency of the detector is. For measurement more intensive sources, it is better to place them farther away from the detector.

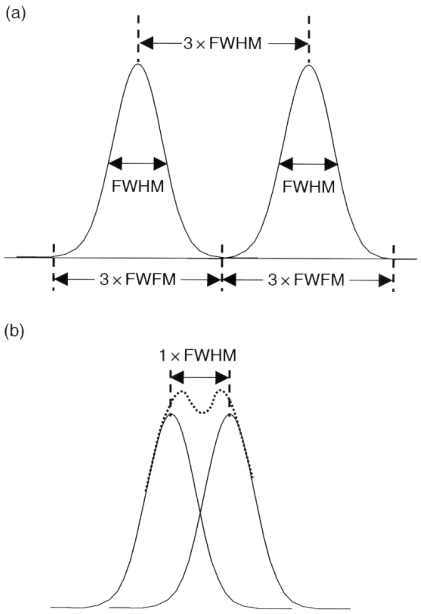

Figure 2.3: Energy resolution of detector [34]

The ratio of Peak/Compton expresses the detector ability to detect low energies when the higher energies are present. It is presented as a ratio of the 1332 keV peak height of the ^{60}Co source and the average height of the Compton continuum plateau between 1040 keV and 1096 keV [33].

2.1.3 Statistics of detector processes

The interaction of γ quanta with the matter of the detector take place on the microscopic level and so it follows the laws of quantum mechanics which are based on the probability. The nucleus decays are random, thus the caused ionization is also random.

Probabilities of measurement of impulse certain values are followed by Poisson distribution which is described by the function

$$f(k;\lambda) = \frac{\lambda^k e^{-\lambda}}{k!}, \tag{2.4}$$

where λ is the average number of events per interval, e is Euler's number and k takes values 0, 1, 2, ...

When we have large amount of impulses (minimum is dozens of impulses) the Poisson distribution proceeds to the Gauss distribution. In gamma-ray spectrometry the large amounts of impulses are usually measured, that why Gauss (normal) distribution is used, which is described by the function

$$f(x) = a \cdot e^{\frac{-(x-\mu)^2}{2\sigma^2}}, \tag{2.5}$$

where μ is mean of the distribution, σ is standard deviation and a is a parameter of height.

If the detector detected N interactions, thus according to Gauss distribution, the standard deviation is $\sigma = \pm\sqrt{N}$. It means that if we repeat the measurements, the 68.2 % of all detected interactions are in the interval (N - σ, N + σ), 95.4 % are in the interval (N - 2σ, N + 2σ) and 99,6 % are in the interval (N - 3σ, N + 3σ). It can be seen in Figure 2.4.

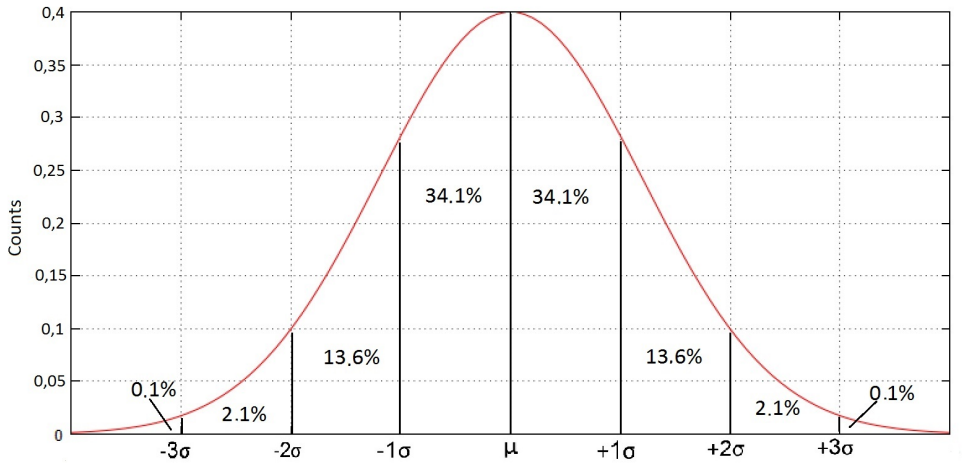

Figure 2.4: Gaussian (normal) distribution

The relative error of the measurement Δ is determined by the ratio σ/N or $\Delta = \sqrt{N}/N$. That means the relative error is smaller when the number of measured impulses N is bigger. For the error less than 1% we need more than 10^4 measured impulses.

2.2 Gamma ray interaction with the HPGe detector

We have three possible gamma radiation interactions with the matter, which are photoelectric absorption, Compton scattering and pair production.

2.2.1 Photoelectric absorption

The photoelectric absorption occurs at the bound electrons in an atom and the most frequently at the K-shell. Photon transmits its whole energy to the electron which is ejected from the shell. The energy of ejected electron E_e is therefore equal to the energy of photon E_γ reduced by bounding energy E_b:

$$E_e = E_\gamma - E_b. \tag{2.6}$$

The atom is in exited state after the electron ejection. It can deexcite by filling the vacancy left by ejection of a higher-energy electron. It falls into left vacancy and emits a characteristic X-rays. Alternatively the atom could deexcite by Auger effect. The probability of photoelectric absorption is expressed by cross section τ which depends on atomic number Z of matter and also on energy of gamma

radiation:

$$\tau \approx Z^n / E_\gamma^{3.2}, \tag{2.7}$$

where n is within the range 3 and 5, depending upon energy of photon. Thus photoelectric absorption dominates at lower energies and at materials with higher Z. For the gamma-spectrometry, the photoelectric absorption is one of the most

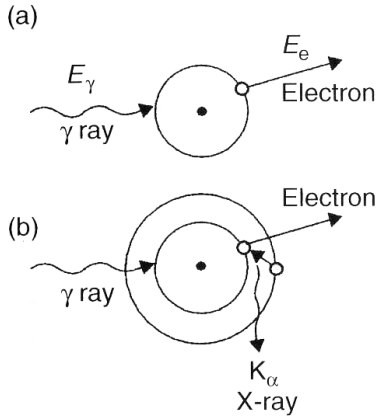

Figure 2.5: Photoelectric absorption mechanism (a) and the X ray fluorescence (b) [34]

important interaction among gamma radiation with matter. During this process, the whole energy is transferred to the electron. The photoelectric absorption scheme is in the Figure 2.5.

2.2.2 Compton scattering

The Compton scattering occurs at free electron or electron which is weekly bounded, thus at valency layer of an atom. The free or weakly bounded electron is ejected from atom after collision with the photon. In this case the original photon does not cease of exists as during photoelectric absorption, but loses only a part of its energy and is scatted from original direction. The relation for recoil electron energy follows from the conservation laws of energy and momentum [34]:

$$E_e = E_\gamma - E_\gamma^{'} = E_\gamma[1 - \frac{1}{(1 + \frac{E_\gamma(1-cos\theta)}{m_0 c^2})}], \tag{2.8}$$

where E_γ is the energy of original photon, $E_\gamma^{'}$ is the energy of scattered photon, m_0 is the electron rest mass and θ is the scattering angle. Extremes for Compton scattering are for angles $\theta = 0°$ and $\theta = 180°$. The original photon does not lose its energy ($E_e = 0$) and its scatter is zero, when the angle $\theta = 0°$. Whereas when the angle is $\theta = 180°$ the original photon is backscattered and its loss energy is the biggest, but it never loses all energy. The expression in square brackets is closest to one for an angle of 180 decrees. The scheme of Compton scattering is in Figure 2.6.

In the Figure 2.7 of theoretical spectrum it is seen Compton edge which corresponds to the scattering angle 180° of original photon. The theoretical decrease

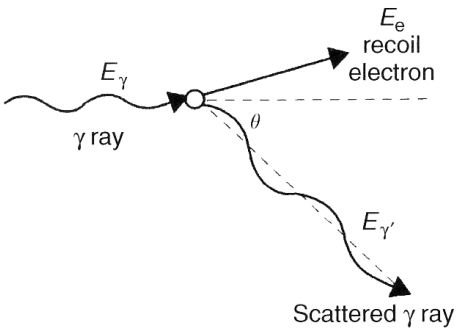

Figure 2.6: Compton scattering [34]

of Compton edge is abrupt, but practically occurs as milder decrease which is indicated by the dotted curve in Figure 2.7. It is caused by multiple Compton scatterings of photon.

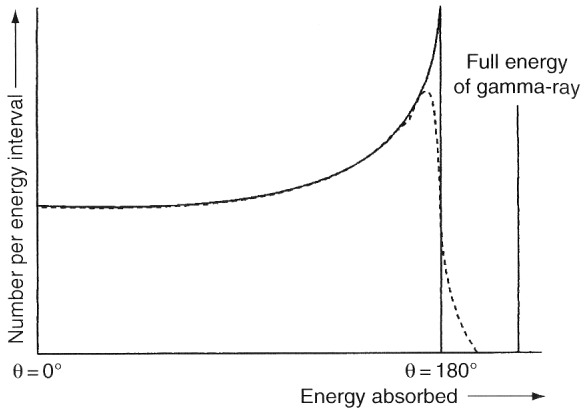

Figure 2.7: Theoretical spectrum of transferred energy to absorber by Compton scattering related to scattering angle [34]

Probability of Compton scattering is expressed by cross section σ which depends on atomic number of material Z and on the energy of photon E_γ. It could be approximately written by expression [34]

$$\sigma \approx Z/E_\gamma. \tag{2.9}$$

Compton scattering is elastic and not coherent. It also exists as coherent scattering when the energy of photon is not changed. Only its momentum is changed, thus the original photon solely changed its movement direction. This coherent scattering dominates for higher wavelengths of radiation, that is a reason why the representation of this coherent scattering is small.

2.2.3 Pair production

Pair production takes place within the Coulomb field of nucleus. As a result is conversion of gamma ray into an electron-positron pair. The scheme is seen

in Figure 2.8. This interaction could occur only if the energy of gamma rays is greater than 1022 keV which is equivalent to the combined rest mass of the two produced particles (511 keV each). This energy should be computed by Einstein equation $E = mc^2$, where m is a mass of particle and c is speed of light in vacuum. The created positron is slowed down to the thermal energy and than annihilates with electron, resulting in two annihilation photons with the energy of 511 keV each. The annihilation mostly occurs of the order 1 ns after the electron-positron pair origins.

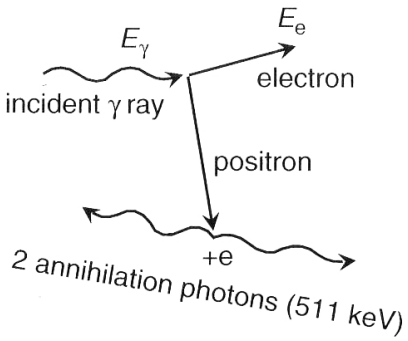

Figure 2.8: Electron-positron pair production [34]

Probability of pair production is expressed by cross section κ [34]

$$\kappa \approx Z^2 ln(2E_\gamma). \tag{2.10}$$

This interaction causes, in the gamma ray spectrum, the annihilation peak and so-called single and double escape peaks. After the photon annihilation, two photons with 511 keV each, arise. These photons could again interact in detector or leave the detector without the interaction. In the case just one photon leaves the detector, the single escape peak is created and in the case both of them leave the detector, the double escape peak is created.

2.2.4 Cross-sections of each interaction

In Figure 2.9, the total experimental cross section σ_γ on a carbon and lead atom is shown. The result is curve compound from curves a, b, c, d and e, where the curve a shows the photoelectric absorption, curve b is the Rayleigh (coherent) scattering, c corresponds to the Compton scattering and curves d and e are electron-positron pair production, where d is a pair production in the field of the nucleus and e is in the field of the atomic electrons.

2.3 Gamma ray spectrum and Genie 2000

Output of the measurement in gamma-ray spectrometry is an spectrum of energies. Spectrum shows the dependence of channel number (channels in multichannel analyzer) to the counts per the channel. The channel number should be transferred to the energy by the energy calibration. In the spectrum we can see

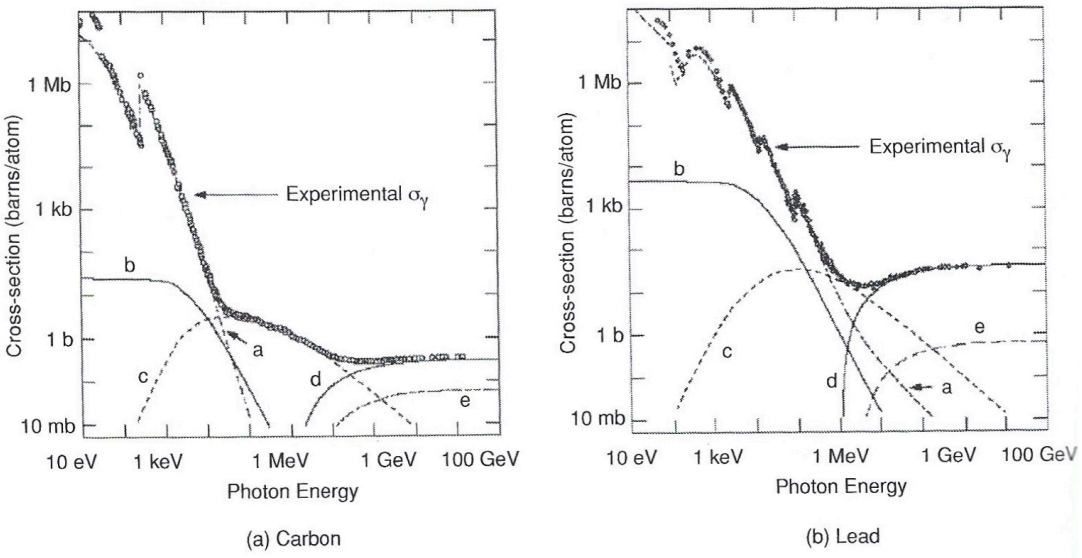

Figure 2.9: Probabilities of each interactions [35]

interactions of gamma rays with the material of detector and with the surrounding material as a detector shielding. The peaks, which are results from the full absorption of its photon in the detector, are important for radioactive isotopes identification. These peaks are caused by photoelectric absorption or by multiple Compton scatterings followed by the photoelectric absorption or the pair production followed by photoelectric absorption of both annihilation photons. In the Figure 2.10 we can see the characteristic spectrum of ^{137}Cs. This radionuclide has only one peak with the energy 661.7 keV. The part of spectrum before the full energy peak (FEP) is caused by the Compton scattering and we can see the Compton edge.

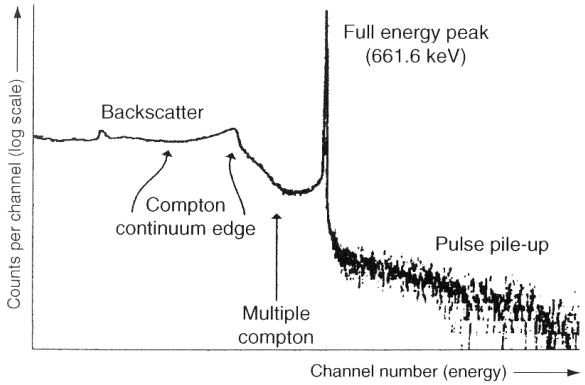

Figure 2.10: Example spectrum of ^{137}Cs [34]

Multiple Compton scattering is between the Compton edge and FEP. The part of spectrum behind the FEP is a pulse pile-up. It is a condition where two pulses are generated so close in the time that effectively a single composite pulse is produced. It is also referred as a random summing [34]. Backscatter peak is caused by Compton scattering out of the detector (for example in the shielding)

and scattered photon is detected by detector.

In the area of Compton scattering could be another peaks which are caused by the electron-positron pair production. It includes the annihilation peak and also double escape peak and single escape peak. Annihilation peak is always on the energy 511 keV and it is caused by detection of photon created by electron-positron pair production out of the detector (for example in a detector shielding). Unlike single escape peak (SEP) is 511 keV before FEP and double escape peak (DEP) is 1022 keV before FEP as we can see in the Figure 2.11.

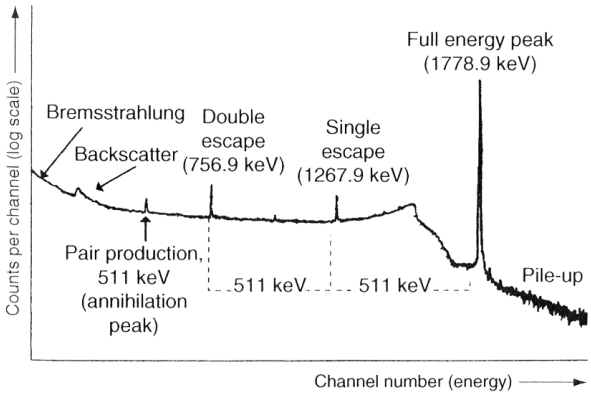

Figure 2.11: Example spectrum of ^{28}Al [34]

In the spectrum we can also see the characteristic peaks of X-ray and summing peaks. The X-ray peaks are usually at low energies in the spectrum and they are caused by photoelectric absorption. The summing peaks are cased by the sum of two or more peaks of one radionuclide.

Let us consider two models of a detector, purely from a theoretical point of view. If we assume a model of a really small detector, we will see only double escape peak in the spectrum and we do not have counts in the area between FEP and Compton edge. It is because in a very small detector occurs only one Compton scattering and not multiple Compton scatterings, because the photon leaves the detector earlier. Whereas in the second model of infinity detector we have only FEP. That is because whole energy of gamma rays are absorbed in a detector [34].

The measured spectrum can be evaluated in many ways. In this work I will describe just one program, Genie 2000, which I used in my experiments for spectrum evaluation and obtaining the net peak area (NPA) of interested peaks. The evaluation in program Genie 2000 has a few basic steps. Firstly is needed to do energetic and efficiency calibration of the detector. Then the analysis of the measured spectrum can be done. This analysis include finding of the peaks, assignment of radionuclides to each peak, fit by Gaussian function and determining peak area (NPA), which is essential for the cross-sections calculation. In the following subsections, I will describe in more detail each step of spectrum evaluation in program Genie 2000.

2.3.1 Energy calibration

Before the measurement the energy calibration is needed to do. That means to assigned each channel of MCA (multi-channel analyser) to the energy. It

is usually linear dependence between the energy of photon and the channels. Energy calibration is frequently made by using point sources ^{137}Cs, ^{60}Co, ^{241}Am, ^{152}Eu, ^{133}Ba etc., because their peaks cover the required energy range. The energy calibration also includes determination of parameters characterizing the dependence of peak shape on energy. These parameters are half-width FWHM and low-energy tail of the peak. The example of energy calibration by program Genie 2000 is in Figure 2.12, where can be seen the linear dependency.

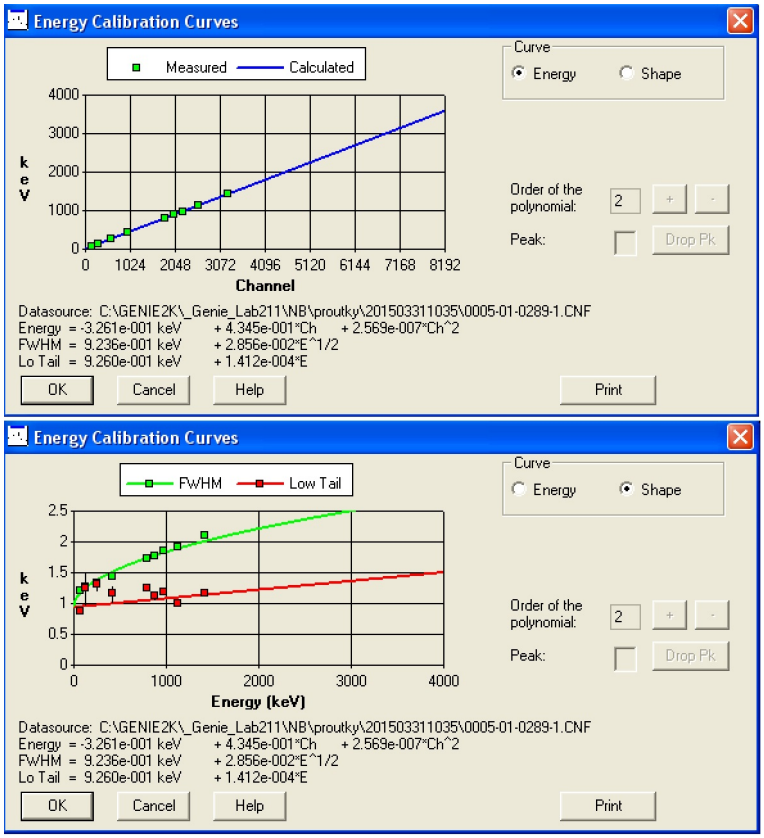

Figure 2.12: Energy calibration in program Genie 2000 [36]

2.3.2 Efficiency calibration

For determination of the amount of isotope in the sample, respective activity, it is needed to do the efficiency calibration of the detector. First of all I need to mention that we have more efficiencies, such are relative efficiency, absolute peak efficiency and total efficiency, but for gamma-ray spectrometry, the absolute peak efficiency is essential and thus this type will be described in more detail. Absolute peak efficiency of the detector, for set geometry of the sample and its specific location relative to the detector during the measurement, depends on the energy.

Efficiency of detector is thus the conversion factor between the measured peak area and the activity of sample and hold the equation [36]

$$A_0 = \frac{NPA}{t_{live} \cdot \mu \cdot Y} \cdot K, \tag{2.11}$$

where NPA is net peak area, t_{live} is live time of the measurement without dead time of detector, Y is intensity of the peak, μ is the detector efficiency, and K is the decay correction during the measurement and correction to the reference time, which is discussed later in this section. Value A_0 is therefore the activity of sample at the beginning of the sample measurement.

Using the calibration sources with known activity, the efficiency curve for the detector can be determined from the equation 2.11. An example of this calibration in the program Genie 2000 is in Figure 2.13, where the upper window is in a linear scale and the lower one is in a logarithmic scale. Used calibration sources were CMI standards of EG3 type (point sources) ^{60}Co, ^{137}Cs, ^{241}Am, ^{133}Ba and ^{152}Eu. But for the samples measurement itself, the calculated efficiency curve by MCNP code was used [37]. This curve can be seen in Figure 2.14. The measured curve using the point sources can not be used because the measured samples are not the point source. The difference between measured efficiency calibration and calculated efficiency by MCMP code can be seen in Figures 2.13 and 2.14. It is also important to mention, that efficiency is also dependent on the source to detector distance.

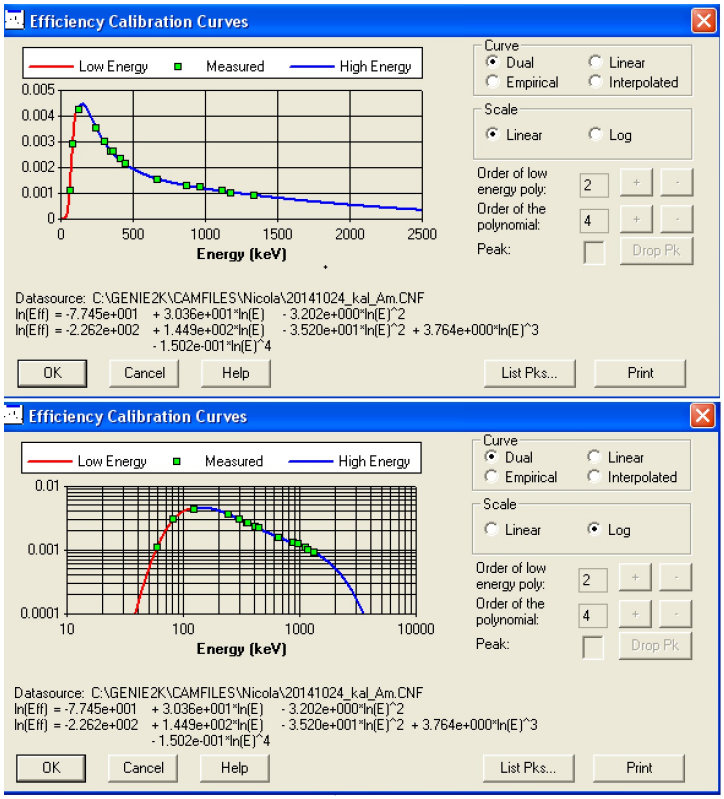

Figure 2.13: Efficiency calibration measured using the EG3 sources [36]

2.3.3 The spectrum evaluation

The spectrum can be evaluated after the energy and the efficiency calibration. This evaluation include some steps, which could be set into a sequence in program Genie 2000. Therefore is not necessary to repeat each step for each spectrum separately. Using the sequence we can save the time. In Figure 2.15 is one sequence

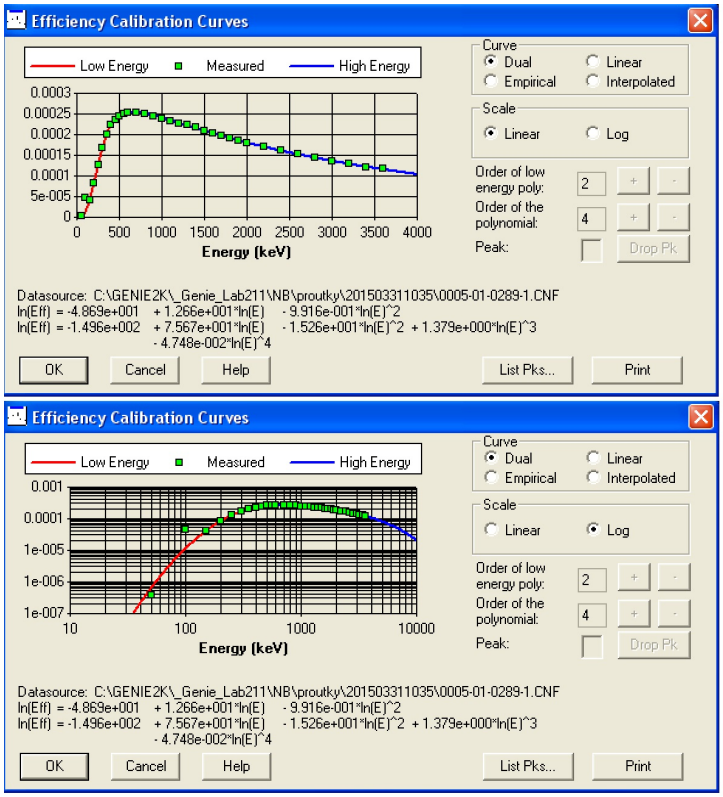

Figure 2.14: Efficiency calibration calculated by MCMP code [36] [37]

example of steps evaluation, where the arrow indicates the steps direction. Firstly the program is using the second derivation to find the peaks, after that their area is calculated by fitting the Gauss function. This area is subsequently corrected to the natural background and then the efficiency correction is made. Finally the nuclides are assign to the peaks by using Genie 2000 database and the results are written to the final report [36].

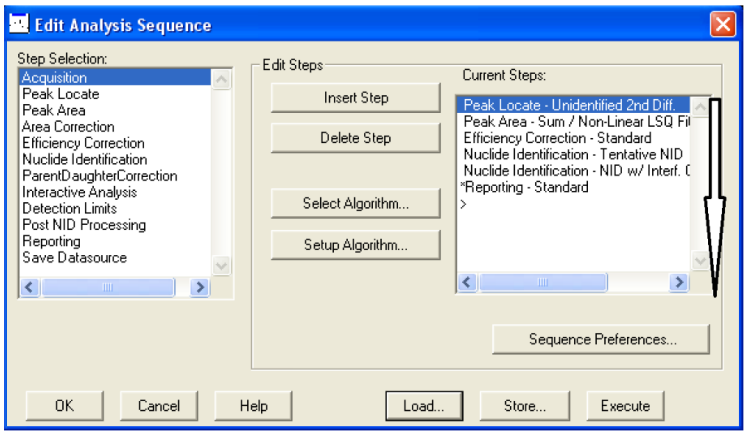

Figure 2.15: Sequence of spectrum evaluation in Genie 2000 [36]

The parameters of sequence are set by the Setup Algorithm. In Figure 2.16 can be seen the Peak Locate setup, where initial and final channel of evaluation, statistic of significant peaks against Compton continuum and the tolerance of

peak position can by set. In Figure 2.17 is more detailed set for the peak fitting [36].

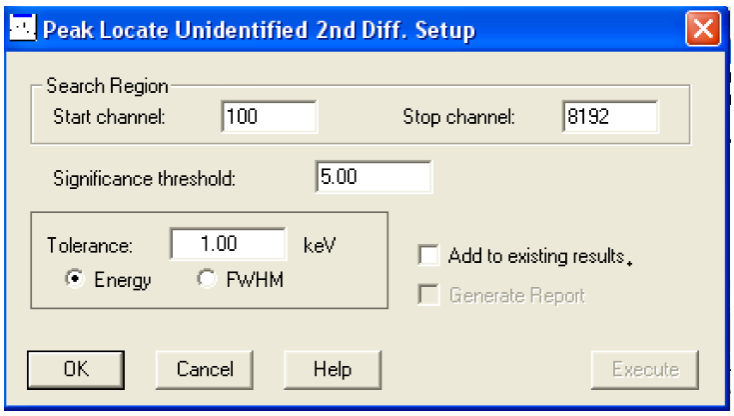

Figure 2.16: Peak Locate setup [36]

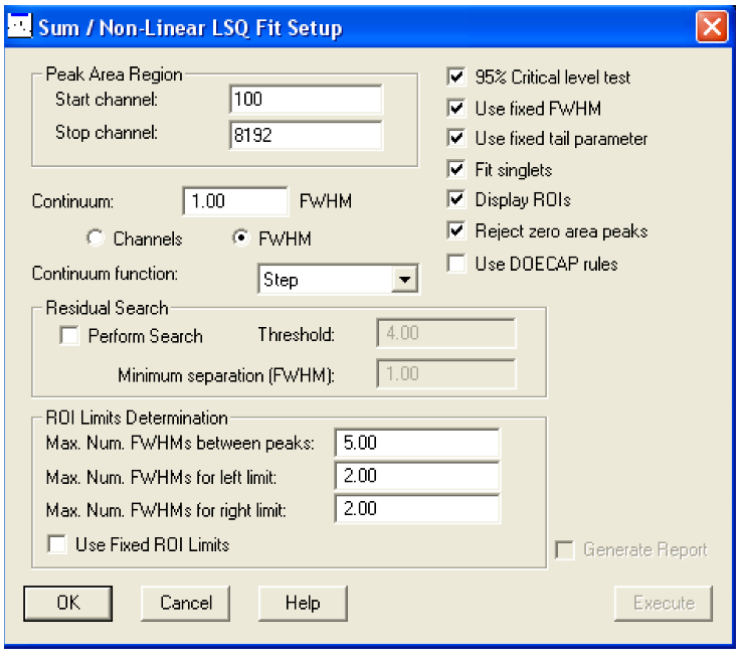

Figure 2.17: Setting of fit the peaks of the spectrum by nonlinear least squares method [36]

The Genie 2000 program output is the final report, where for each peak, the NPA is determined. This area is corrected only to detector efficiency and background radiation, but we need to include the correction for the radioactive decay during the measurement and also the correction to the chosen reference time.

2.3.4 The correction for radioactive decay during the measurement

Due to the measurement of radionuclides with a short half-live in comparison to the time of the measurement we must apply the correction for the decay during the measurement and the correction for the reference time. Correction K has been determined for measured NPA by the equation

$$[e^{\lambda t_d}\frac{\lambda t_{real}}{1-e^{-\lambda t_{real}}}] = K, \tag{2.12}$$

where t_{real} is the real time with a detector dead time, λ is the decay constant and t_d is the time between the chosen reference time and the start of the measurement. Derivation of the equation 2.12 is following:

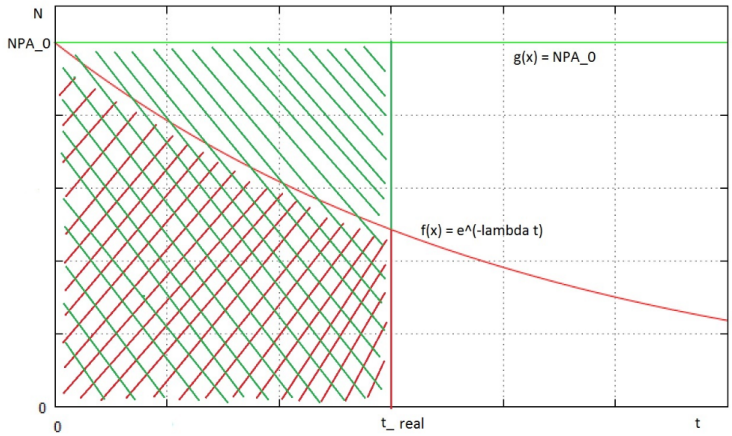

Figure 2.18: The derivation of correction for decay during the measurement

In Figure 2.3.4 the time dependence of NPA during measurement is shown. If the radionuclides with the long-time half-life had been measured (when the time of measurement is negligible), then the NPA would not change in the time of the measurement, thus the green hatched area in Figure would be

$$NPA_0 \cdot t_{real}, \tag{2.13}$$

where NPA_0 is the initial NPA and t_{real} is the real time of the measurement. In our case the NPA during the measurement decreases exponentially, that the area under the curve $e^{-\lambda t}$, which is red hatched in the Figure , needs to be calculated

$$NPA_0\int_0^{t_{real}} e^{-\lambda t}dt = NPA_0(-\frac{1}{\lambda}e^{-\lambda t}|_0^{t_{real}}) = NPA_0\frac{1-e^{-\lambda t_{real}}}{\lambda}. \tag{2.14}$$

By the ratio of the equations 2.13 and 2.14 we obtain the correction for decay during the measurement. This correction is needed to be multiplied by a correction to a chosen reference time. The reference time t_{ref} was set as the start of measurement of the first sample. This correction for the reference time is

$$e^{\lambda(t_{real_i}-t_{ref})}, \tag{2.15}$$

where t_{real_i} is the start of the measurement of each i-th sample. The resulting correction is therefore the multiplication of equation 2.15 with the ratio of the equations 2.13 and 2.14. The final result is the equation 2.12.

The corrected N in the units of impulses per second can be calculated from the equation

$$\frac{NPA}{t_{live}}[e^{\lambda t_d}\frac{\lambda t_{real}}{1-e^{-\lambda t_{real}}}] = N, \tag{2.16}$$

where t_{live} is the live time of the measurement without the dead time of the detector.

2.3.5 The parent-daughter correction

This is a correction for the activity increase of the daughter radionuclide from the parent radionuclide. In the case of radionuclide measurement which has a parent radionuclides with a very short half-life (on the order of seconds), we do not have to perform this correction. But in the case when the parent radionuclide has a long half-life, we need this correction. In this section I will derive this parent-daughter correction.

The transformation of the parent radionuclide is independent of the daughter radionuclide and is governed by the differential equation 2.1. The daughter radionuclide originates from the parent radionuclide and decays itself. The change in the number of its atoms N_2 in the time dt consists of two terms. The first characterizes the rate of its formation, which is equal to the rate of decay of the parent radionuclide, and the second term indicates the rate of its decay through its own transformation. So it applies [38]

$$\frac{dN_2}{dt} = \lambda_1 N_1 - \lambda_2 N_2, \tag{2.17}$$

where N_1 and λ_1 are for the parent radionuclide and N_2 and λ_2 are for the daughter radionuclide. We get the substitution for the parent radionuclide from the decay law:

$$\frac{dN_2}{dt} + \lambda_2 N_2 - \lambda_1 N_1^0 e^{-\lambda_1 t} = 0, \tag{2.18}$$

and after the integration [38]

$$N_2 = N_1^0 \frac{\lambda_1}{\lambda_2 - \lambda_1}(e^{-\lambda_1 t} - e^{-\lambda_2 t}) + N_2^0 e^{-\lambda_2 t}. \tag{2.19}$$

Depending on the mutual ratio of the values of the conversion constants λ_1 and λ_2 of both radionuclides, the conversion equations are simplified in certain cases. As an example I will consider the radionuclides as ^{140}Ba and ^{140}La. The half-life of the parent radionuclide is greater than the half-life of the daughter radionuclide. After a certain, sufficiently long time, which depends on the half-life of the daughter and parent radionuclide, a stationary state occurs. The ratio of activities and the number of atoms of the parent and daughter nuclide is constant, and the number of atoms and the activity of both nuclides decrease with the same half-life, namely with the half-life of the parent nuclide, in our case

with the half-life ^{140}Ba . Time to equilibrium assuming zero amount of daughter radionuclide after the end of irradiation, i.e. in the case when $N_2^0 = 0$ is [38]

$$t_p > 10\, T_1 T_2/(T_1 - T_2). \tag{2.20}$$

For our specific case of ^{140}Ba and ^{140}La, the result is $t_p = 19.35$ days.

Since we do not know the initial amount of ^{140}La at the time of the end of the irradiation, we can use the Genie 2000 program for the parent-daughter radionuclide correction. The correction for the activity of the daughter radionuclide in this program is calculated by the equation [36]

$$D_{0,Corr} = D_0 - k_{PD} P_0 \frac{\lambda_D}{\lambda_D - \lambda_P} [\frac{\lambda_D e^{-\lambda_P t_d}(1 - e^{-\lambda_P t_{real}})}{\lambda_P e^{-\lambda_D t_d}(1 - e^{-\lambda_D t_{real}})} - 1], \tag{2.21}$$

where D_0 is the activity of the daughter radionuclide without correction, P_0 is the activity of the parent radionuclide, k_{PD} is a dimensionless constant determining how much of the parent radionuclide is transformed into the parent radionuclide (in our case it is 1, i.e. 100 % of the parent radionuclide is transformed into a daughter [39]), λ_D is the decay constant for the daughter radionuclide, λ_P is the decay constant for the parent radionuclide, t_{real} is the time of measurement including the dead time and t_d is the time from the reference time to the beginning of the measurement.

2.4 Samples irradiation theory

As was already mentioned, for the cross-section measurement, the activation method and gamma spectrometry measurement were used in my experiments. The question is, how long we need to irradiate the samples for the cross-section result, to obtain as low uncertainty as possible.

The equation $q = N_t \sigma I$ shows the relation among the reaction rate q and density of particle flow I by which the sample is irradiated, to the number of target nuclei N_t and to the cross-section σ. In the case the product of sample irradiation is not radioactive, the product nuclei number increases linearly, but in our case we have product of irradiation, which decay itself, so the number of its produced nuclei depends on the irradiation time. This relation is represented by the equation

$$N(t) = \frac{q}{\lambda}(1 - e^{-\lambda t_{irr}}), \tag{2.22}$$

where t_{irr} is the irradiation time. When the irradiation time $t_{irr} \to \infty$, $N(\infty) = q/\lambda$. We can express this equation in activity [34]:

$$A(t) = A_s(1 - e^{-\lambda t_{irr}}), \tag{2.23}$$

where A_s is the saturated activity, which is the maximum activity that we can achieve during the sample irradiation.

From this equation we can see that the irradiation time is dependent on the decay constant of the resulting radioisotope. The saturated activity is then reached after approximately ten half-lives, but the irradiation is in practice shorter because the saturated activity is reached early for short-lived radioisotopes. For the case of long-term radioisotopes, it is not possible to reach the saturated activity by the irradiation in a reasonably long time.

3. Neutron sources and their use for neutron reaction studies

For the advanced nuclear technology the missing nuclear data have to be supplemented and neutron reactions have to be studied in more details. That is the reason, why the neutron sources are needed. In this chapter the three types of possible neutron sources will be described in more detail, a nuclear reactor, accelerator-based neutron sources and ^{252}Cf.

3.1 Research nuclear reactors

In contrast with power reactors, research reactors serve primarily as neutron sources and are low-power. Technically they are simpler and operate at lower temperatures. Due to this, the heat released by the fission can be taken away just by the natural water flow without a circulation pump (not necessarily). On the other hand, research reactors need more enriched uranium, typically up to 20% of ^{235}U. To summarize the usage of research reactors worldwide, I use the table 3.1 from [40].

Table 3.1: Common applications of 273 research reactors from around the world (2014) [40].

Type of application	**Number of research reactors involved**	**Number of member states hosting utilized facilities**
Teaching and Training	172	54
Neutron activation analysis	125	54
Isotope productions	94	45
Material irradiation	75	29
Neutron radiography	71	40
Neutron scattering	50	33
Transmutation (doping of silicon)	31	20
Geochronology	25	21
Boron neutron capture therapy	23	13
Transmutation (gemstones)	22	13
Other	126	31

More technical information about worldwide research reactors can be found in [41], which is the IAEA's Research Reactor Database, containing technical information on over 800 research reactors in 67 countries.

3.1.1 LR-0 reactor

The LR-0 reactor is used for VVER reactor core characteristic experimental measurement. It is a zero power and light water pool type reactor. Maximum thermal

power is 1 kW and water volume is 20 m^3. The reactor vessel is located in a concrete shielding bunker and is made of high-purity aluminum. In addition to the fuel and absorption clusters, the reactor core also has a dry channels for measurement instruments. The fuel is in the shape of hexagonal prism of type VVER 1000 or VVER 440 [42].

The LR-0 reactor has been designed in a universal manner. It is suitable for physics experiments on VVER-type reactor core with a wide range of cartridge quantities, fuel enrichment, along with various concentrations (0 - 12 gl^{-1}) of H_3BO_3 in the moderator and configurations of absorptive elements in the cartridges. The reactor diagram can be seen in Figure 3.1 and its parameters are summarized in Table 3.2. One of the most important research is the experimental verification of radiation damage to reactor vessels. More details about this reactor can be found in my bachelor thesis [32] and in my master thesis as well [3] (My previous work was mainly focused on the measurements done with LR-0 nuclear reactor in research center in Řež in the Czech Republic). The neutron field of this reactor is well described. To validate spectral average cross-sections it is necessary to have a well-defined neutron field in the reactor (the computational mathematical model of the reactor core). Behind this there are many experiments including the power profile measurement by single fuel assembly pins measurements and I dealt with this issues in my Master thesis, where it is described in detail in chapter 3 [3].

Diameter	3.5 m
Height	6.5 m
Maximum output	1 kW
Maximal output for up to 1 hour	5 kW
Maximum thermal fluence	10^{13} n m^{-2} s^{-1}
Pressure	atmospheric
Temperature	room or up to 70°C after heating
Fuel assembly type	PWR 1000 (Temelín NPP) and PWR 440 (Dukovany NPP)
Active length of fuel assembly	1250 mm
Fuel assembly sheathing	ZrNb
Tablets (fuel cell contents)	UO_2
Enrichment	1.6 - 4.4 % ^{235}U
Controlling method	through the level of the moderator, boric acid
H_3BO_3 in moderator	0 až 12 g/kg
Absorbing clusters	B_4C
Shielding	concrete bunker, cadmium sheet metal, mobile platforms and a gate

Table 3.2: Basic technical parameters of LR-0 experimental reactor in Řež. [42]

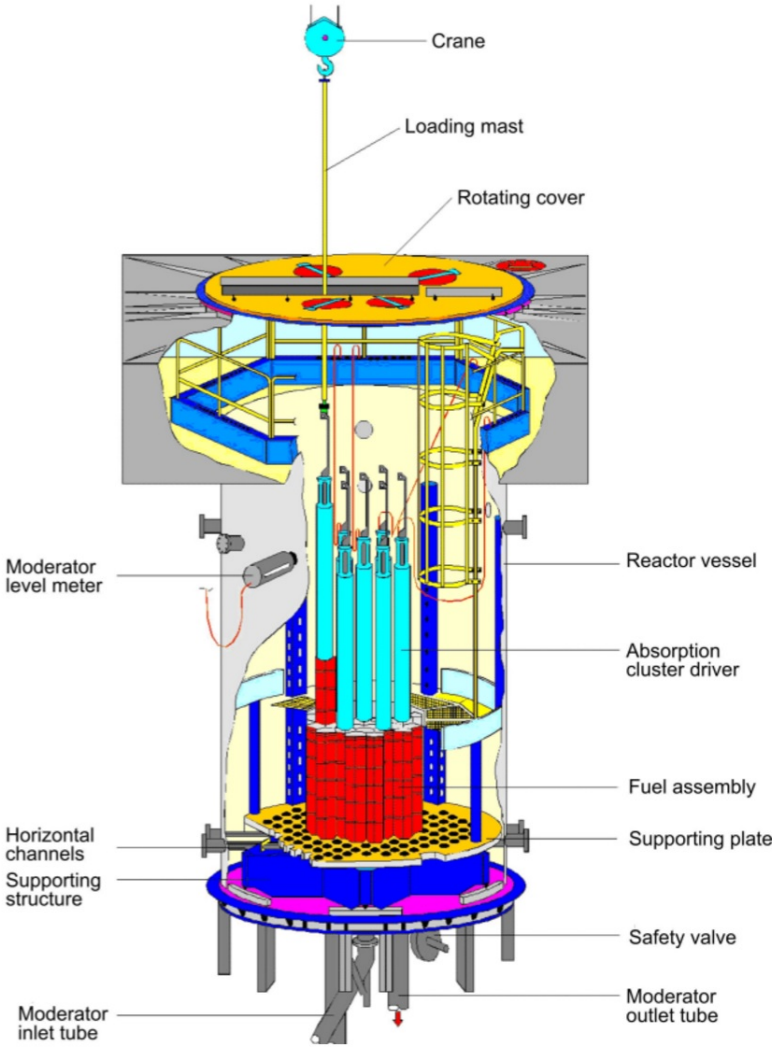

Figure 3.1: The experimental reactor LR-0. [42]

3.1.2 VR-1 reactor

The VR-1 is a school training reactor, located at the Czech Technical University in Prague, mainly for the students of the Faculty of Nuclear Science and Physical Engineering. It is a low power pool type, light water reactor with IRT-4M fuel type (Figure 3.3) with 19.7% of ^{235}U enrichment. Its design satisfies the requirement of easy accessibility to the reactor core in order to provide education to students and training to qualified staff of nuclear industry and is in operation since 1990. Its core is assembled on the top of a core support plate with 8×8 cells in a square lattice geometry (Figure 3.2). The number of fuel elements depends on the core configuration. The reactor is also equipped with five to seven control rods and, of course, experimental channels. Those control rods are made of a cadmium plate sheet wound on an aluminum tube inserted inside a stainless rod. Number of control rods depends on the core configuration [43] [44] [45].

The reactor body has the shape of an octagon and has two reactor vessels which are placed next to each other. One is for the reactor core consisting of fuel cells and second one is used for fuel handling and storage during experiments. Both vessels are interconnected but it is possible to separate them by a watertight

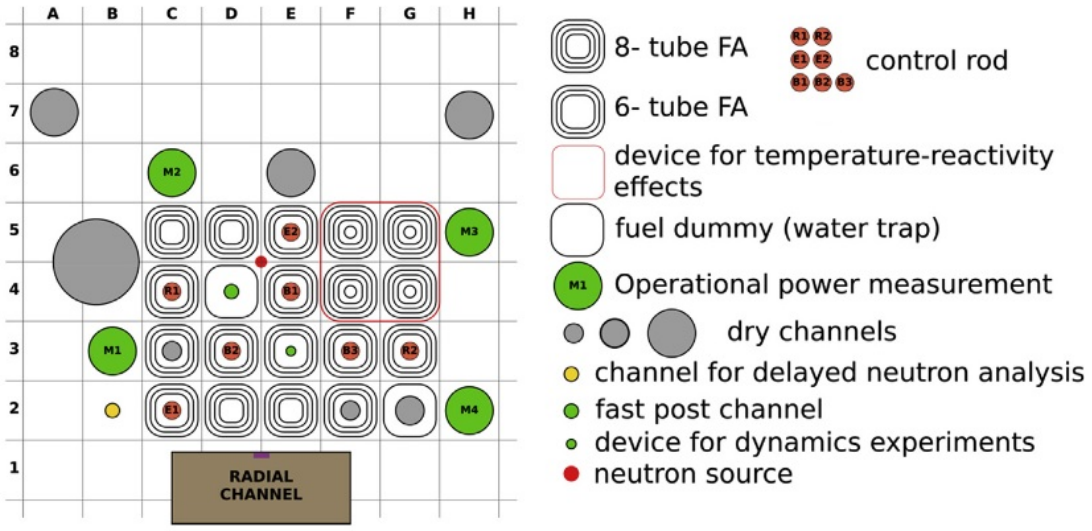

Figure 3.2: The core configuration of VR-1 reactor. [43]

shutter. The reactor vessels are made of stainless steal, their height is 4.7 m, diameter is 2.3 m and both of them have a reinforced bottom to 2 cm.

The fuel for the reactor is supplied by the Russian company TVEL. Due to the low power, the fuel burnout is negligible (less than 0.1 g of ^{235}U burns out in the reactor during 1 year). So the fuel rods service life is determined only by the corrosive properties of their coverage. Alternatively, they may be mechanically damaged. For such case hermetic stainless steal case is prepared in which the damaged fuel cell can be placed. Fuel tubes are available in two versions - 6-tube fuel assembly and 8-tube fuel assembly. Also due to the low power, the heat dissipation takes place by natural flow.

The reactor is being started-up by Am-Be neutron source which is placed inside a shielding container below the reactor vessel and it is moved pneumatically by pressurized air into the reactor core.

The VR-1 reactor parameters are summarized in the Table 3.3.

Table 3.3: VR-1 reactor parameters. [46]

Nominal thermal power	100 W
Reactor type	H_20
Temperature	20°C
Enrichment	19.7% ^{235}U
Geometry	Square
Pressure	Atmospheric
Fuel type	IRT-4M

3.1.3 LVR-15 reactor

The LVR-15 reactor was the first research reactor in the Czech Republic and it has been operating since 1957 in the Institute of Nuclear Physics in Řež near Prague as a VVR-S reactor with a thermal power of 2 MW. After 30 years of operation, the reactor underwent reconstruction which aimed to increase power

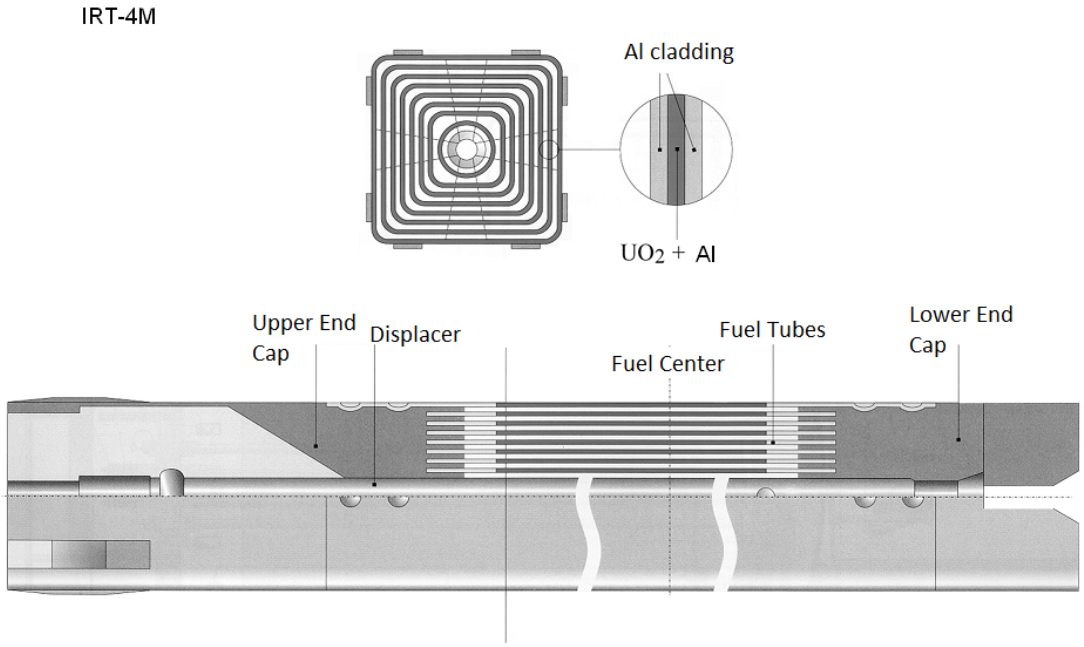

Figure 3.3: IRT-4M fuel scheme. [47]

and increase in safety to the current reactor LVR-15. The reactor serves not only the research purposes but also the production of radiopharmaceuticals and radioisotopes for medical purposes. Its scheme can be seen in the Figure 3.4, where 9 horizontal channels used for experiments (HK1 - HK9) can also be seen.

It is a light water tank-type research reactor placed in a stainless steel vessel under a shielding cover. The reactor vessel diameter is 2300 mm, height is 5760 mm and the weight without water is 7900 kg. The fuel type is the same as for VR-1 reactor, IRT-4M. This reactor operation runs in three weeks long campaigns. Technical parameters are summarized in the Table 3.4.

IRT-4M fuel (Figure 3.3) has active length of 600 mm and its cladding is made of aluminum. The reactor core contains from 28 up to 34 fuel assemblies depending on the needs of the current campaign. Also 12 fuel assemblies are constructed for inserting control rods (8 of them are compensation, 3 are safety rods and 1 is automatic regulator). The possible core configuration can be seen in Figure 3.5, where 5 middle core blocks contain cases with highly enriched ^{235}U for the radiopharmaceutical ^{99}Mo production. Some of published papers using LVR-15 research reactors are [48], [49], [50], [51] and [52].

Table 3.4: LVR-15 reactor parameters. [47]

Maximal thermal power	10 MW
Reactor type	H_20
Temperature	max. 56°C
Enrichment	19.75% ^{235}U
Absorber	B_4C
Pressure	Atmospheric
Fuel type	IRT-4M
Water volume	22 m^3

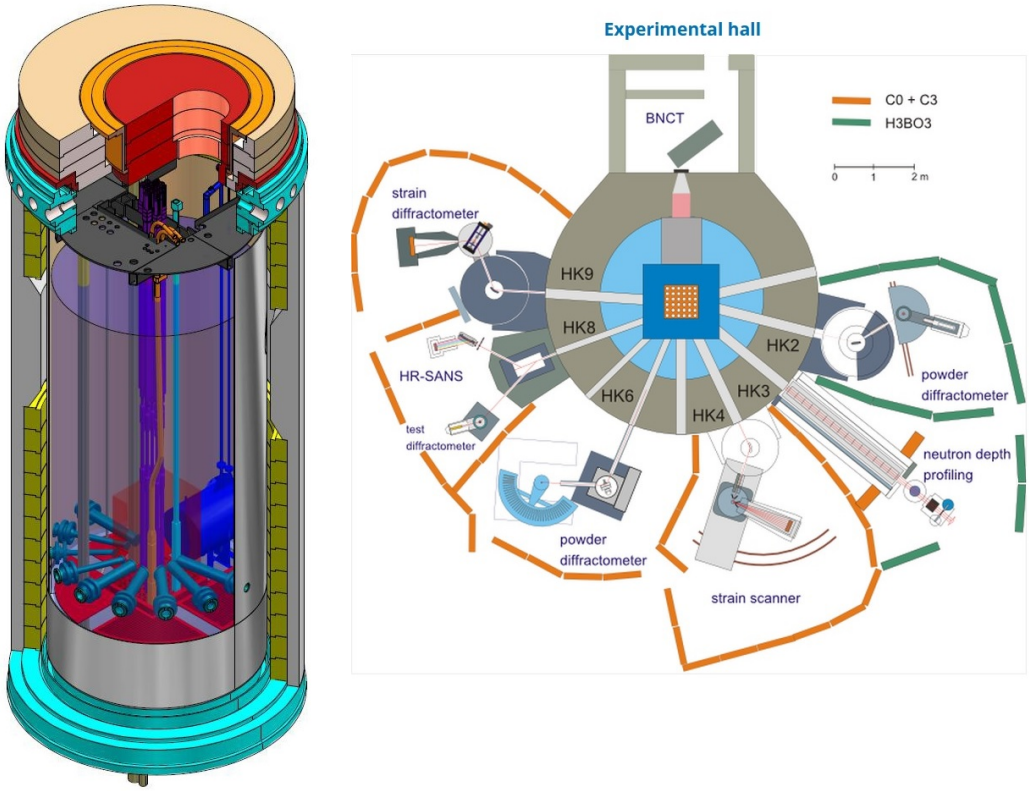

Figure 3.4: LVR-15 reactor scheme. [47]

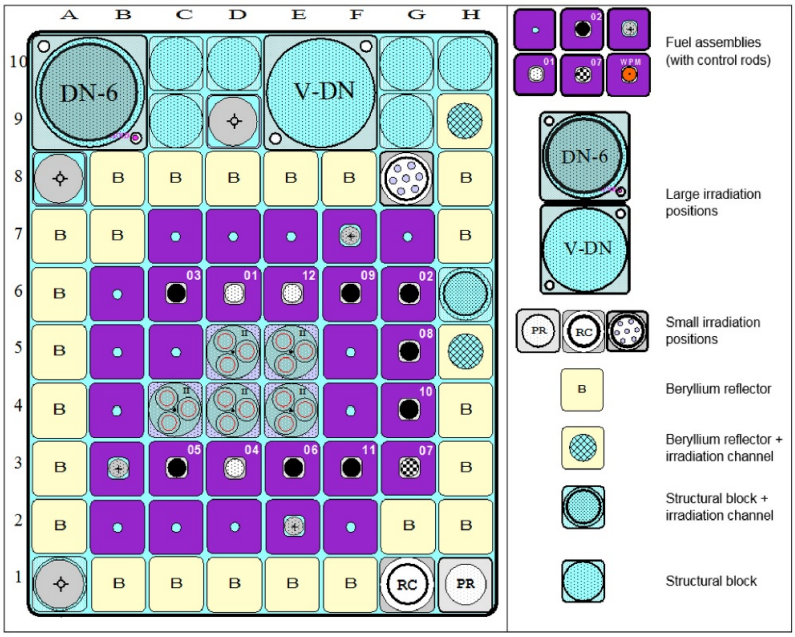

Figure 3.5: LVR-15 core configuration. [48]

3.2 Accelerator as a neutron source

Accelerator-based neutron sources have an important role in the field of higher neutron energies. Nuclear reactor mean value of neutron energy is approximately 2 MeV and the vast majority of produced neutrons are below 10 MeV. So in the

range of 10 MeV up to hundreds of MeV we need an accelerator as a neutron source. In comparison with a cross-section measurement in the nuclear reactor, we are able to measure the differential cross-section for each neutron energy thanks to the mono-energetic spectrum of such neutron sources.

Neutron has a neutral charge, so it can not be accelerated by an electric field. The fast neutrons are produced by specific reactions of accelerated charged particles with some kind of a suitable target. The neutron spectrum is given by this target material, the target thickness and the characterization of the accelerated charged particle.

The continuous spectrum is mostly produced in the thick target where the beam ions gradually lose their energy in the target itself. On the other hand, mono-energetic spectrum is mostly produced in thin targets. The continuous spectra are widely used in the study of material radiation damage, testing of radiation resistance of electronic devices, neutron radiotherapy or for integral validation of nuclear data. Mono-energetic neutron spectra are mainly used for measurement of discrete values of cross-sections for specific neutron energies to obtain the excitation function. The mostly used target materials are described in more detail in the following subsection [53] [54].

3.2.1 Target materials

Among targets used in accelerator driven neutron sources are mainly deuterium, lithium and beryllium or high atomic number materials.

The most effective reaction for neutron production is spallation, which produce white neutron spectrum, where no energy dominates significantly. It is the reaction caused by the collision of a high-energy proton with a high atomic number material such as lead. Proton energies in this case are relativistic in the range of hundreds and thousand of MeV. De Broglie projectile wavelength at these energies is significantly smaller than the diameter of the target nuclei, so the impact particle does not interact with the nucleus as a whole, but with individual nucleons. Neutrons produced in spallation reactions are of three types. First ones are produced during the collisions of relativistic protons with nucleons. These neutrons also have relativistic energies and thus can cause other spallation reactions and their momentum is mainly of forward direction. Second type of neutrons are those which are emitted by the nucleus before the thermal equilibrium is reached. These neutrons have energy in the order of tens of MeV. Third type of neutrons are those, which are emitted by nucleus deexcitation and their energies are in the order of units of MeV. The first spallation neutrons can trigger further spallation or a fission process to produce the next generation of neutrons, but not in meaning of a chain reaction, so this process is non-critical and it is used in sub-critical nuclear reactors like the research reactor MYRRHA, as was mentioned above in 1.2. But this is a very expensive way how to produce neutrons because to produce the high energy proton the big accelerator is necessary. This neutron production was studied for example in [55] with activation detectors. As an examples of spallation sources in the word I would like to mention for example Time-Of-Flight (n_TOF) facility at the European Laboratory for Particle Physics (CERN), which is a pulsed white-spectrum neutron spallation source designed to study neutron-nucleus interactions. [56] Another would be the Eu-

ropean Spallation Source (ESS) which is presently under construction in Lund, Sweden [57].

A cheaper way of neutron production is by the reaction of protons with energies up to 100 MeV with light targets such as p-Be or p-Li reactions which produces mostly the quasi-monoenergetic neutron spectrum

$$\begin{aligned} p + {}^{7}Li &\rightarrow {}^{7}Be + n - 1.65\,MeV \\ p + {}^{9}Be &\rightarrow {}^{9}B + n - 1.85\,MeV \end{aligned} \tag{3.1}$$

Their threshold energies are 1.88 MeV for Li and 2.08 MeV for Be. The thick Be target is mostly used for production of a continuous neutron spectrum. Its advantage is the high melting point temperature for Be, which allows us to operate it at high charged particle intensities. Also the cross-section of protons or deuterons with this material is high in the range of units and tens of MeV. Disadvantage of Be is its toxicity and this makes the manipulation with it complicated. For the mono-energetic neutron spectrum thin Be target can also be used, but in this case, Li target is used more often. Relatively low energy impact protons (no more than tenths of MeV) produce a purely mono-energetic neutron spectrum. For higher energies of impact protons, there is an extension of continuous neutron background and then we get quasi-mono-energetic neutron spectrum. This background is significant, but it can be separated by a suitable correction (this will be mentioned later in the subsection 4.2.4). Thick Li target can be used also for the production of continuous neutron spectrum but Li has much lower melting point temperature in comparison with the Be (1287 °C for Be and 180.5 °C for Li). One of the interesting Li reaction is ^{7}Li(d,n)^{8}Be. This reaction produces a neutron spectrum with the mean value around 14 MeV which is convenient for the imitation purposes of the fusion reactor neutron spectrum.

For the neutron production deuterium and tritium reactions (^{2}H(d,n)^{3}He, ^{3}H(d,n)^{4}He, ^{3}H(p,n)^{3}He) can also be used. Here the mono-energetic neutron spectrum is produced. Deuterium is usually used in the form of gas or heavy water D_2O. In the case of gas deuterium it is necessary to have a high pressure in the target to achieve required target density. Disadvantage of this gas target is the possibility to use only the low particle intensity in an accelerator because with the high intensity a local heating may occur and thus a density reduction in the target. Due to this the liquid deuterium target is mostly used. But even here a very good cooling system is needed to minimalize the occurrence of steam bubbles.

It is also possible to use solid tritium target which is widely used for 14 MeV neutron production by the interaction of target with deuterons. Those targets are usually produced by evaporation of Ti and Zr layer on a thin Cu backing, with a subsequent absorption of ^{3}H gas in it. Problem of those neutron generators is their high operation cost.

3.2.2 NG-2 and U-120M

The production of the fast neutrons at the Institute of Nuclear Physics of the Academy of Sciences of the Czech Republic (NPI CAS) is mainly ensured by the neutron source NG-2, operated by the cyclotron U-120M. More neutron sources exist (research reactors, AmBe source, PuBe source or Cf and PET center), but

this one was used for our purposes, which is why it is described here in more detail.

Cyclotron itself is composed of two duants and charged ions are accelerated in the gap between the duants using an electric field with periodically changing polarity. Duants curve the ion trajectory via magnetic field. The trajectory of ions is circular with increasing radius. The cyclotron frequency has to be constant in order to accelerate more than one particle beam effectively, but in classical cyclotron with constant magnetic induction. It is only possible in the non-relativistic case where the mass change is negligible. Cyclotron modification means increasing the magnetic induction with increasing ion radius, which allows to compensate the relativistic growth of the particle mass. This modified device is an izochronous cyclotron.

Cyclotron U-120M is placed in Nuclear Physics Institute of CAS in the Czech Republic and it is able to produce a continuous neutron spectrum or quasi-mono-energetic neutron spectrum using different neutron sources. This izochronous cyclotron is in operation since 1977, provides beams of accelerated ions (p, H^-, D^+, D^-, $^3He^{2+}$, $^4He^{2+}$) and can operate in wide range of energies (1-55 MeV). Beams of accelerated particles with currents from units of nA to tens of μA are intensively used for a wide range of basic and applied research experiments. The acceleration modes of positive and negative ions differ not only in energy and intensity but also in the way they are extracted. Positive ions are extracted by means of three sections of electrostatic deflection system with a magnetic kicker. Negative ions are extracted by a stripping method using a thin carbon foil. The parameters of accelerated beams are summarized in 3.5.

NG-2 is a target station connected to the negative beam of U-120M accelerator. Depending on the target material this station produces a continuous neutron spectrum or a quasi-mono-energetic neutron spectrum. This station also ensures the cooling of the target and defines the positions for sample placement [58] [59].

Table 3.5: Parameters of accelerated beams from the U-120M cyclotron[58].

Ions	**Energy [MeV]**	**Max. current** [μA]
H^+	1-37	>200
H^+	6-25	5
H^-/H^+	6-37	50-30
D^+	2-20	>80
D^+	12-20	5
D^-/D^+	11-20	35-20
$^3He^{2+}$	3-55	20
$^3He^{2+}$	18-52	2
$^4He^{2+}$	4-40	40
$^4He^{2+}$	24-38	5

3.3 ^{252}Cf as a neutron source

Last but not least, mentioned in this thesis, is the ^{252}Cf neutron source, which is the only neutron spectrum standard with a spontaneous fission neutron spectrum.

This standard spectrum is tabulated within the range of $1 \cdot 10^{-10}$ MeV to 30 MeV. The IAEA evaluation is based on [60] within the range of 0.1 MeV to 20 MeV. Above 20 MeV and below 0.1 MeV the spectrum is loaded with large uncertainty due to the lack of experimental data.

The ^{252}Cf(s.f.) source is based on a spontaneous fission with a half-life of 2.645 years, so this is one of its disadvantages, because it needs to be replaced regularly. Another disadvantage is that it cannot be turned off, so shielding is required when it is not being used. During the spontaneous fission, a number of fast neutrons is emitted. This neutron spectrum is considered as a standard and thus it is a suitable neutron source for the nuclear data measurement. The integral cross-sections data can usually be measured much more accurately than differential nuclear data, so this neutron source is important for improving integral performance [61]. More information about the cross-sections measurement using the ^{252}Cf neutron spectrum is described in several previously published papers by my colleagues, in one of which I was also involved ([62], [63], [64] and [65]). As an example of a measurement with the Cf source worldwide I mention [66] and [67] as examples.

4. Specific cross-section measurement experiments

There are many possible methods, how to experimentally obtain cross-sections, but our focus is mainly on an activation method. The small activation foil or the suitable amount of powder sample is placed into the neutron field (^{252}Cf, reactor or accelerator) and irradiated. For this work were specifically selected materials of Y, Cu, Ti, Fe, and Nb.

The material is chosen based on the reaction we are interested in. It is usually a thick foil, wire or pressed powder, ideally pure material consisting of just one isotope. In the target material, new nuclei are produced during the irradiation in the neutron field by the ongoing reactions. Irradiated activation material is subsequently analyzed by gamma-ray spectrometry at High Purity Germanium (HPGe) detector. Measured gamma spectrum contains direct reaction products or a product of their decay series. Due to this it is possible to determine the number of nuclei produced by the reaction during the whole irradiation time. Detectors and methodology for gamma radiation detection and gamma spectrum analysis are described in a number of textbooks and review papers ([68],[69],[70], [71]) The necessary corrections for various experimental conditions are also discussed here. Specific formula for calculation of the reaction yield is [72]

$$N_{yield} = \frac{S_{peak} C_{abs}(E_\gamma) C_{stab}}{I_\gamma \epsilon_P(E_\gamma) C_{COI} C_{square}} \frac{t_{real}}{t_{live}} \frac{e^{\lambda t_0} t_{real}}{1 - e^{-\lambda t_{real}}} \frac{\lambda t_{irr}}{1 - e^{-\lambda t_{irr}}}, \tag{4.1}$$

where S_{peak} is the gamma peak area, C_{abs} is self-absorption correction, C_{stab} is a neutron beam stability, I_γ is gamma emission probability, ϵ_P is detector efficiency, C_{COI} is true cascade coincidences correction [73], C_{square} is square-emitter correction, t_{real} is a real time of HPGe detector measurement, t_{live} is a live time of HPGe detector measurement, t_{irr} is a irradiation time, λ is a decay constant and t_0 is time between end of the irradiation and start of the HPGe detector measurement. The fraction t_{real}/t_{live} represents the correction to detector dead time. The last two fractions represent the correction to reference time (the end of irradiation), correction to the decay during the measurement and correction to the decay during the irradiation, which was derived in chapter 2.

The self-absorption correction and the square-emitter corrections were calculated in MCNP[37] by my colleagues. The C_{COI} is determined from the equations, which were published in [74], where this correction were obtained for each nuclide taking into account the decay data from DDEP/BIPM-5 database. The equations for the most intense gamma emissions of a selected nuclides are summarized in [74]. Those equations can be used for our purposes. As an example, I will show the equations for ^{60}Co

$$\begin{aligned} 1173.2\,keV &\rightarrow F^S(E) = [1 - 1.0001\epsilon^T(1332.2)] \\ 1332.2\,keV &\rightarrow F^S(E) = [1 - 0.9988\epsilon^T(1173.2)], \end{aligned} \tag{4.2}$$

where $F^S(E) = C_{COI}$ and ϵ^T is the total detector efficiency for the photons of given energy, which was calculated in MCNP [37].

The reaction rate is than determined by the equation

$$q = \frac{N_{yield}}{N} = \frac{N_{yield}}{\frac{mN_a}{M_m}}, \tag{4.3}$$

where N is the number of nuclei in the irradiated sample, m is a sample mass, N_a is Avogadro constant and M_m is molar mass. More detailed derivation of reaction rate equation is described in thesis attachments.

4.1 Reactor experiments

In this section all my work will be summarized, which was mainly focused on spectral averaged cross-section measurement in the neutron field of a nuclear reactor. During my research, many experiments were performed ([72], [75], [76]). Spectral averaged cross-sections were measured in the LR-0 reactor and the research behind it will shortly be discussed in the following three subsection (more details can be found in [3]). Other subsections in this section will describe in more detail the possibility of spectral averaged cross-sections measurement using VR-1 reactor with more enriched fuel, where the burn up effect need to be included.

4.1.1 LR-0 reactor experiments

For the cross-sections measurement using the nuclear reactor it is essential to know the neutron field in a given position of the reactor. My previous work was focused on the measurement with LR-0 reactor.

As a summary of my previous work in LR-0 neutron spectrum, I will mention cross-sections measurements of ^{90}Zr(n,2n), ^{55}Mn(n,2n) and ^{127}I(n,2n) reactions. All of those three samples were in form of encapsulated ZrO_2, MnO_2 and NaI. An example of ZrO_2 capsule can be seen in Figure 4.1. This is readily available form and this choice includes the suitable neutron properties of oxygen, low absorption and scattering. The samples were irradiated in the special core, which is well characterized LR-0 reactor zone, and can be seen in Figure 4.2. After the irradiation, the capsules were measured at HPGe detector. All three samples are big in volume, so the good detector characterization for the efficiency calculation is needed (see the subsection 4.1.3). Experiment results are summarized in Table 4.1.

Since this issue was the subject of my Master thesis, the details are not discussed here. More details can be found in my papers [75], [77] or in my Master thesis [3]. In the following subsection, the characterization of its neutron field is summarized. In the second subsection the HPGe detector characterization, which is also essential for cross-section determination, is mentioned. It is also important to note that, in the case of cross-sections measurements in a reactor field, we obtain a spectrum averaged cross-section (SACS) not a differential cross-section for each neutron energy as we can get from accelerator measurements. This integral cross-section for the whole neutron spectrum is primarily used for the differential cross-section measurement validation or, in the case when the cross-section is well known, the measurement in reactor spectrum is important for the refinement of ^{235}U fission spectrum above 10 MeV. Nuclear data libraries vary widely

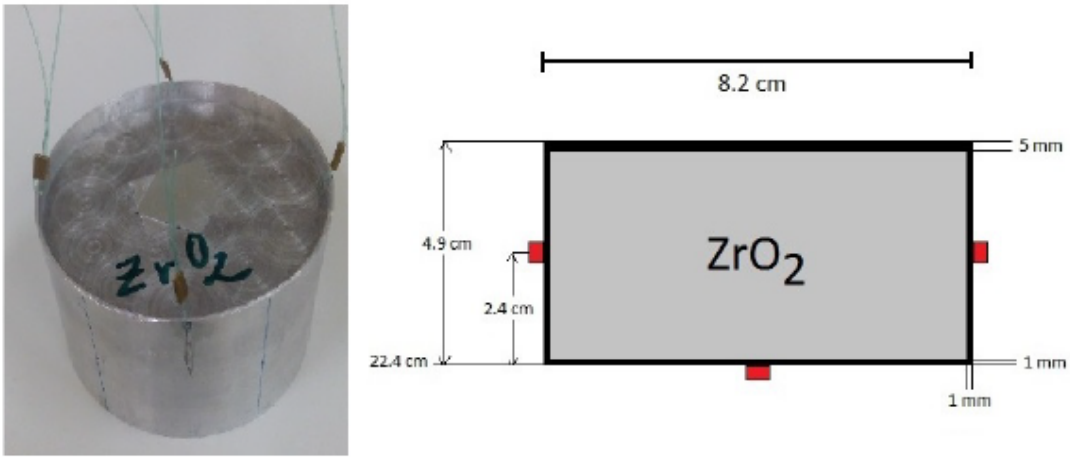

Figure 4.1: The photo and the scheme of ZrO_2 capsule with the activation foils positions (red rectangles). [75]

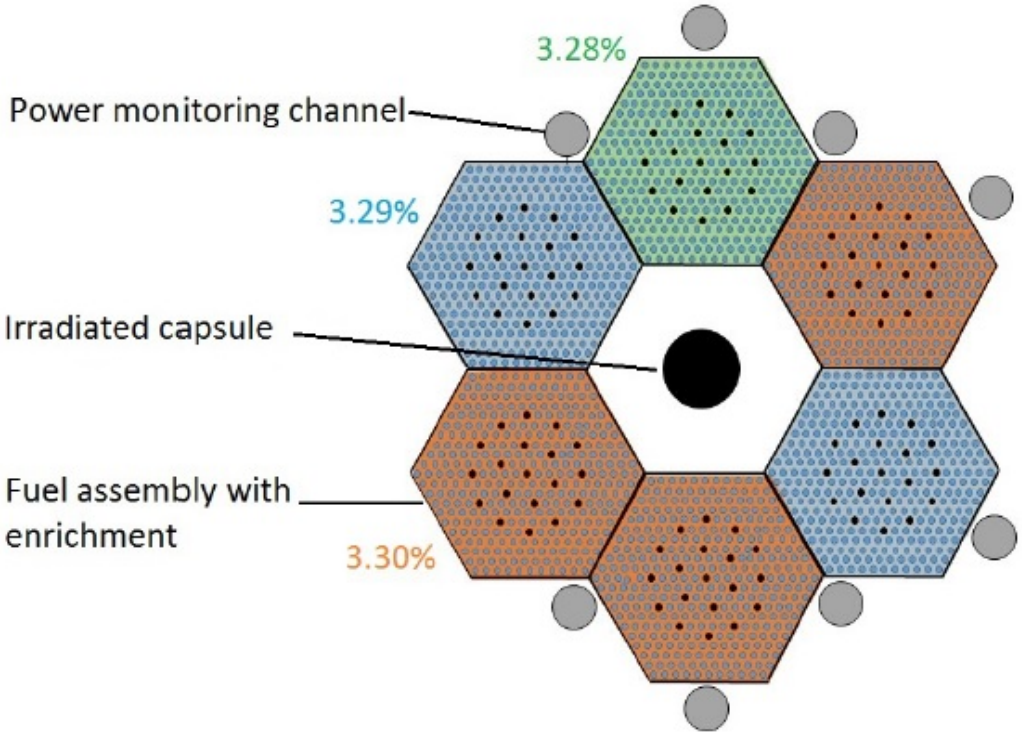

Figure 4.2: Radial plot of the LR-0 special core with capsule position. [75]

in this area. As an example, in the Figure 4.3 is shown a comparison between ENDF/B-VIII.0 and JEFF-3.3 neutron fluxes ^{235}U PFNS. It can be seen that above 15 MeV it starts to vary, but the number of neutrons above 15 MeV is approximately 2.87E-05. Overall, the number of neutrons in the reactor spectrum with the energy above 10 MeV is small.

Table 4.1: Results of ^{90}Zr(n,2n), ^{55}Mn(n,2n) and ^{127}I(n,2n) reactions cross-section [75].

	^{55}Mn(n,2n	**^{127}I(n,2n)**	**^{90}Zr(n,2n)**
A [Bq]	8.046	453.872	47.91
q [s^{-1}]	5.13E-21	2.78E-20	2.40E-21
SACS in reactor spectra > 10 MeV [μb]	163.6	858.4	76.8
Cross-section in ^{235}U PFNS [mb]	0.2393	1.2087	0.107
Uncertainty [%]	6.45	4.36	3.88

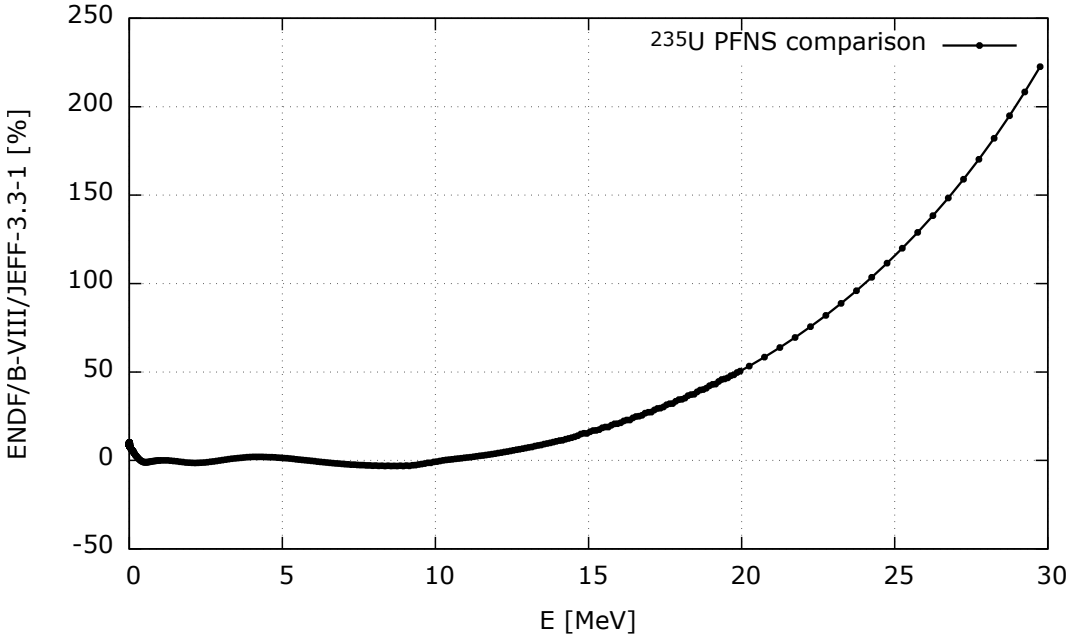

Figure 4.3: Difference between ENDF/B-VIII.0 and JEFF-3.3 ^{235}U PFNS. [48]

4.1.2 Characterization of LR-0 neutron field

Well characterized LR-0 zone is the reactor core with 6 fuel assemblies and 1 dry channel in the middle of this reactor core. This reactor zone arrangement is called special core. This characterization is briefly described in chapter 3 in my Master thesis [3]. To validate the reactor model it was necessary to compare two results of calculations and experiment - critical height and power profile. The criticality experiment was performed with an empty dry channel in the middle of reactor core and with graphite inside this dry central channel. The power profile of the LR-0 reactor was measured by gamma activity of single pins from fuel. The advantage of LR-0 reactor is the possibility of disassembling the fuel into individual rods. Those specifically chosen rods from reactor core were measured in a laboratory specially designed for this purpose. The lead shielding was used to reduce the contribution from non-collimated parts of fuel pins. An automatic movable and rotating mechanism was used for the measurement, so the pin rotated during the measurement and automatically shifted its measurement positions after finishing

the previous measurement, to reduce manipulation with the fuel and personal radiation exposure. The permeability of the lead shielding and its correction determination was the main part of my Bachelor thesis [32] For a better model, which is not the subject of this work, more experiments were performed and are briefly described in my Master thesis as well [3].

4.1.3 Characterization of HPGe detector

This HPGe detector characterization is important because the detector efficiency is needed for the cross-section calculation. I dealt with this problem in chapter 4 of my Master thesis [3]. For the detector model and thus the determination of detector efficiency of non-point source, the detector parameters need to be obtained. Not all detector parameters are provided by the detector manufacturer and some parameters can be different (see Table 4.2) or can change over the detector lifetime (detector insensitive layer). The detector characterization was mainly based on the detector radiogram, which was made by detector irradiation in the distance of 5 meters from pure ^{137}Cs gamma source. Important values for the detector model were measured from the radiogram . Additionally, the thickness of detector insensitive layer was measured experimentally, using special lead collimator, which allowed the measurement in 90° as well as in 45° [78]. This result can be seen in Figure 4.4.

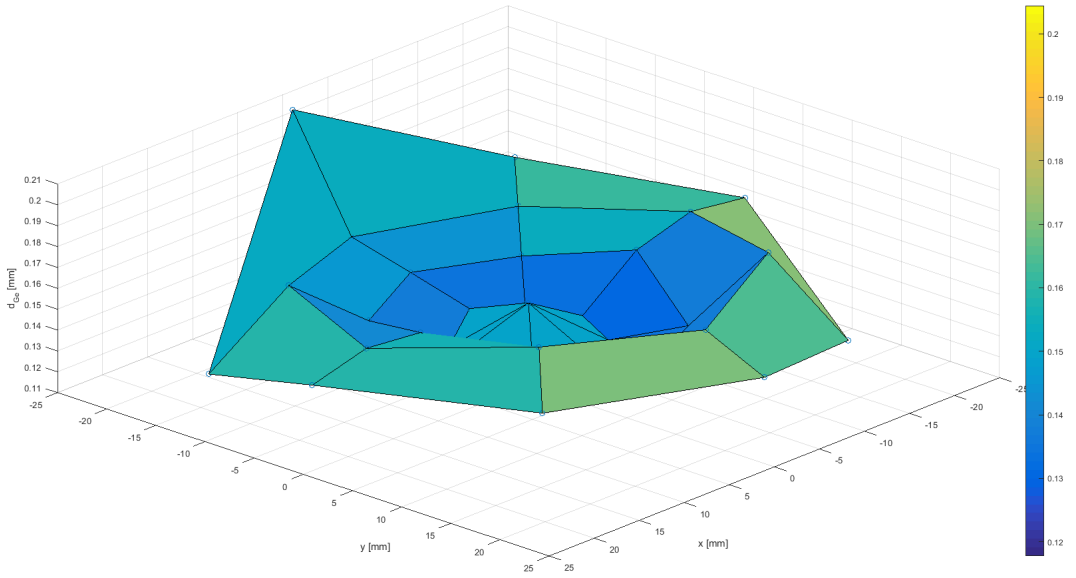

Figure 4.4: 3D graph of detector insensitive layer thickness [3].

4.1.4 VR-1 reactor experiments

During my doctoral research I focused on the reactor cross-sections measurements first to follow up on my previous work. My Master thesis was focused on the cross-sections measurements in LR-0 reactor neutron spectrum. In many, previously published, papers (for example [72], [76] or [79]), it was proven, that this reactor neutron field is close to the ^{235}U(n,f) PFNS [79]. I will mention the measurement of ZrO_2 capsule in LR-0 reactor as an example. This material is important in

Table 4.2: Experimentally determined detector parameters from radiogram [75].

	Measured value [cm]	**Uncertainty [cm]**	**Manufacturer data [cm]**
Crystal radius	3.003	0.010	3.059
Crystal length	5.525	0.020	5.58
Hole radius	0.482	0.011	-
Hole length	4.420	0.035	-
Cap thickness (aluminum)	0.143	0.013	0.1
Pin radius	0.331	0.024	-
Pin contact length	0.369	0.026	-
Gap thickness (vacuum)	0.480	0.018	0.4

reactor physics because the fuel cladding is from zirconium and thus the cross-section of this material needs to be well known. Also due to the fact, that the obtained result of Zr cross-section was in good agreement with the measurement of Mannhart [80], it was one of the proofs that the LR-0 reactor core is well described. Additonally various samples were measured, such as Mn, Ta, Fe or Y in LR-0 reactor core in a special holder for measurement of axial and radial inhomogenities of neutrons flux. The result was that the neutron field is nearly homogenous [72]. The neutron spectrum in the core is, in general, not identical to the fission one because of the scattering reactions. But it was shown in [79], that PFNS and reactor spectra have a similar shape from a certain energy boundary. The lower limit is around the energy of 5.5 - 6 MeV. This is sufficient for us as we investigate reactions with a threshold above 5 MeV.

However, the question whether the ^{238}U(n,f) fission neutrons, which make up about 5% of neutron field in the LR-0 reactor core, affect the measurements or not, was still open. In order to confirm the use of the methodology, an experiment in VR-1 reactor, which has higher enriched fuel, was carried out. Spectra of those reactors varied in the region of low energy due to better moderation in VR-1 reactor (see the Figure 4.5).

During the VR-1 experiment I cooperate with my colleagues from CTU, who have an MCNP model of the VR-1 reactor [79]. In the following subsection I describe calculations for this experiment and in the last subsection I describe the experiment itself with its results.

4.1.5 VR-1 calculations

As was mentioned, for the cross-section measurement, neutron spectrum in the reactor is needed. This VR-1 spectrum with a specific reactor core configuration (Figure 3.2), called C13 zone, was calculated in criticality mode of the MCNP6 code. The spectrum has been calculated using the track length estimate of the cell flux in 640 group structure in the cylindrical volume with a diameter of 6 cm and a thickness of 0.5 cm in the position corresponding to a foil position. This volume was subdivided using mesh tally angularly to four quadrants and radially

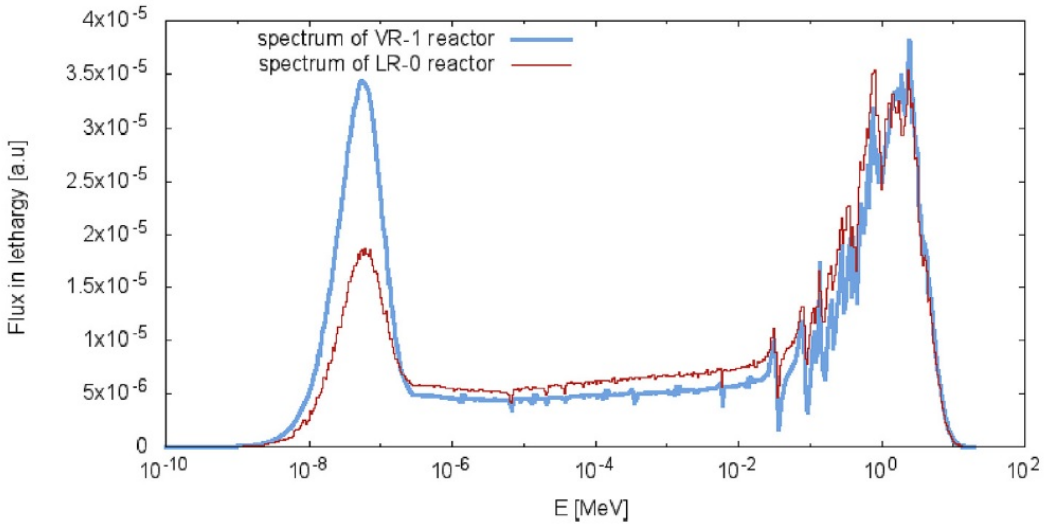

Figure 4.5: LR-0 and VR-1 reactor spectra comparison. [43]

with a step of 0.5 cm. In the whole volume the average thermal neutron flux density was calculated. By this average density was divided the thermal neutron flux in each volume segment. The thermal neutron flux difference in the volume segments can be seen in the left panel of Figure 4.6 beside the average value. But although the thermal neutron flux is consistent, the reaction rate distribution for ^{58}Ni(n,p) reaction has more significant inhomogeneity. The reaction ^{58}Ni(n,p) has higher threshold energy, so the fast neutron flux distribution is less consistent in comparison with the thermal neutron flux. This effect can be seen in the right panel of Figure 4.6. This inhomogeneity can be caused by the fuel geometry, which is influenced by the manufacturing tolerances. Also the zone configuration can affect it (for example the positions of control rods or dry channels).

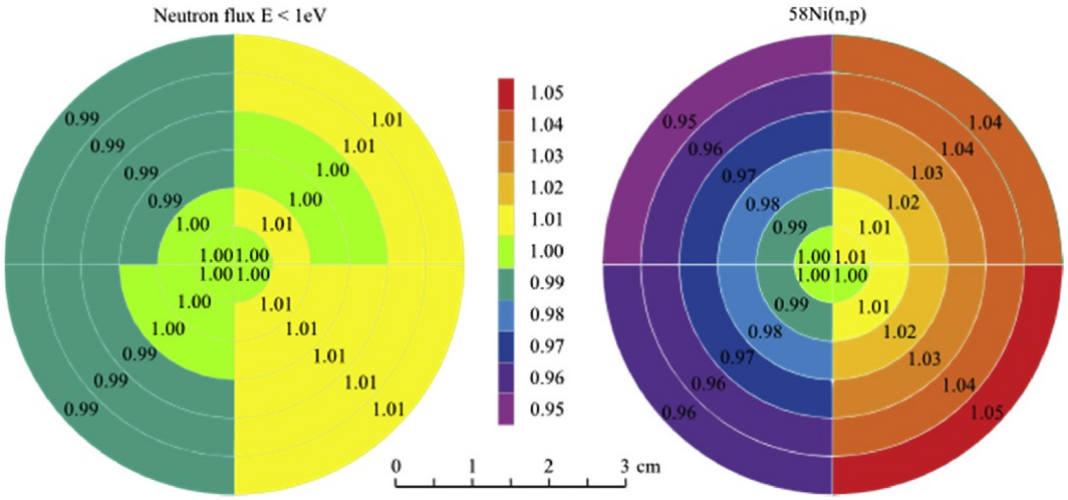

Figure 4.6: Calculated inhomogeneity at the foil irradiation position in the reactor radial channel. [43]

The VR-1 reactor neutron spectrum was measured by stilbene detector and compared with the calculation model [81] which was obtain by the criticality

measurement [82], reaction rates determination [83] and by kinetics parameters [84].

Additionally after this VR-1 experiment, my colleagues continued with the research [44]. In general, a neutron spectrum in the core is not identical to the pure fission one because fission neutrons undergo many scattering reactions. But it is possible to show that ^{235}U PFNS and reactor spectra have a similar shape from a certain energy boundary. This limit is important for experiments, because when the studied reaction threshold is over this limit, the spectral averaged cross-sections in PFNS can be derived from the reactions measured in the reactor core. The evaluation of the neutron spectrum measurements in three different thermal-reactor cores shows that this lower limit is around the energy of 5.5 – 6 MeV. Above this energy the reactor spectra becomes identical with the ^{235}U PFNS. IAEA ENDF/B-VIII.0 PFNS is within 5% of the measured PFNS from 10 to 14 MeV in the LR-0 reactor, while ENDF/B-VII evaluated PFNS underestimated measured neutron spectra. This important conclusion was published by my colleagues in [79], therefore the experiment in the VR-1 reactor plays a key role in this research.

4.1.6 Measurement and results

For VR-1 experiment, the foils of Ni, Nb, Cu, Y, Ti and Fe were chosen (the same materials as was used for the LR-0 reactor measurements). The most important reaction in this experiment was ^{89}Y(n,2n)^{88}Y, because it has high reaction threshold and thus, if the VR-1 has a different tail of ^{238}U PFNS, the results will vary. The foils were irradiated in the middle of the VR-1 reactor radial channel for 8 hours with a nearly constant reactor power of 340 W. The sample of Cu had bigger dimensions, so the corrections for flux loss and spectral shift were necessary (effect of the case when the Cu foil is upside-down was about 1.14%, which was measured experimentally with 0.5% uncertainty - see Table 4.3). The HPGe detector efficiency was calculated in the MCNP6 code. The thickness of the detector insensitive layer was also experimentally measured for the detector model. More detailed information was described in chapter 4 of my Master thesis [3]. The efficiency example for the detector, which was used for the measurement, can be seen in Figure 4.7, where not only calculated efficiency points at different distances from the detector end cap are shown, but also some points measured by using standard point sources such are ^{60}Co, ^{88}Y, ^{152}Eu, ^{137}Cs, ^{241}Am and more. Then in Figure 4.8 the detector efficiency calculations and measurement comparison is shown.

The final ^{235}U SACS was then determined by the equation

$$\overline{\sigma} = \frac{q}{K \times \int_{E>threshold} \phi(E) dE} \times C, \tag{4.4}$$

where C is the self shielding correction factor and flux loss factor [3], K is the scaling factor for the number of neutrons in reactor zone, q is the reaction rate and $\phi(E)$ is the calculated neutron flux in the reactor. The K factor was determined from a reaction rates of ^{27}Al(n,α) and ^{58}Ni(n,p) reactions and represent the neutron flux. It was equal to 1.2078E+13 with the uncertainty 3.6% [85].

For reactor experiment it is necessary to know the self shielding correction factor. It is the relation between the SACS in the real geometry and SACS in the

same geometry, but with void cells. It can be calculated in MCNP. This problem is described in more detail in my Master thesis [3] in chapter 6.4.

Table 4.3: ^{64}Cu foil comparison with upside-down and upside-up measurement.

Energy [keV]		**Counts per second**	**Comparison [%]**
1173.2	upside-up	0.170226	0.336
1173.2	upside-down	0.169656	
1332.5	upside-up	0.156561	1.599
1332.5	upside-down	0.154097	

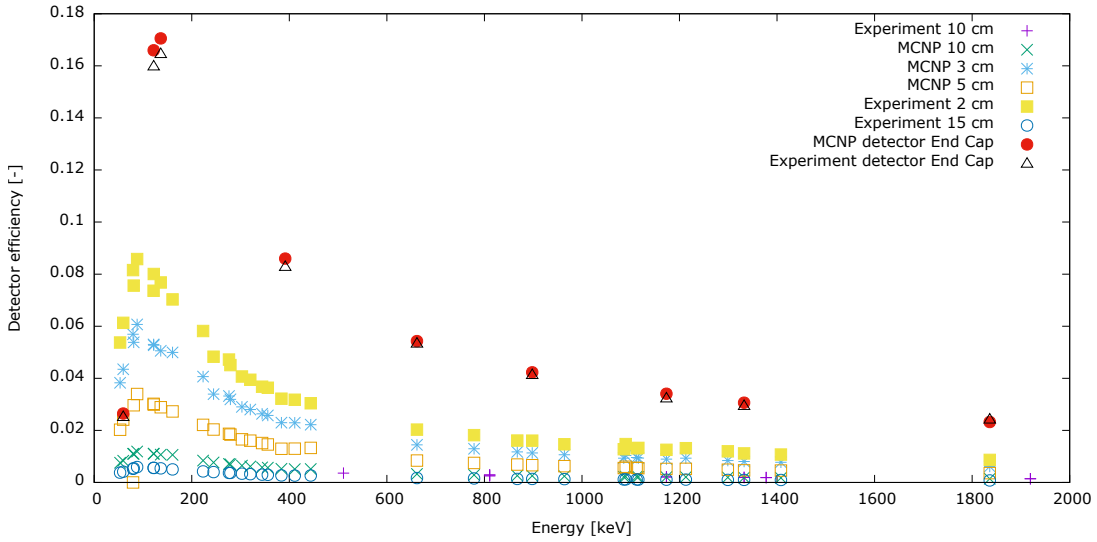

Figure 4.7: Detector efficiency - measured and calculated.

Results for spectral average cross-sections are summarized in Table 4.4. Obtained results confirm correctness of previous experiments in the zero power reactor LR-0. Those result thus confirm the hypothesis that even 5% of ^{238}U(n,f) does not have a significant influence on SACS uncertainties. The VR-1 reactor experiment had similar results as the LR-0 reactor experiment despite the difference in fuel enrichment (3.3wt% for LR-0 and 20wt% for VR-1), as can be seen in Table 4.5. In this table the measured results were also compared with IRDFF 1.05 nuclear data library. The uncertainties are based on statistic uncertainty(uncertainty of detector counts, more measurement of one foil and average value determination) and systematic uncertainty (uncertainty in source emission and uncertainty in reference Au and Ni monitors). More details about the determination of uncertainties are described in section 4.4.

Other measurements in reactor neutron spectrum are still ongoing. Not only in the VR-1 reactor spectrum, but also in the LVR-15 (the reactor parameters are mentioned in 3.1.3) reactor spectrum, which is more complicated. Due to the fuel burn-up effect, which can be neglected for example in the LR-0 and VR-1 reactors, it is necessary to also take into account the contribution of ^{239}Pu to the reactor spectrum due to its high operating powers. So, the neutron spectrum in this reactor is a linear combination of ^{235}U PFNS and ^{239}Pu PFNS. The ^{238}U PFNS could be neglected due to its 0.13% contribution. The fuel composition

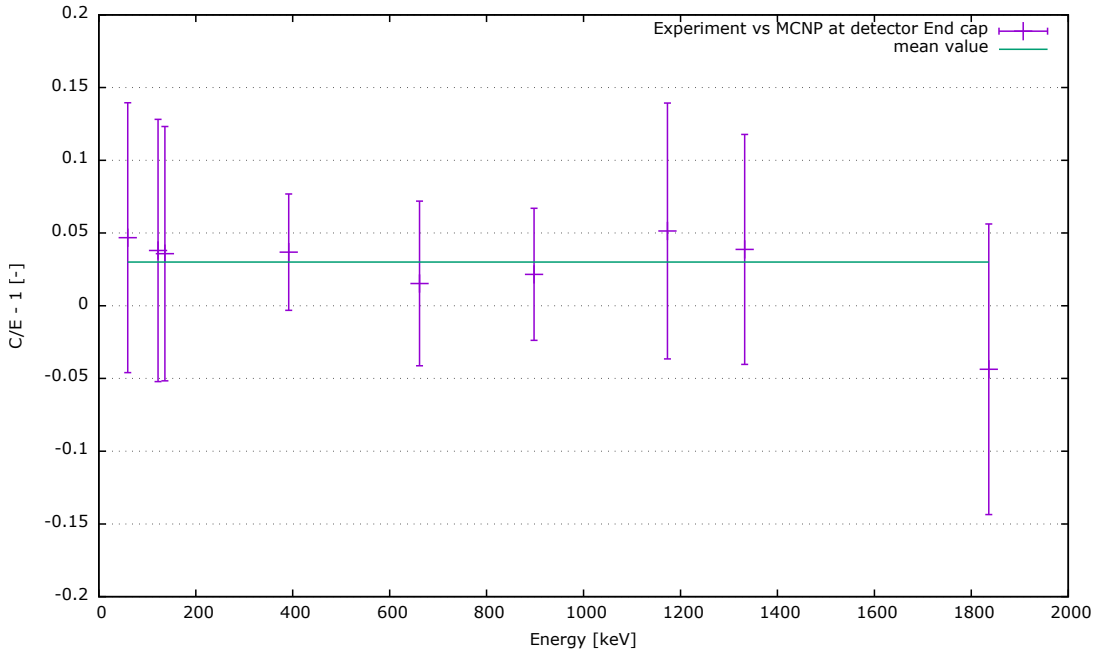

Figure 4.8: Calculated detector efficiency compared to measured detector efficiency at the detector end cap.

Table 4.4: SACS results for VR-1 reactor experiment. [43]

Reaction	**VR-1 SACS** [mb]	**uncertainty** [mb]
^{89}Y(n,2n)	0.1709	0.0115
^{46}Ti(n,p)	10.738	0.719
^{47}Ti(n,p)	17.896	1.181
^{48}Ti(n,p)	0.294	0.0199
^{54}Fe(n,p)	72.994	4.964
^{63}Cu(n,α)	0.528	0.036
^{93}Nb(n,2n)^{92}Nb*	0.444	0.029
^{58}Ni(n,x)^{57}Co	0.239	0.016

and its burn up effect is being calculated by the code NODER [86]. The burn up is calculated according to the irradiation history for each element of reactor core and according to the fission density. What this reactor core layout could look like can be seen in 3.5. More details about the ^{235}U SACS measurement in the field of the LVR-15 reactor can be found in [48].

4.2 Accelerator experiments

The experiments in the neutron spectrum of the accelerator neutron source were carried out to complement the ^{235}U SACS, used to validate nuclear data libraries, with a differential cross-section. The goal of adding these accelerator experiments was also to expand my awareness of both of these methods of measurement and validating nuclear data, which are essential for advanced nuclear systems. For this purpose I performed experiments with the group of researchers who are focused in this field. Their research included many reactions ([87], [88], [89], [90]). From my

Table 4.5: SACS results comparison in reactor spectrum of VR-1 and LR-0 with IRDFF nuclear data library. [43]

Reaction	**VR-1/IRDFF** [%]	**VR-1/LR-0** [%]
^{89}Y(n,2n)	1.12	1.73
^{46}Ti(n,p)	-6.71	-
^{47}Ti(n,p)	0.31	-
^{48}Ti(n,p)	-1.87	-3.29
^{54}Fe(n,p)	-8.38	-5.19
^{63}Cu(n,α)	7.36	-
^{93}Nb(n,2n)^{92}Nb*	-4.41	-

previously measured samples, they were besides focused on Y reactions, but I also added a measurement with Cu, which I measured in VR-1 reactor spectrum. The aim was to find out how these measurements can be connected and eventually suggest a measurement of other materials. As for reactor experiments, those using accelerator neutron sources, knowledge of their neutron spectrum is key. There are more options for how to determine it. ToF (time of flight) method, Monte Carlo (MC) calculation codes, by the target analysis or also by an activation detectors measurements. The best and the most precise approach is to use all methods and compare their results. As it was already mentioned above, from the accelerator measurement we are able to get a differential cross-section, but a pure mono-energetic neutron spectrum is not always produced. Usually it is a quasi-mono-energetic spectrum with a dominant peak and the lower energy continuum and the background, which needs to be subtracted.

4.2.1 Neutron spectrum by ToF

This method is based on measurement of the time, which a particle (in our case neutron) needs to cover a known distance between two points. The kinetic energy E_k is thus derived from the relativistic equation

$$E_k = m_0 c^2 \left(\frac{1}{\sqrt{1 - \frac{v^2}{c^2}}} - 1 \right), \tag{4.5}$$

where m_0 is the rest mass of particle, c is the speed of light and v is the particle velocity calculated by knowing the distance and time.

This method needs an accelerator which allows a pulse mode or the use of a chopper, which usually is a rotating disc with slots. During the particle interaction with the target there is also a significant amount of gamma photons produced. Those photons have a speed of light and thus arrive to the detector (scintillator detector) first. After the photons arrive at the detector they are gradually followed by neutrons, which are sorted from the fastest to the slowest. But this is the ideal case when all particles are created in one moment and it is assumed that before the start of a new pulse, all the particles from the previous pulse already arrived at the detector. This is not what occurs in reality. The fastest neutrons from the following pulse usually arrive to the detector earlier than the slowest neutrons from the previous pulse, so a corresponding correction

is needed. This phenomenon also sets a limit on the minimum detectable neutron energy. This neutron spectrum measurement requires an optimal choice of the distance between the neutron source and the detector (longer distance causes better energy resolution but on the other hand it causes an increase in minimum detectable neutron energy due to the frame overlap). The amplitude of the neutron pulses versus the determined time phase to the cyclotron radiofrequency signal for the 14.4 MeV proton irradiation is shown in the Figure 4.9 [91] [92]. The comparison of deconvoluted neutron spectrum for 14.4 MeV protons with the neutron spectrum obtained by ToF method is shown in the Figure 4.10 [91].

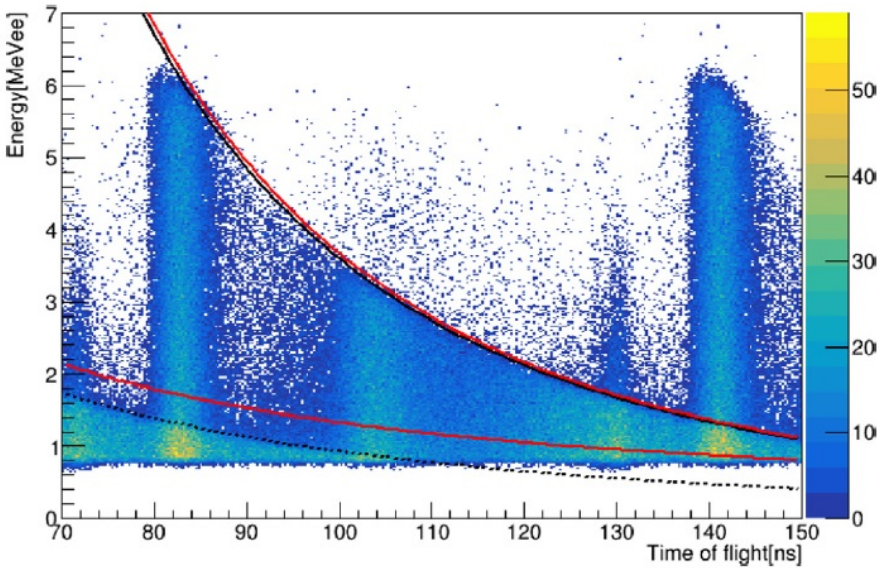

Figure 4.9: Amplitude of pulses versus their phase to the radiofrequency signal. [91]

4.2.2 Neutron spectrum by MC calculations

Neutron spectrum can also be obtained from MC models. The target station geometry and all its materials need to be defined in a calculation program such as MCNPX [37]. The proton beam from the accelerator is described as a Gaussian peak. For this method the cross-sections of fast protons with target materials are needed as well. Those data are used from data libraries. The accuracy of this method depends not only on the quality of model of the target station and the target itself, but also on the uncertainty of the data library and the choice of the library.

4.2.3 Neutron spectrum by target analysis

Another method how to obtain the neutron spectrum is to directly measure the target itself. Neutrons produced in the reaction ^{7}Li(p,n)^{7}Be significantly contribute to the mono-energetic peak in the neutron spectrum in case of ground state and first excited state of ^{7}Be ($^{7g+m1}$Be). The higher excited states contribute to the background continuum as well as other reactions such as ^{7}Li(p,np)^{6}Li. Thanks

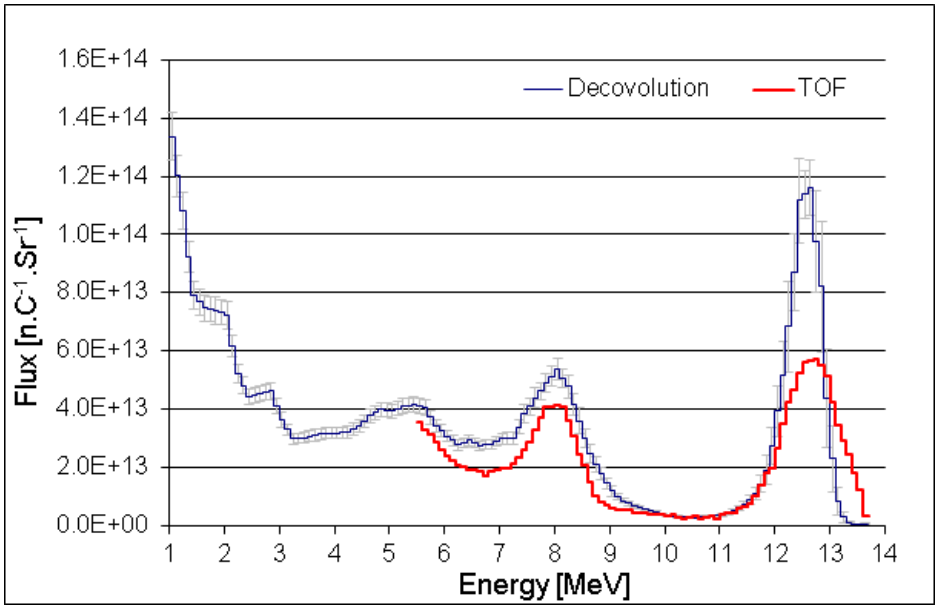

Figure 4.10: Comparison of the deconvoluted and TOF neutron spectrum for the 14.4 MeV protons. [91]

to this, when the Li target is measured after the irradiation, using HPGe detector, it is possible to get the $^{7g+m1}$Be reaction yield (4.1) and thus number of neutrons corresponding to the mono-energetic peak emitted into the entire space. Higher excited states of ^{7}Be always get deexcited by heavy particles, so then this can be distinguishable using a gamma spectrometry measurement. The only problem is the angular distribution. Neutron field of the Li target is strongly anisotropic which means the forward direction is preferred, but from target measurement we are able to obtain emission into entire space. Therefore it is necessary to determine the representation of the forward emitted neutrons. The ratio of forward emitted neutrons and neutrons emitted into the entire space can be described by the function

$$R = -5.155 \cdot 10^{-13} E_p^4 + 4.409 \cdot 10^{-9} E_p^3 + 2.483 \cdot 10^{-5} E_p^2 + 6.521 \cdot 10^{-2} E_p - 0.8636, \tag{4.6}$$

where E_p is the proton energy. This function was determined by Y. Uwamina [93] and is also applicable for the NG-2 target station in the Czech Republic. The usage of this same function has been verified several times [94] - the irradiated foils are placed in the forward direction maximum of angular distribution and their size is so small that this angular distribution can be neglected.

4.2.4 Neutron background

The neutron spectrum is not monoenergetic but quasi-monoenergetic. The nuclear reactions with low threshold energies might be strongly affected by the low energy continuum in the neutron spectrum. This continuum subtraction is based on the folding of the calculated cross-section and neutron spectrum [88]. The low energy neutron continuum correction is calculated as the ratio between the folding in the energy interval of the quasi-monoenergetic peak and in the whole

energy spectrum, as can be seen in the following equation [87]

$$C_{bgr} = \frac{\int_{peak} \sigma(E_n)N(E_n)dE_n}{\int_{spectrum} \sigma(E_n)N(E_n)dE_n} = \frac{\sum_{i \in peak} \sigma(i)N(i)}{\sum_{i \in spectrum} \sigma(i)N(i)}, \tag{4.7}$$

where $\sigma(E_n)$ is the reaction cross-section for energy E_n and $N(E_n)$ is the number of neutrons with E_n energy. The neutrons in the spectrum were divided into energetic groups and for each group cross-sections were calculated in the TALYS [13], which is the open source software and datasets for the simulation of nuclear reactions. This makes it possible to replace the integrals in equation 4.7 with a sum of the corresponding discrete values. However, as can be seen from the equation 4.7, for C_{bgr} determination, the knowledge of reaction cross-sections is needed, but its limited knowledge is why the reaction cross-section is measured. The cross-sections used in subtraction method was therefore predicted in the TALYS 1.96 code with default parameters.

4.2.5 Differential cross-section

The several experiments were performed during the research by my colleagues before I joined them. Some of them were previously published ([87], [88], [89], [90] and [95]). The last experiments, which have not been published yet, will be mentioned here in more detail.

Similarly as for reactor measurement, the activation detector method was used for differential cross-section determination. In this case equation 4.1 was also used. Differential cross-section was subsequently determined from the equation

$$\sigma = \frac{N_{yield} C_{bgr} S M_m}{N_n N_A m} = \frac{qSC_{bgr}}{N_n}, \tag{4.8}$$

where q is the reaction rate, S is the activation foil area, C_{bgr} is low energy neutron continuum correction and N_n is the number of neutrons in the neutron spectrum peak. In the case of accelerator neutron spectrum, it is necessary to control the flux unit. As can be seen for example in the Figure 4.14, the unit is $nC^{-1}Sr^{-1}$. This unit needs to be converted to $1/m^2$ using the spatial angle ($\frac{S_{foil}}{r^2}$, where r is the foil distance from Li target) and by accelerator beam charge (average accelerator beam current multiplied by irradiation time). The sum over the peak area gives us the value of N_n.

In the last experiments samples of Au, Y, Cu, Bi, Al, Co and NaF were irradiated. I focused on the analysis of the neutron reactions with Y and Cu samples, which I also measured in the reactor spectrum. The other samples were mainly analyzed by my colleague Jiří Járošík. ^{197}Au(n,γ) reaction was used as a standard for results validation. All samples were in the form of high purity thin foils with the size of 25×25 mm. In Table 4.6 the foils properties which were used as a follow-up to the previously measured samples in reactor spectrum are summarized. The designations 1 and 2 mean experiment 1 (E_n = 23.3 MeV) and experiment 2 (E_n = 14 MeV). The foils were placed in the specific order in a sample holder at a distance of 106 mm from Li target. The length of irradiation of the samples in both experiments can be seen in Figures 4.11 and 4.12. The neutron spectrum from both experiments can be see in Figures 4.13 and 4.14. As can be seen, the first experiment had a higher neutron energy, therefore the

cross-section of the ^{89}Y(n,3n)^{87}Y reaction was possible to measure. This reaction cross-section threshold can be seen in the Figure 4.17.

Table 4.6: Irradiated foils properties.

Foil material	**weight** [mg]	**thickness** [mm]
Au1	1498	0.8
Au2	1512.44	0.8
Y1	1413	1.1
Y2	1399.98	1.1
Cu1	1238	1.0
Cu2	1261.60	1.0

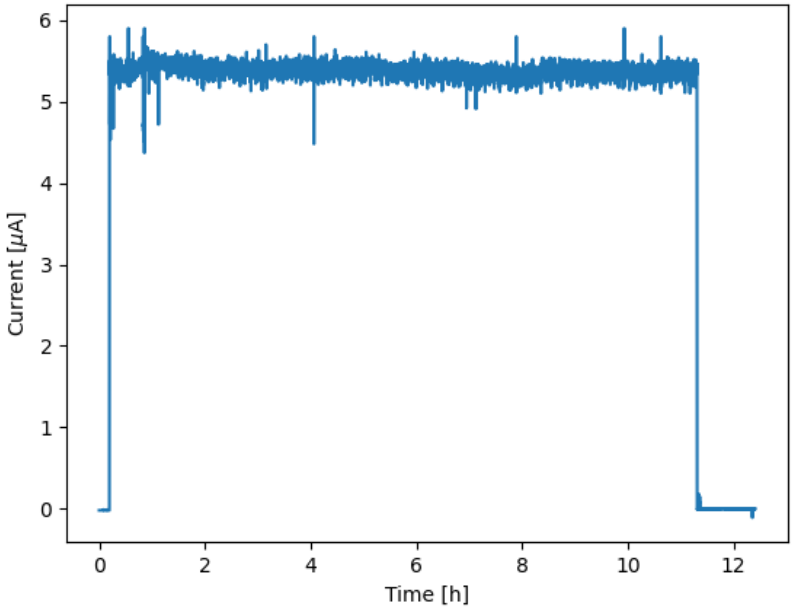

Figure 4.11: Accelerator current flow during the first experiment.

4.2.6 ^{63}Cu(n,α)^{60}Co and ^{63}Cu(n,2n)^{62}Cu cross-sections measurement

To follow up on the previous experiments in the VR-1 reactor spectrum, the reaction ^{63}Cu(n,α)^{60}Co was also measured. This reaction measurement was performed for the first time at the U-120M cyclotron and also due to the HPGe detector light contamination by ^{60}Co, the measurement faced some difficulties. Unlike the experiment in the reactor spectrum, a smaller sample of Cu was chosen, so there was no need to measure both sides of the sample. The main contribution of this experiment is experience and some recommendations for next measurements. In the Table 4.7 and 4.8 results for ^{63}Cu(n,α)^{60}Co reaction are summarized.

The measurement of ^{62}Cu is not easy, because the gamma line 511 keV is also produced by ^{64}Cu, which is created by gamma capture in ^{63}Cu or by the

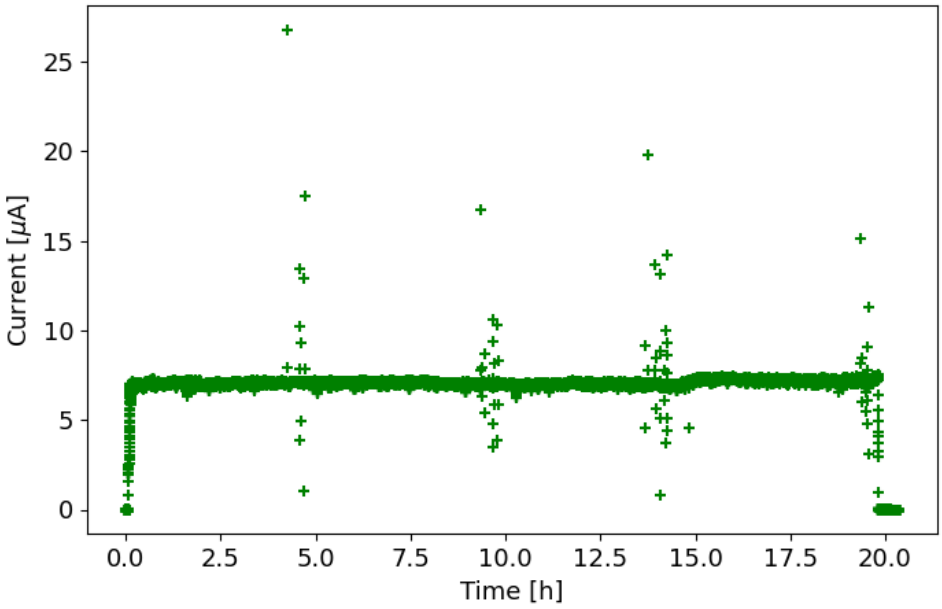

Figure 4.12: Accelerator current flow during the second experiment.

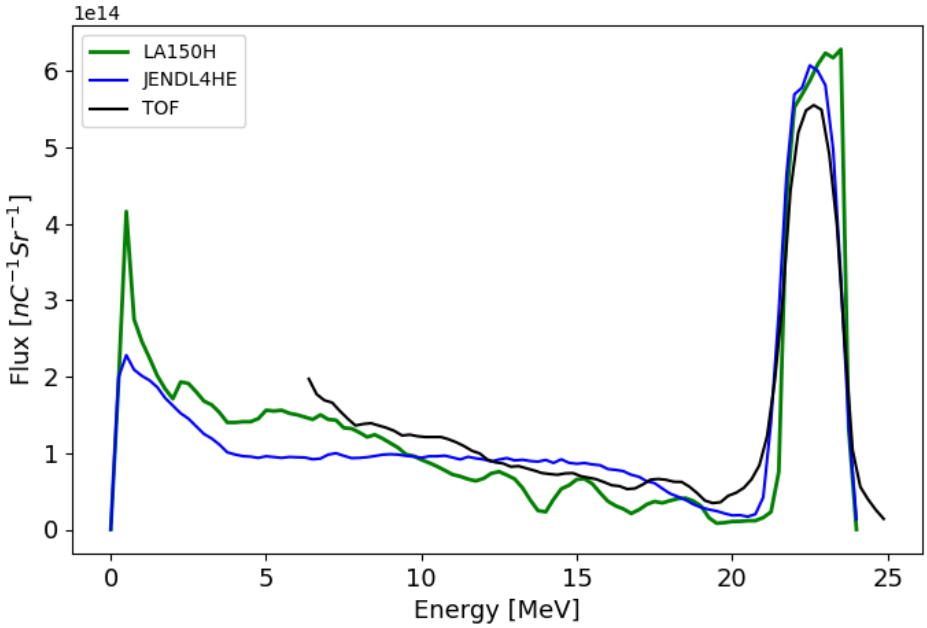

Figure 4.13: Neutrons spectrum during the first experiment, with neutron energy up to 25 MeV.

Table 4.7: The reaction rates results for ^{63}Cu(n,α)^{60}Co reaction.

Reaction	$q_{23.3\,MeV}$	**Δq** [%]	q_{14MeV}	**Δq** [%]
^{63}Cu(n,α)^{60}Co	$8.8399 \cdot 10^{-21}$	4.8	$4.69204 \cdot 10^{-24}$	4.7

reaction ^{65}Cu(n,2n)^{64}Cu. The abundance of ^{65}Cu in natural copper is 30.85 %.

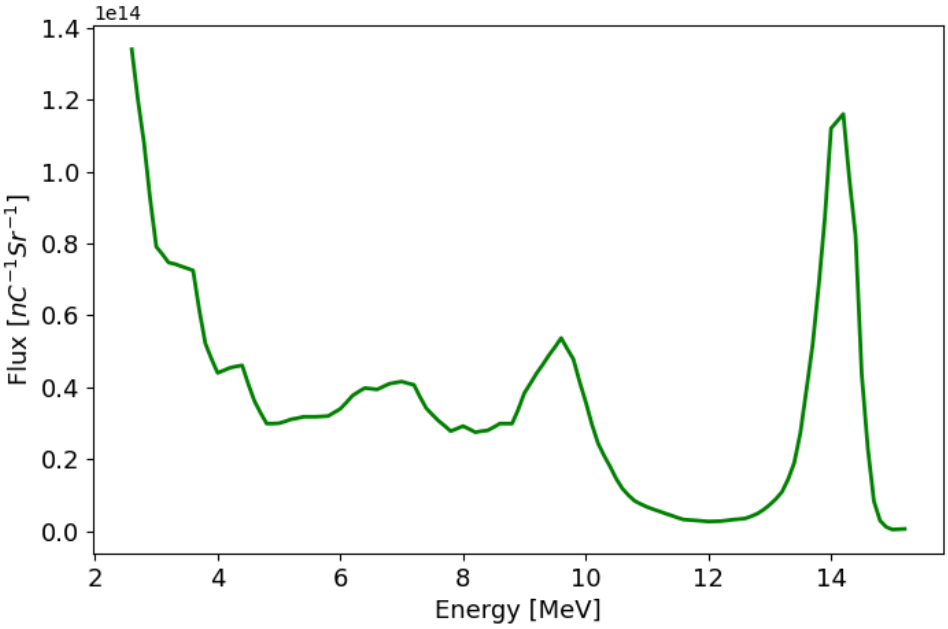

Figure 4.14: Neutrons spectrum during the second experiment, where the neutron peak is at 14 MeV.

Table 4.8: The cross-section results for ^{63}Cu(n,α)^{60}Co reaction.

Reaction	$\sigma_{23.3\,MeV}$[mb]	σ_{14MeV}[mb]	VR-1 SACS [mb]
^{63}Cu(n,α)^{60}Co	4.6	32	0.528

But the contribution to this annihilation peak can be distinguished due to the different half-lives of those Cu isotopes. ^{62}Cu has a half-life of 9.673 minutes, but ^{64}Cu has a half-life of 12.7 hours. This reaction threshold is above 11 MeV, as can be seen in the Figure 4.15, which, as can be seen in Figure 4.14, was fulfilled. During the irradiation of natural copper, three possible reactions can occur, namely ^{63}Cu(n,2n)^{62}Cu, ^{63}Cu(n,g)^{64}Cu and ^{65}Cu(n,2n)^{63}Cu. Due to the difference in half-life, the Cu foil was measured as soon as possible after the irradiation when the activity of ^{62}Cu is the highest and than the Cu foil was measured after a sufficiently long time (after 7 half-lives of ^{62}Cu) to measure ^{64}Cu activity. ^{64}Cu activity in the time of the first measurement can be calculated by decay law and subsequently, the ^{62}Cu activity can be calculated by subtraction of ^{64}Cu activity, NPA respectively. The calculation of ^{64}Cu NPA in the time of the first measurement after the irradiation is shown in the equation 4.9.

$$NPA_{64Cu} = \frac{NPA}{t_{life2}} \frac{e^{\lambda_{64Cu} t_{02}} \lambda_{64Cu} t_{real2}}{(1 - e^{-\lambda_{64Cu} t_{real2}})} \frac{t_{life1} e^{-\lambda_{64Cu} t_{01}} (1 - e^{-\lambda_{64Cu} t_{real1}})}{\lambda_{64Cu} t_{real1}}, \qquad (4.9)$$

where t_{life} is the life time of measurement by HPGe detector, t_{real} is the real time of measurement, t_0 is the time between the end of irradiation and the start of measurement, λ_{64Cu} is the decay constant of ^{64}Cu. The first two fractions express the NPA from the later measurement (measurement number 2) of ^{64}Cu (^{62}Cu is already decayed), corrected to the decay during the measurement and corrected

to the end of the irradiation time. The last parts of this equation express the recalculation of ^{64}Cu NPA from the second measurement to the NPA of ^{64}Cu in the time of the first measurement (measurement number 1, where NPA of 511 keV is the sum of ^{64}Cu and ^{62}Cu). [64]

The NPA of ^{62}Cu is then calculated as:

$$NPA_{62Cu} = NPA_{total} - NPA_{64Cu}. \tag{4.10}$$

Subsequently the activity of ^{62}Cu can be calculated using the equation 4.11.

$$A_{62Cu} = \frac{NPA_{62Cu}\lambda_{62Cu}t_{real}}{t_{life}\eta\epsilon_{62Cu}} \frac{e^{\lambda_{62Cu}t_0}}{(1 - e^{-\lambda_{62Cu}t_{real}})}. \tag{4.11}$$

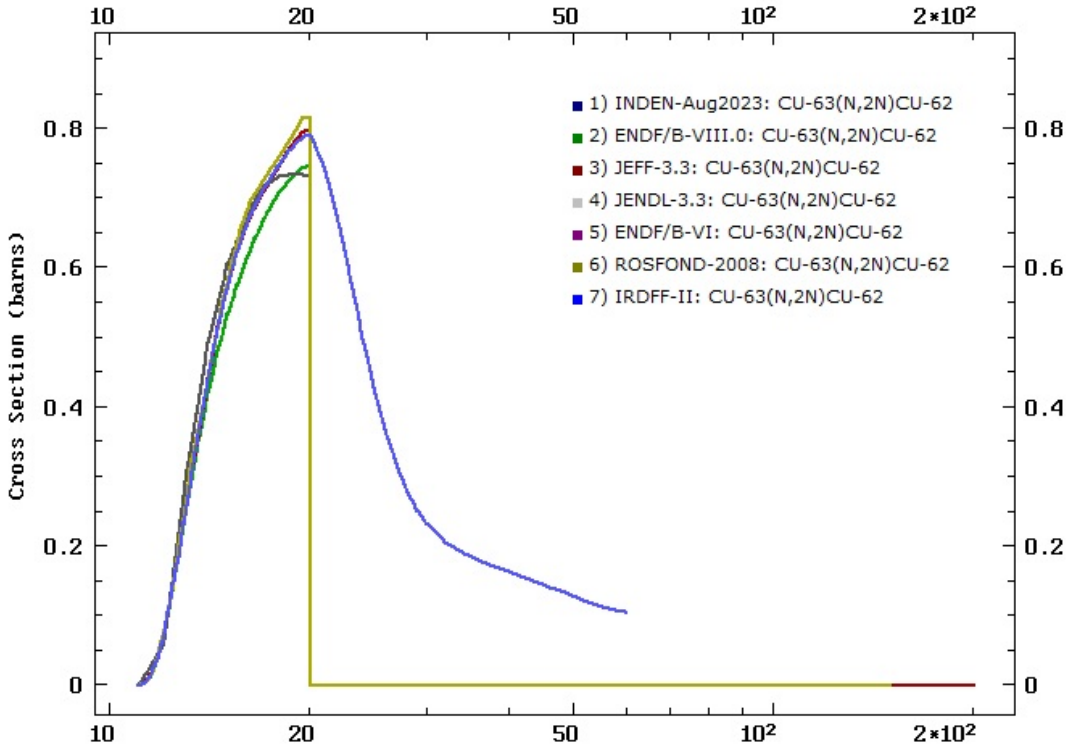

Figure 4.15: Cross-section for ^{63}Cu(n,2n)^{62}Cu reaction. [15]

The result of ^{62}Cu decay curve evaluated using annihilation peak can be seen in Figure 4.16. From this decay curve, the ^{62}Cu half life was experimentally determined by fitting experimental data with exponential function as 7.9 minutes (the table value is 9.67 minutes). From the fit, one parameter is decay constant λ and using the conversion over $ln2$ we get the half life. This experimental half life difference from the table value is within the uncertainties. Reaction rates and cross-sections are in Table 4.9. In the second experiment the uncertainty is higher due to the lower number of activation foils measurements.

4.2.7 ^{89}Y(n,2n)$^{88g+m}$Y and ^{89}Y(n,3n)$^{87g+m}$Y reactions

As a follow-up to the previously measured spectral averaged cross-sections in the VR-1 reactor spectrum for ^{89}Y(n,2n)$^{88g+m}$Y, this experiment was also performed

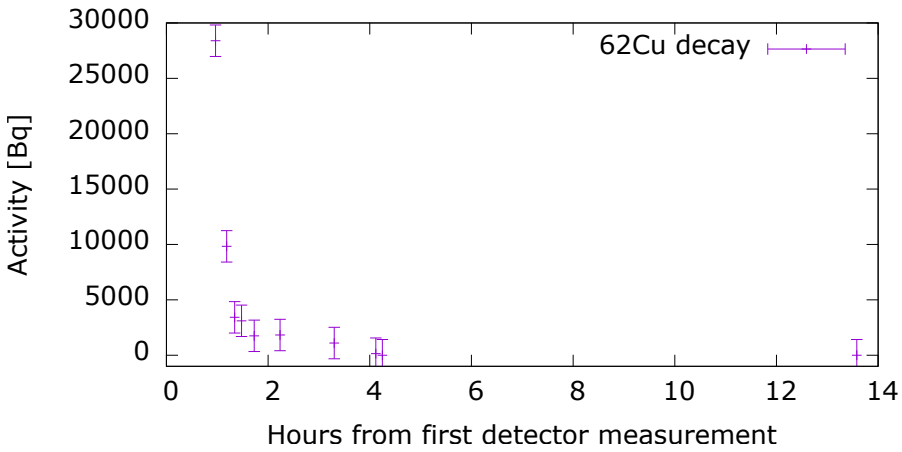

Figure 4.16: Decay curve of ^{62}Cu.

Table 4.9: Measured results for ^{63}Cu(n,2n)^{62}Cu reaction with statistical and systematic uncertainty.

Experiment	**q**	**Δq** [%]	σ[b]	$\Delta\sigma$[b]
Cu 1 (23.3 MeV)	$5.67 \cdot 10^{-15}$	4.8	0.543	0.072
Cu 2 (14 MeV)	$1.02 \cdot 10^{-17}$	5.2	0.309	0.044

in the accelerator neutron spectrum. As the accelerator neutrons energy is higher in comparison to the reactor neutrons, in this experiment it was also possible to measure ^{89}Y(n,3n)$^{87g+m}$Y reaction, where it is possible to distinguish the ground (g) and metastable (m) states by a gamma peak measurement.

If the monitored nuclide is in the decay series of another radionuclide, which is also produced during the reaction, the equation for calculation of the reaction rate 4.3 is violated. In this case due to the high purity of irradiated samples the equation is violated only in the case of the production of a radionuclide in both the ground and metastable states. The metastable nuclei are deexcited to the ground state nuclei and thus contribute to its activity. If the half-life of this metastable state is long enough, it can be measured. In the case of those experiments, it occurs in reactions ^{89}Y(n,2n)$^{88g+m}$Y, ^{89}Y(n,3n)$^{87g+m}$Y, ^{197}Au(n,2n)$^{196g+m1}$Au and ^{197}Au(n,2n)^{196m2}Au.

Cross-sections of ^{88g}Y and ^{88m}Y are not possible to distinguish due to the short half-life of ^{88m}Y, which is only 14 ms. But ^{87m}Y has a half-life of 13.37 h, so it can be measured separately. For the reaction ^{89}Y(n,2n) the reaction rate was determined by measurement of gamma peaks of ^{88}Y, 898 keV and 1836.1 keV. These results can be seen in the Table 4.10 for the reaction rate and in the Table 4.11 for the cross-section. This reaction was measured during both previously mentioned experiments and both experiments are summarized in the table as well as a comparison of the result for each energy peak separately.

In the case of distinguishing the reaction rates of ^{87g}Y and ^{87m}Y states the method of measurement gamma lines of ^{87m}Y and ^{87g}Y (380.79 keV for m state, 484.8 keV and 388.5 keV for g state) can be used. The same method can be used for Au (for g state 355.73 keV and 333 keV, for m state 147.8 keV and 188.27 keV).

In Table 4.12 the results for numbers of nuclei at the end of irradiation, reaction rates and cross-sections, can be seen. Au sample was used as a monitor.

Table 4.10: Reaction rate result for ^{89}Y(n,2n)$^{88g+m}$Y reaction with statistical and systematic uncertainty.

Experiment	$q_{898\,keV}$	Δ[%]	$q_{1836\,keV}$	Δ[%]	$\bar{q}$	$\Delta\bar{q}$[%]
1 (23.3 MeV)	$4.54 \cdot 10^{-16}$	1.40	$4.62 \cdot 10^{-16}$	1.43	$4.58 \cdot 10^{-16}$	1.0
2 (14 MeV)	$5.10 \cdot 10^{-17}$	0.96	$5.13 \cdot 10^{-17}$	0.98	$5.12 \cdot 10^{-17}$	0.69

Table 4.11: Cross-section result for ^{89}Y(n,2n)$^{88g+m}$Y reaction.

Experiment	$\sigma_{898\,keV}$ [b]	Δ[b]	$\sigma_{1836\,keV}$ [b]	Δ[b]	$\bar{\sigma}$ [b]	$\Delta\bar{\sigma}$[b]
1 (23.3 MeV)	1.014	0.093	1.032	0.096	1.023	0.086
2 (14 MeV)	0.739	0.068	0.744	0.069	0.741	0.064

In Figure 4.18 experimentally measured ^{87}Y decay curves can be seen. The result of the measurement of ^{196}Au in the units of activity can be seen in Figure 4.19. In both cases, the g and m states decay curves were fitted by Python programming using the following function with guessed initial parameters:

$$f(x) = e^{(-a \cdot x)} \cdot [b \cdot (e^{(-c \cdot x)} - 1) + d], \tag{4.12}$$

where a, b, c and d are the fitted parameters. Parameters a and c represent the decay constants of the ground state and metastable state, parameter b represents $N_{0,m}$ respectively $A_{0,m}$ and parameter d represents $N_{0,g}$ respectively $A_{0,g}$.

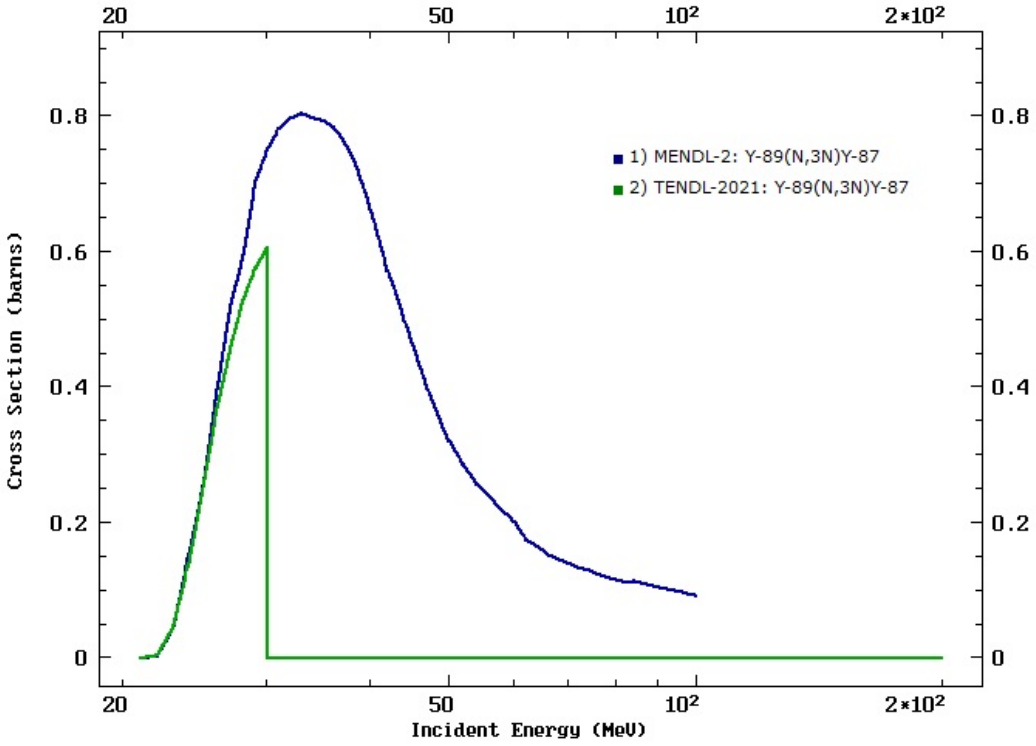

Figure 4.17: Cross-section for ^{89}Y(n,3n)^{87}Y reaction. [15]

Table 4.12: Number of nuclei at the end of irradiation for Y and Au.

Results	^{87}**Y (23.3 MeV)**	^{196}**Au (23.3 MeV)**
$N_{0,m}$	$1.737 \cdot 10^{8}$	$1.33 \cdot 10^{8}$
$N_{0,g}$	$1.347 \cdot 10^{8}$	$3.89 \cdot 10^{9}$
q_m	$2.77 \cdot 10^{-18}$	$4.82 \cdot 10^{-17}$
q_g	$3.58 \cdot 10^{-18}$	$4.63 \cdot 10^{-17}$
σ_m [b]	0.124	0.0971
σ_g [b]	0.0264	0.0787

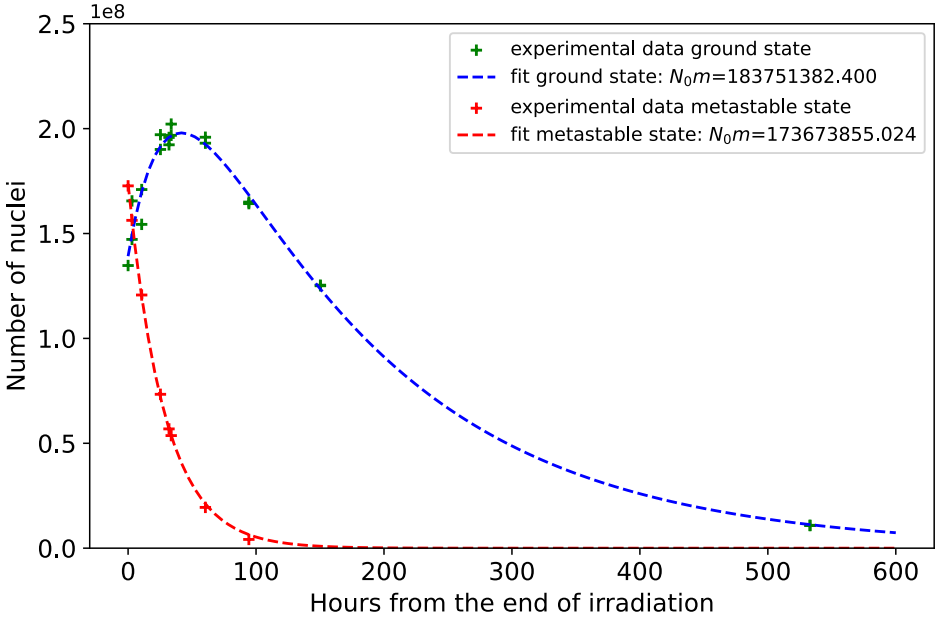

Figure 4.18: ^{87g}Y and ^{87m}Y experimentally determined decay curves from gamma peak measurements.

4.3 Results summary and discussion

This work summarizes the results of previous research and at the same time provides new data of cross-sections, which were measured both in the reactor spectrum and in the spectrum of accelerator-generated neutron spectrum and are summarized in Table 4.13.

The cross-section values in Tables 4.14, 4.15, 4.16, 4.17, 4.18, 4.19 and 4.20 are compared with selected libraries of nuclear data. In tables for differential cross-sections, some previously measured cross-sections with the same or similar neutron energy, are also mentioned. As can be seen, those data are also really old and need to be not only updated, but also new data needs to be added to clarify and validate those data. For some data from libraries cross-sections uncertainties were found in JANIS covariance database [96]. Measured differential cross-sections were also compared with the TALYS cross-sections calculations, EXFOR experimental data results and nuclear data libraries in Figures 4.20, 4.21, 4.22, 4.23, 4.24 and 4.25.

As can be seen from the result figures, new experimental data was obtained

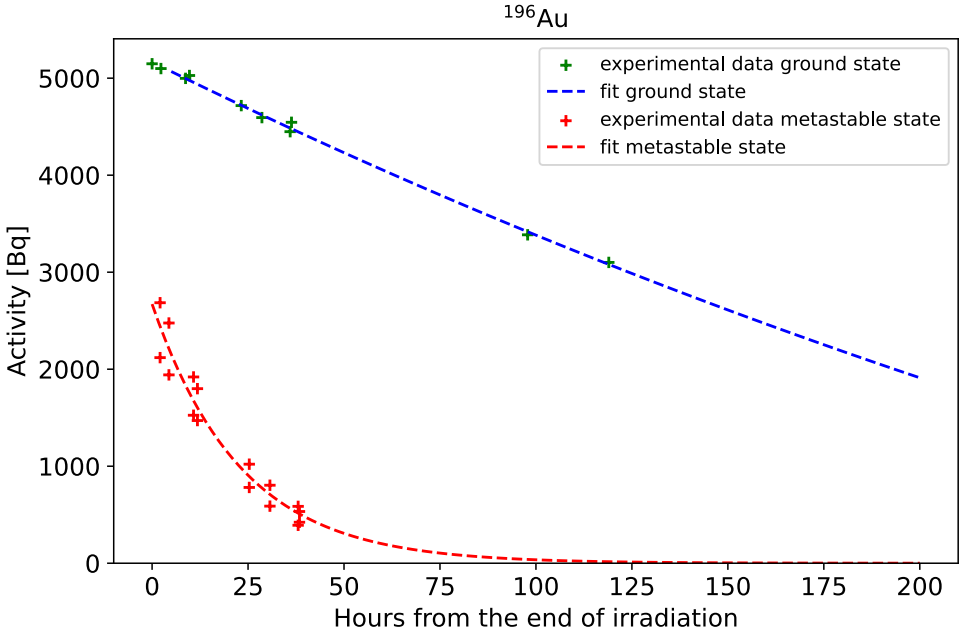

Figure 4.19: ^{196g}Au and ^{196m}Au experimentally determined decay curves from gamma peak measurements.

especially for ^{63}Cu(n,a) and ^{89}Y(n,3n) reactions. For Cu reactions can also be seen that measured cross-sections does not match the values in the nuclear data libraries. It shows that more experiments are needed. In the case of ^{89}Y(n,3n) reaction we can see a lack of data, so my experimental data well complements the existing data and are with a good agreement with nuclear data library Tendl 2021. The metastable state ^{87m}Y is harder to determined and thus the measured value is not in such a good agreement with data library as the ^{87g}Y. All measured cross-sections are in a good agreement with other experimentally determined cross-sections from EXFOR. In the case of ^{89}Y(n,2n) reaction differential cross-section, we can see from Figure 4.23 that the results are with a good agreement with previously measured cross-sections and also with the nuclear data libraries. It confirms that we have well described excitation function for this reaction and thus various libraries and experimental data differs minimally.

This also applies to the case of ^{89}Y(n,2n) SACS measured in VR-1 reactor neutron spectrum, as can be seen from the Table 4.5, the difference in result for IRDFF nuclear data library is only 1.12%. The bests agreement with IRDFF nuclear data library has the SACS of ^{47}Ti(n,p) which is only 0.31%. Measured data were also compared in the same table with previously measured SACS in the neutron field of LR-0 reactor to confirm the hypothesis that even 5% of ^{238}U(n,f) does not have a significant influence on SACS uncertainties. This conclusion is the main new knowledge obtained from this VR-1 experiment.

As can also be seen in the tables with the reactor neutron spectrum results (4.15 and 4.17), the reaction rates for mentioned data libraries was calculated. It was calculated by the scalar product of the VR-1 neutron spectrum with the data library cross-section in the same group structure and unit, which was obtained in JANIS [96].

To summarize it as a whole, it can be seen that during this work and research, some new data and some data which can help to validate the existing data, were measured. The goal was also to measure the same samples in the reactor spectrum as well as in the accelerator neutron spectrum, so the result is not only SACS but also some differential cross-sections. Both methods are similar and using same concept of gamma spectrometry measurement and activation method, but the spectrum itself is different and need to be evaluated by different methods, as was described in this thesis. Based on these results I can recommend some future measurements. In the field of differential cross-sections, I can recommend to measure more experiments with Cu samples and also to measure the ^{89}Y(n,3n)^{87g}Y cross-section since there is lack of experimental data. In the field of SACS measurement, I can recommend to measure more cross-sections in LVR-15 experimental reactor. This reactor neutron spectrum is much harder to validate due to the fuel burn up and there is not much experience with those cross-sections measurements.

Table 4.13: Measured cross-sections results summary.

Reaction	$\sigma_{23.3MeV}$[b]	$\Delta\sigma$[b]	σ_{14MeV}[b]	$\Delta\sigma$[b]	SACS[mb]	$\Delta\sigma$[mb]
^{46}Ti(n,p)	-	-	-	-	10.738	0.72
^{47}Ti(n,p)	-	-	-	-	17.896	1.18
^{48}Ti(n,p)	-	-	-	-	0.294	0.02
^{54}Fe(n,p)	-	-	-	-	72.994	4.96
^{63}Cu(n,2n)	0.543	0.072	0.309	0.044	0.1763 [64]	0.0076
^{63}Cu(n,α)	0.0046	0.0021	0.032	0.005	0.53	0.04
^{89}Y(n,2n)	1.023	0.086	0.741	0.064	0.171	0.012
^{89}Y(n,3n)^{87g}Y	0.0264	0.0035	-	-	-	-
^{89}Y(n,3n)^{87m}Y	0.1239	0.0177	-	-	-	-
^{197}Au(n,2n)$^{196g+m}$Au	0.2875	0.082	1.85	0.15	-	-

Table 4.14: Comparison of results in accelerator driven neutron spectrum for ^{63}Cu(n,2n) reaction.

^{63}Cu(n,2n)	σ[b]	$\Delta\sigma$[b]
experiment $E_n = 23.3$ MeV	0.543	0.072
experiment $E_n = 14$ MeV	0.309	0.044
IRDFF-II $E_n = 23.3$ MeV	0.4216	0.0579
IRDFF-II $E_n = 14$ MeV	0.4389	0.0057
JEFF-3.3 $E_n = 23.3$ MeV	-	-
JEFF-3.3 $E_n = 14$ MeV	0.437	0.028
ENDF/B-VIII.0 $E_n = 23.3$ MeV	-	-
ENDF/B-VIII.0 $E_n = 14$ MeV	0.417	-
CENDL - 3.2 $E_n = 23.3$ MeV	0.422	-
CENDL - 3.2 $E_n = 14$ MeV	0.447	-
Y.Uwamino (1992) $E_n = 25.5$ MeV	0.403 [97]	0.12
Y.Ikeda (1994) $E_n = 14$ MeV	0.42 [98]	0.01

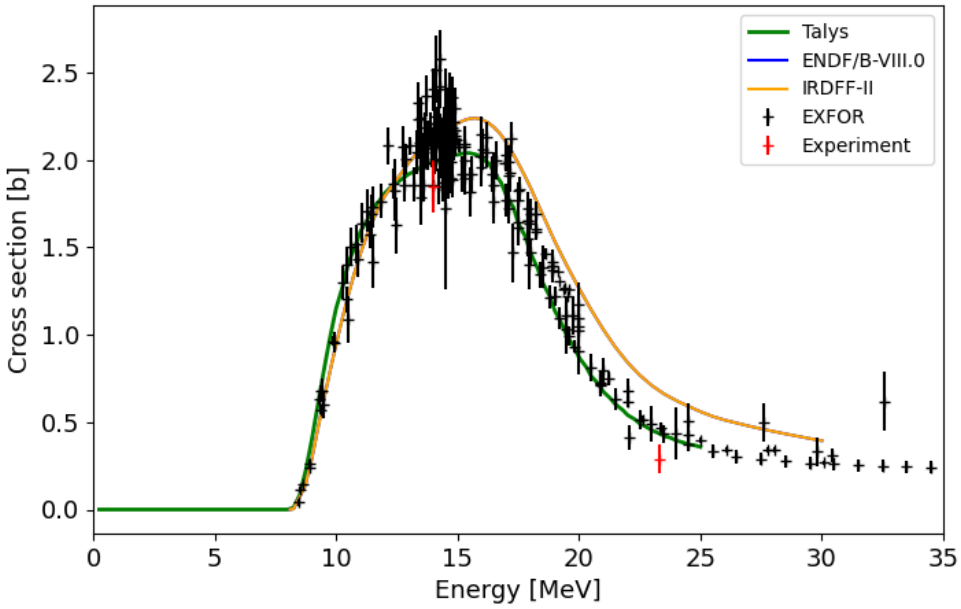

Figure 4.20: ^{197}Au(n,2n)$^{196g+m}$Au reaction cross-section measured result with comparison to other EXFOR data, TALYS calculation and ENDF/B-VIII.0 nuclear data library. [7] [15]

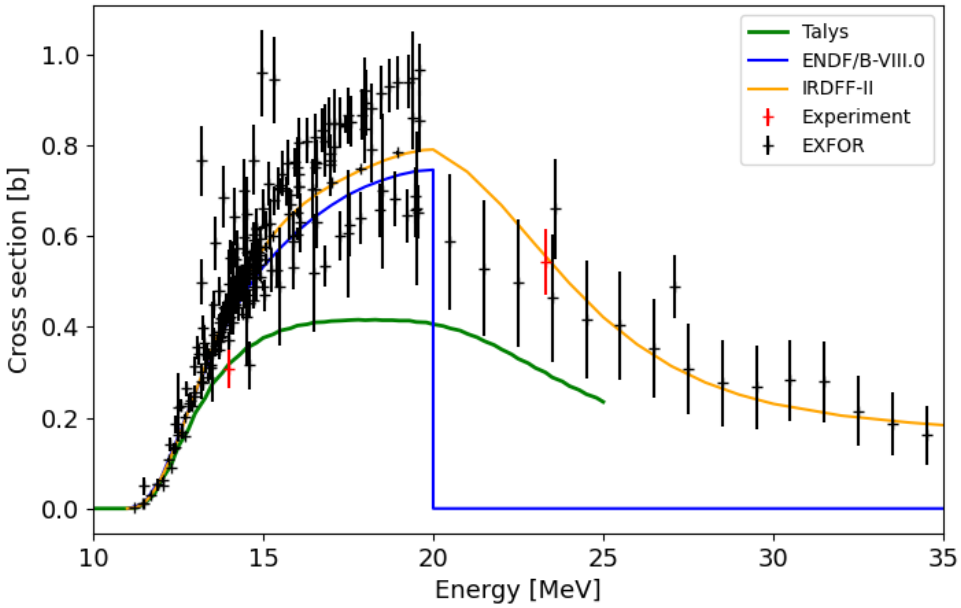

Figure 4.21: ^{63}Cu(n,2n)^{62}Cu reaction cross-section measured result with comparison to other EXFOR data, TALYS calculation and two nuclear data libraries. [7] [15] [99]

Table 4.15: Comparison of VR-1 experiment results with nuclear data libraries for ^{63}Cu(n,α) reaction (q unit is neutron per atom).

^{63}Cu(n,α)	q	SACS[mb]
VR-1 experiment	3.46E-32	0.528 ± 0.036
IRDFF II	3.42E-32	0.4918 ± 0.024
CIELO g6	-	0.5157 ± 0.071
JEFF 3.3	3.31E-32	-
JENDL 4.0	3.55E-32	-
ENDF/B-VIII.0	4.44E-32	-
CENDL 3.2	3.20E-32	-
ROSFONF 2010	3.34E-32	-

Table 4.16: Comparison of results in accelerator driven neutron spectrum for ^{63}Cu(n,α) reaction.

^{63}Cu(n,α)	σ[b]	$\Delta\sigma$[b]
experiment $E_n = 23.3$ MeV	0.0046	0.002
experiment $E_n = 14$ MeV	0.032	0.005
IRDFF II $E_n = 23.3$ MeV	0.006	-
IRDFF II $E_n = 14$ MeV	0.046	-
JEFF 3.3 $E_n = 23.3$ MeV	-	-
JEFF 3.3 $E_n = 14$ MeV	0.045	-
JENDL-5 $E_n = 23.3$ MeV	-	-
JENDL-5 $E_n = 14$ MeV	0.043	-
ENDF/B-VIII.0 $E_n = 23.3$ MeV	-	-
ENDF/B-VIII.0 $E_n = 14$ MeV	0.044	-
CENDL 3.2 $E_n = 23.3$ MeV	0.006	-
CENDL 3.2 $E_n = 14$ MeV	0.045	-
TENDL 2021 $E_n = 23.3$ MeV	0.003	-
TENDL 2021 $E_n = 14$ MeV	0.025	-
B. Czapp (1960) $E_n = 14$ MeV	0.047 [7]	0.0094

Table 4.17: Comparison of VR-1 experiment results with nuclear data libraries for ^{89}Y(n,2n) reaction (q unit is neutron per atom).

^{89}Y(n,2n)	q	σ[mb]
VR-1 experiment	1.12E-32	0.1709 ± 0.012
IRDFF II	1.04E-32	0.169 ± 0.008
CIELO g6	-	0.1645 ± 0.093
JEFF 3.3	1.05E-32	-
JENDL 4.0	1.02E-32	-
ENDF/B-VIII.0	1.05E-32	-
CENDL 3.2	1.08E-32	-
ROSFONF 2010	1.05E-32	-

4.4 Uncertainties of obtained results

It is still important to discuss also the uncertainties of the final results and how they were obtained. The statistical and systematical uncertainties will be described in this section in more details. All uncertainties are applicable for the

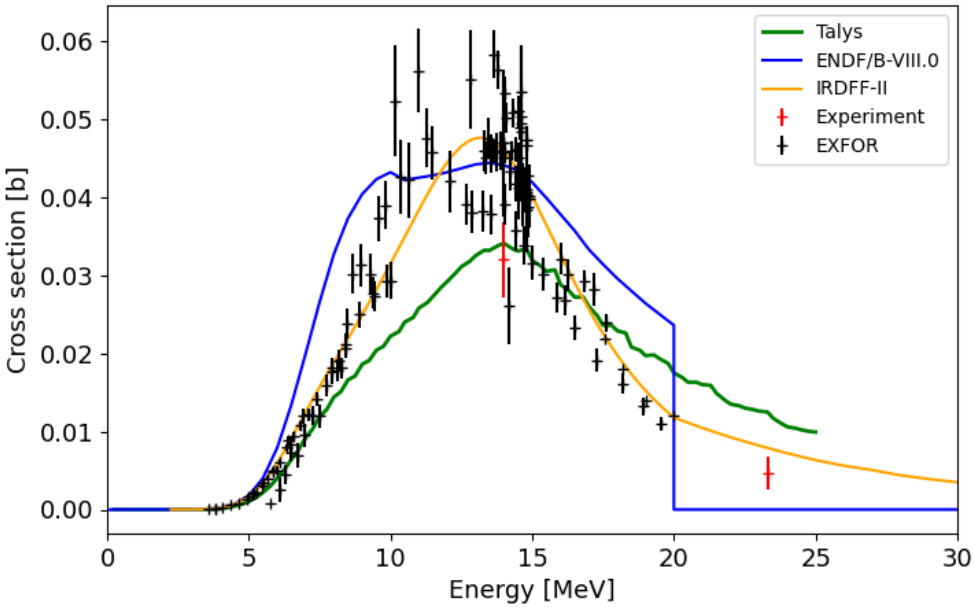

Figure 4.22: ^{63}Cu(n,a)^{60}Co reaction cross-section measured result with comparison to other EXFOR data, TALYS calculation and two nuclear data libraries. [7] [15] [99]

Table 4.18: Comparison of results in accelerator driven neutron spectrum for ^{89}Y(n,2n) reaction.

^{89}**Y(n,2n)**	σ[b]	$\Delta\sigma$[b]
experiment $E_n = 23.3$ MeV	1.023	0.086
experiment $E_n = 14$ MeV	0.741	0.064
IRDFF II $E_n = 24.5$ MeV	0.991	0.041
IRDFF II $E_n = 14$ MeV	0.858	0.0098
JEFF 3.3 $E_n = 23.3$ MeV	-	-
JEFF 3.3 $E_n = 14$ MeV	0.824	0.016
ENDF/B-VIII.0 $E_n = 23.3$ MeV	-	-
ENDF/B-VIII.0 $E_n = 14$ MeV	0.824	0.016
CENDL 3.2 $E_n = 23.3$ MeV	0.909	-
CENDL 3.2 $E_n = 14$ MeV	0.850	0.073
N.I.Molla (1998)$E_n = 14$ MeV	0.802 [7]	0.08
M.Kostal (2023) $E_n = 14.05$ MeV	0.795 [7]	0.0318
Y.Uno (1996) $E_n = 24.99$ MeV	0.9739 [7]	0.0395

Table 4.19: Comparison of results in accelerator driven neutron spectrum for ^{89}Y(n,3n)^{87g}Y reaction.

^{89}**Y(n,3n)**^{87g}**Y**	σ[b]	$\Delta\sigma$[%]
Experiment	0.0264	0.004
Tendl 2021 $E_n = 23$ MeV	0.0187	-
Tendl 2021 $E_n = 24$ MeV	0.0458	-
P. Chudoba (2018) 24.5 MeV	0.043 [7]	0.005

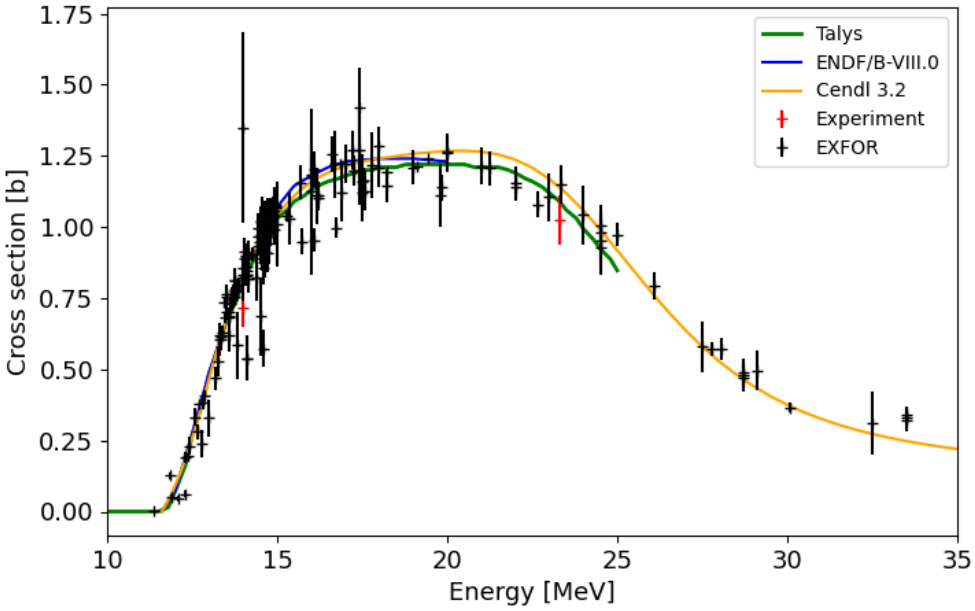

Figure 4.23: ^{89}Y(n,2n)^{88}Y reaction cross-section measured result with comparison to other EXFOR data, TALYS calculation and two nuclear data libraries. [7] [15] [99]

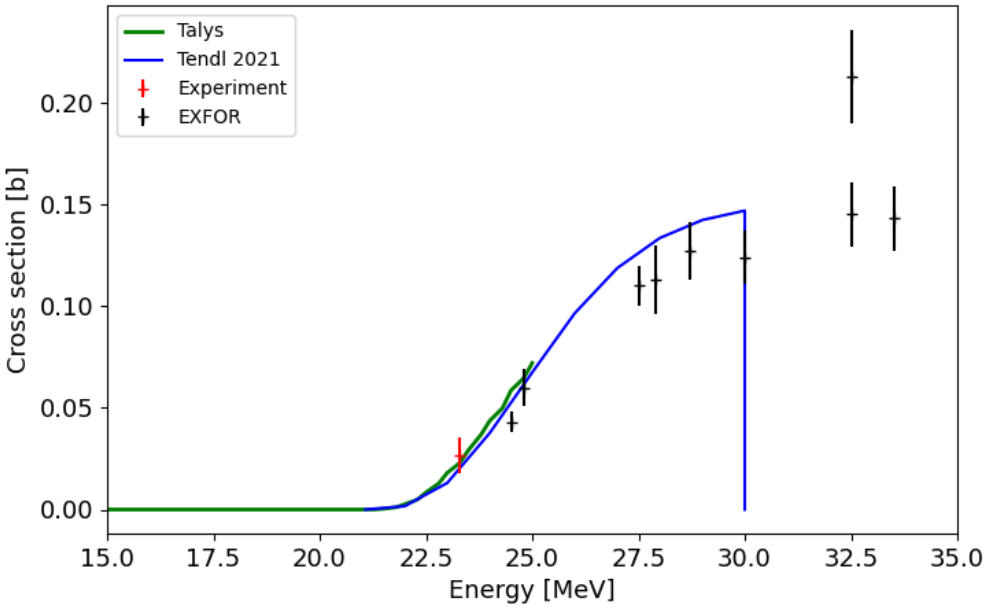

Figure 4.24: ^{89}Y(n,3n)^{87g}Y reaction cross-section measured result with comparison to other EXFOR data, TALYS calculation and Tendl 2021 nuclear data library. [7] [12]

both type of measurements in the reactor neutron spectrum and accelerator neutron spectrum. As can be seen for example in the equation 4.8, the cross-section uncertainty is composed of the uncertainties of all quantities involved. The main

Table 4.20: Comparison of results in accelerator driven neutron spectrum for ^{89}Y(n,3n)^{87m}Y reaction.

^{89}**Y(n,3n)**^{87m}**Y**	σ[b]	$\Delta\sigma$[b]
Experiment	0.124	0.02
Tendl 2021 $E_n = 23$ MeV	0.0472	-
Tendl 2021 $E_n = 24$ MeV	0.1229	-
P. Chudoba (2018) 24.5 MeV	0.11 [7]	0.012

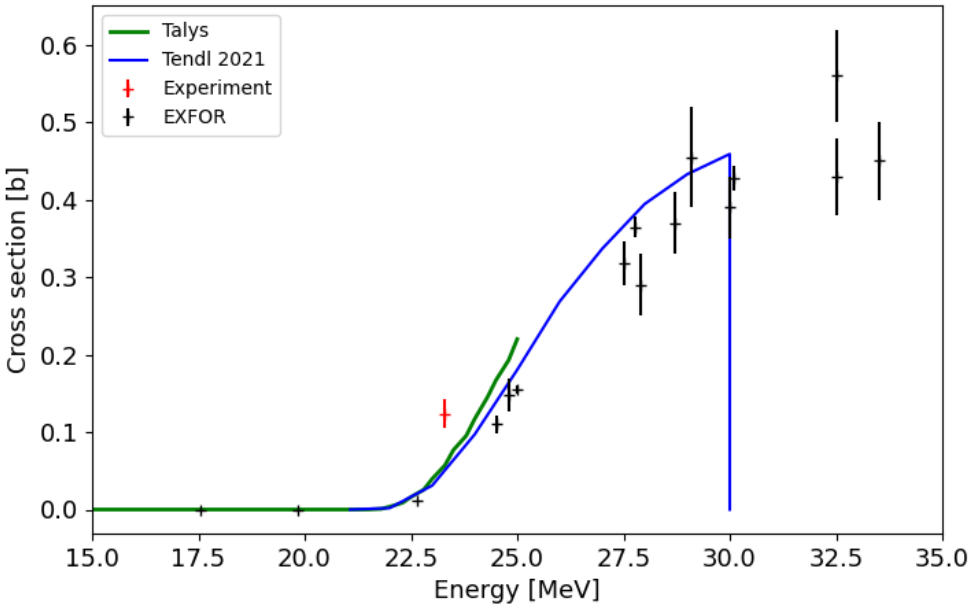

Figure 4.25: ^{89}Y(n,3n)^{87m}Y reaction cross-section measured result with comparison to other EXFOR data, TALYS calculation and Tendl 2021 nuclear data library. [7] [12]

part of the result uncertainty is the neutron spectrum determination since the neutron spectrum is used in cross-section calculation (in reactor experiments) and also in background subtraction (accelerator experiments).

4.4.1 Systematical uncertainties

All uncertainties such are the irradiation uncertainties, gamma spectrometry uncertainties and the neutron energy and neutron spectrum determination uncertainty are systematical. The major contribution of the samples irradiation uncertainty originates from foil positioning in the irradiation position (2%), current measurement (5%), the energy and the number of protons determination (1.5%) and also the accelerator target thickness (2%) or the foil distance from the target uncertainty (2%). The beam instability correction is within our precision negligible. The difference in neutron flux density between the first and the last irradiated sample can be up to 20%. Therefore, it is necessary to record the exact position of each sample. We also have uncertainties of weight of the samples or time measurement precision but they are often negligible. In these uncertainties

the C_{bgr} uncertainty (1%-15%) is included as well [90] [91] [92].

Other uncertainties are the uncertainty of the neutron spectrum spectrometry [91] and the HPGe spectrometry uncertainty during the detector measurement of the irradiated foils. Those spectrometry uncertainties are the NPA uncertainty, which is less than 1%, but in case of the annihilation peak where due to Doppler broadening, the peak has a bigger FWHM, the uncertainty is higher. The included spectrometry uncertainty is also the detector efficiency uncertainty. This value is calculated from the MCNP model and it is usually around 2%. In this case, uncertainties of the measured foil characteristics, such as their size (0.1%) and mass (0.01%) or also a molar mass, play a role as well. Those uncertainties are practically negligible compared to the other previously mentioned uncertainties. The uncertainty of true coincidence summing (2.5%) also has to be included.

Finally for the correct determination of the final cross-sections results it is necessary to precisely know the neutron energy (the case of accelerator measurements) and the neutron spectrum (the case of reactor measurements), which caused these reactions.

In the case of accelerator measurements, as can be seen in Figure 4.14, the peak in quasi-mono-energetic spectrum has a non-negligible FWHM. The uncertainty of this neutron energy determination comes from fitting this peak by normal distribution:

$$f(x) = \frac{1}{\bar{\sigma}\sqrt{2\pi}} exp\left(-\frac{(x-\mu)^2}{2\bar{\sigma}^2}\right), \tag{4.13}$$

where the measured cross-sections match with the neutron energy μ with the uncertainty $\bar{\sigma}$. The uncertainty of neutron energy determination is usually smaller than 5%. This uncertainty can by larger for lower energy of quasi-mono-energetic spectrum, which has larger peak FWHM and therefore larger uncertainty. Another contribution to uncertainties is the uncertainty of nuclear data libraries. [92]

In the case of reactor measurements, there were many years of research and experiments carried out by my colleagues to determine the reactor neutron spectrum not only in LR-0 reactor, but also in VR-1 reactor. The spectra are calculated and those calculations were validated by the experiments ([83], [45], [43], [72]). Additionally during the SACS measurement, for the neutron flux monitoring the foils of Au and Ni were used, because their cross-sections are well known and have low cross-section uncertainties, because a lot of measurements were made. Therefore, we can consider these values as standardized.

The cross-section uncertainty is determined by differential calculus. If the final result, f, is a differentiable function of several measured quantities (x, y, z, ...), the uncertainty in f relates to the measurement uncertainties according to the equation:

$$\Delta f = |\frac{\partial f}{\partial x}|\Delta x + |\frac{\partial f}{\partial y}|\Delta y + |\frac{\partial f}{\partial z}|\Delta z + ... \tag{4.14}$$

In a special case of:

$$f = \frac{x}{y} \Longrightarrow \Delta f = \frac{1}{y}\Delta x + \frac{x}{y^2}\Delta y \tag{4.15}$$

This uncertainty is determined for each measurement, of which there are dozens.

4.4.2 Statistical uncertainty

As one foil was measured more than once, the final uncertainty was calculated as a standard deviation, which is the dispersion of data values relative to their mean value and it is calculated as the square root of the variance. By using this method, the final uncertainty can be significantly reduced. This reaction rate statistical uncertainty is therefore calculated by the following equation:

$$\Delta\bar{q} = \frac{1}{\sqrt{\sum_{i=1}^{k} \frac{1}{\Delta q(i)^2}}}, \tag{4.16}$$

where $\Delta q(i)$ is a calculated uncertainty of i-th reaction rate and k is a number of measurement of one sample. $\bar{q}$ is the mean value of q.

It is also important to mention that a number of experiment quantities (detector efficiency, neutron flux, gamma line intensity, etc.) are the same for all measurements and this part of the uncertainties does not decrease.

Conclusion

The main task was to use the synergy between the measurement of integral effective cross-sections, using reactors as neutron source, and differential effective cross-sections, using neutron sources based on accelerators. In this thesis the study of both reaction cross-sections, which are important for advanced nuclear systems, was described, and thus the main goal of this work was fulfilled. This is the reason, why the experiments were performed not only in the neutron spectrum of a nuclear reactor, where spectral averaged cross-sections up to 20 MeV are experimentally measured, but also some experiments were performed in the neutron spectrum of accelerator as well.

In my doctoral thesis I not only summarise the methodology of two independent methodologies of cross-sections measurements in the reactor and the accelerator spectra, but I also bring some new data and I thus connect these two so far independently working groups of researchers. Additionally my research also results in new findings, which includes the verification of the SACS measurement methodology in a reactor with more enriched fuel. It proved that a wide range of different reactors can be used for these purposes in the case of a known neutron spectrum, regardless of the fuel enrichment. This hypothesis was further developed and verified by my colleagues. [79] [44] [48]

The methodology in this work builds on my previous work during my bachelor and master studies and has been gradually developed into new findings and conclusions and has brought new cross-sections data that are important for the validation of nuclear data libraries. Many experiments have been carried out during many years of my research in this field. Many experiments were preceded by the measurement of the cross-sections themselves, such as research into the characterization of the HPGe detector, and the characterization of the neutron field of research reactors.

The nuclear data library IRDFF-II is the latest data library and addresses neutron dosimetry needs for fission and fusion applications for incident neutron energies up to 60 MeV [99]. It corresponds the best to the measured SACS result, so it is mostly used in calculations.

During my doctoral research it was proved that even 5 % of the ^{238}U(n,f) fission neutrons in the LR-0 reactor spectrum does not have a significant influence on the ^{235}U SACS measurement. Additionally I measured samples in accelerator spectrum and determined some differential cross-sections. Mainly for the sample of Cu, which was not measured previously in the energy range above 20 MeV. I brought some new experience and recomendations for next improvements especially for ^{63}Cu(n,α)^{60}Co reaction and ^{63}Cu(n,2n)^{62}Cu methodology which I used with my colleagues during measurements in reactor spectrum. In an EXFOR database it can be also seen, that there are no data above 20 MeV of incident energy. So the first experiment with the neutron energy of 23.3 MeV brought new data for the ^{63}Cu(n,α)^{60}Co reaction. The measurement of this reaction was complicated due to the contamination by ^{60}Co and also the need of very long measurement of not only the Cu sample, but also the background to subtract the detector contamination. The measurement of the ^{63}Cu(n,2n)^{62}Cu reaction needs faster measurements after the irradiation to monitor the decay curve. Due to the

fact that more samples were irradiated during both experiments, it was impossible to measure the precise decay curve of Cu without loosing activation of the other samples. So this could be the recommendation for following experiments, that less samples should be irradiated. Then the Cu sample can be measured more precisely.

As can be seen from my result figures, some new data in the case of differential cross-sections was obtained and some data complemented and enriched the existing ones and thus they can serve to refine nuclear data libraries. Those latest results in the neutron field of accelerator described in this doctoral thesis, have not been published yet. In the case of spectrum averaged cross-sections, my experimental data from VR-1 reactor spectrum were published [43] and are already a part of the EXFOR database (see Figure 4.26). Based on my VR-1 results, the new experiments in this reactor field to validate those results, can be performed. My colleagues from reactor research already performed some additional measurements and they followed up on my VR-1 experiment. They also tried to measure SACS in the field of LVR-15 reactor, where the neutron spectrum is much more complicated due to the fuel burn up. In the field of cross-sections measurements, it could be interesting to carry out more experiments in this more complicated reactor neutron field since there is not much experience at all.

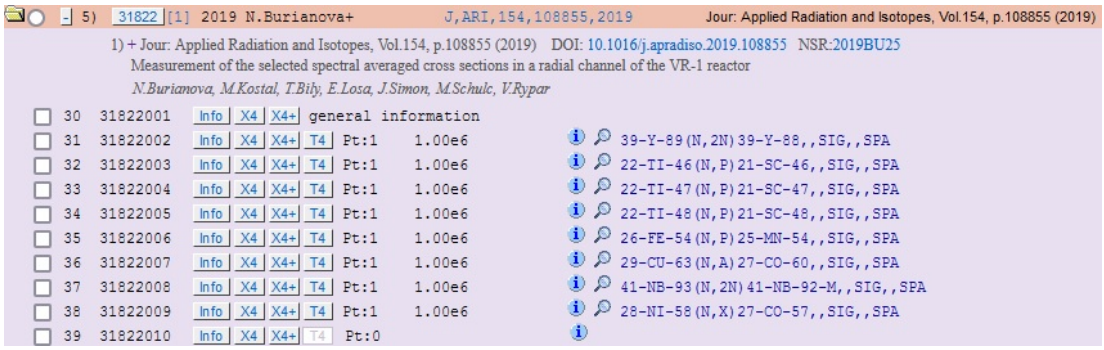

Figure 4.26: My ^{235}U SACS results from VR-1 experiment in EXFOR database. [7]

Other experiments in this field are still ongoing not only in accelerator neutron spectra, but also in nuclear reactor spectra. Due to the fact, that even during the experimentally obtained cross-sections, the data from nuclear data libraries are needed, several experiments are required to evaluate, refine and validate nuclear data libraries. Those data can than be used as an input for simulations of advanced nuclear system projects.

Bibliography

[1] A. Plompen et al. “The NEA High Priority Nuclear Data Request List for future needs”. In: *International Conference on Nuclear Data for Science and Technology, Nice, France, 22-27 April 2007* (2008), pp. 765–768. DOI: doi.org/10.1051/ndata:07419.

[2] T. Smith et al. “The OECD Nuclear Energy Agency Request List for Nuclear Data”. In: *International Conference on Nuclear Data for Science and Technology, Santa Fe, New Mexico, USA, 26 September-1 October 2004* AIP Conference Proceedings 769 (2005), pp. 545–548. DOI: dx.doi.org/10.1063/1.1945067.

[3] Nicola Burianová. “Cross section measurement in reactor spectrum: 55Mn (n,2n), 90Zr(n,2n), 127I(n,2n)”. Master thesis. Faculty of Mathematics and Physics, Charles University, Prague, 2018, p. 51.

[4] M. Allibert et al. *7 - Molten salt fast reactors*. Ed. by Igor L. Pioro. Woodhead Publishing Series in Energy. Woodhead Publishing, 2016, pp. 157–188. ISBN: 978-0-08-100149-3. DOI: https://doi.org/10.1016/B978-0-08-100149-3.00007-0. URL: https://www.sciencedirect.com/science/article/pii/B9780081001493000070.

[5] Michal Košťál and Evžen Losa. “Impact of reactor neutron spectrum on measured spectrum averaged cross sections”. In: *Annals of Nuclear Energy* 74 (2022), pp. 242–263. URL: https://doi.org/10.48550/arXiv.2306.02835.

[6] Ivan A. Kodeli and Aljaž Čufar. “Validation of DT source term modelling in MCNP and MCUNED codes against SINBAD fusion benchmarks”. In: *Fusion Engineering and Design* 154 (2020), p. 111542. ISSN: 0920-3796. DOI: https://doi.org/10.1016/j.fusengdes.2020.111542. URL: https://www.sciencedirect.com/science/article/pii/S0920379620300909.

[7] N. Otuka et al. “Towards a More Complete and Accurate Experimental Nuclear Reaction Data Library (EXFOR): International Collaboration Between Nuclear Reaction Data Centres (NRDC)”. In: *Nuclear Data Sheets* 120 (2014), pp. 272–276. ISSN: 0090-3752. DOI: https://doi.org/10.1016/j.nds.2014.07.065. URL: https://www.sciencedirect.com/science/article/pii/S0090375214005171.

[8] M.B. Chadwick et al. “ENDF/B-VII.1 Nuclear Data for Science and Technology: Cross Sections, Covariances, Fission Product Yields and Decay Data”. In: *Nuclear Data Sheets* 112.12 (2011). Special Issue on ENDF/B-VII.1 Library, pp. 2887–2996. ISSN: 0090-3752.

[9] A.J. Koning et al. “Status of the JEFF Nuclear Data Library”. In: *Proceedings of the International Conference on Nuclear Data for Science and Technology* Jeju Island, Korea (2010), p. 1057.

[10] K. Shibata et al. “JENDL-4.0: a new library for nuclear science and engineering”. In: *J. Nucl. Sci. Technol.* 48 (2011), pp. 1–30.

[11] Z.G. Ge et al. “The Updated Version of Chinese Evaluated Nuclear Data Library (CENDL-3.1)”. In: *In: Proc. International Conference on Nuclear Data for Science and Technology* (2010). Jeju Island, Korea (April 2010), pp. 26–30.

[12] IAEA. *TENDL*. 2023. URL: https://tendl.web.psi.ch/tendl_2021/tendl2021.html.

[13] IAEA. *TALYS*. 2023. URL: https://nds.iaea.org/talys/.

[14] IAEA. *High Priority Nuclear Data Request List*. 2022. URL: https://www.oecd-nea.org/dbdata/hprl/index.html (visited on 11/28/2022).

[15] IAEA. *Evaluated Nuclear Data File (ENDF)*. URL: https://www-nds.iaea.org/exfor/endf.htm (visited on 2023).

[16] Ministry of Industry and Trade. *Státní Energetická Koncepce*. 2015. URL: https://www.mpo.cz/dokument158059.html.

[17] Kazumi Ikeda et al. “Technology readiness assessment of partitioning and transmutation in Japan and issues toward closed fuel cycle”. In: *Progress in Nuclear Energy* 74 (2014), pp. 242–263. ISSN: 0149-1970. DOI: https://doi.org/10.1016/j.pnucene.2013.12.009. URL: https://www.sciencedirect.com/science/article/pii/S0149197013002497.

[18] Carlo Rubbia et al. *A High Resolution Spallation Driven Facility at the CERN-PS to Measure Neutron Cross Sections in the Interval from 1 eV to 250 MeV: a Relative Performance Assessment*. Tech. rep. Addendum to CERN-LHC-98-002-EET. Geneva: CERN, 1998. URL: https://cds.cern.ch/record/363828.

[19] C.D. Bowman et al. “Nuclear energy generation and waste transmutation using an accelerator-driven intense thermal neutron source”. In: *Nuclear Instruments and Methods in Physics Research Section A: Accelerators, Spectrometers, Detectors and Associated Equipment* 320.1 (1992), pp. 336–367. ISSN: 0168-9002. DOI: https://doi.org/10.1016/0168-9002(92)90795-6. URL: https://www.sciencedirect.com/science/article/pii/0168900292907956.

[20] M Angelone, S Atzeni, and S Rollet. “Conceptual study of a compact accelerator-driven neutron source for radioisotope production, boron neutron capture therapy and fast neutron therapy”. In: *Nuclear Instruments and Methods in Physics Research Section A: Accelerators, Spectrometers, Detectors and Associated Equipment* 487.3 (2002), pp. 585–594. ISSN: 0168-9002. DOI: https://doi.org/10.1016/S0168-9002(02)00399-6.

[21] Arthur E. “Accelerator-Driven Transmutation Technology”. In: *The Los Alamos National Laboratory ADTT Update* No.1 (1994).

[22] Klapisch R. “Accelerator driven systems: an application of proton accelerators to nuclear power industry”. In: *Europhysics News* 31 (2000).

[23] World Nuclear Association. *World Nuclear Association*. 2023. URL: https://world-nuclear.org/information-library/nuclear-fuel-cycle/fuel-recycling/plutonium.aspx.

[24] World Nuclear Association. *Processing of used nuclear fuel*. 2022. URL: https://world-nuclear.org/information-library/nuclear-fuel-cycle/fuel-recycling/processing-of-used-nuclear-fuel.aspx (visited on 2022).

[25] Paul Leon Netter. "Reprocessing of spent oxide fuel from nuclear power reactors". In: 2012. URL: https://api.semanticscholar.org/CorpusID:134510630.

[26] Charles E. Till and Y. I. Chang. "Plentiful energy : the story of the integral fast reactor : the complex history of a simple reactor technoloogy, with emphasis on its scientific basis for non-specialists". In: 2011. URL: https://api.semanticscholar.org/CorpusID:57286288.

[27] INTERNATIONAL ATOMIC ENERGY AGENCY. *Technology Review 2023*. IAEA, 2023.

[28] Hamid Ait Abderrahim. "Realization of a new large research infrastructure in Belgium: MYRRHA contribution for closing the nuclear fuel cycle making nuclear energy sustainable". In: *EPJ Web of Conferences* 246 (2020), p. 00012.

[29] Aït Abderrahim et al. "A multi-purpose fast spectrum research reactor". In: *MYRRHA – Energy Conversion and Management* (2012), pp. 4–10. DOI: 101016/jenconman201202025.

[30] International Atomic Energy Agency. *Status of Accelerator Driven Systems Research and Technology Development*. IAEA-TECDOC-1766. IAEA, 2015, p. 376. URL: https://www.iaea.org/publications/10870/status-of-accelerator-driven-systems-research-and-technology-development.

[31] MYRRHA. *MYRRHA*. 2022. URL: https://myrrha.be/ (visited on 2023).

[32] Nicola Burianová. "Gama spektrometrie v reaktorové fyzice na experimentálním reaktoru LR-0 v Řeži". Bachelor thesis. Faculty of Mathematics and Physics, Charles University, Prague, 2016, p. 72.

[33] M. Ohera. *Uvod do polovodicove gamaspektrometrie*. EnviMO Brno, 2000.

[34] G. Gilmore. *Practical gamma-ray spectrometry. 2nd ed.* Wiley, Hoboken, 2008. ISBN: 9780470861967.

[35] B. R. Martin. *Nuclear and particle physics. 2nd ed.* Wiley, Chichester, 2009. ISBN: 978-0-470-74274-7.

[36] CANBERRA Industries. *Genie 2000 3.1 - Customization Tools Manual*. Meriden, CT 06450, 2006.

[37] Laurie S. Waters et al. "The MCNPX Monte Carlo Radiation Transport Coder". In: *AIP Conference Proceedings* (2007), pp. 81–90. DOI: 101063/12720459.

[38] V. Majer. *Základy jaderné chemie: vysokoškolská příručka. 2. vydání*. SNTL Praha, 1981.

[39] Brookhaven National Laboratory Alejandro Sonzogni NNDC. *Chart of nuclides*. 4.4.2016. URL: http://www.nndc.bnl.gov/chart/.

[40] INTERNATIONAL ATOMIC ENERGY AGENCY. *Applications of Research Reactors*. IAEA Nuclear Energy Series No. NP-T-5.3. IAEA, 2014, p. 97. URL: https://www.iaea.org/publications/10491/applications-of-research-reactors.

[41] IAEA. *RRDB*. 2023. URL: https://www.iaea.org/resources/databases/research-reactor-database-rrdb.

[42] CVŘ. *Research reactor LR-0*. 2023. URL: https://www.cvrez.cz/cs/vyzkum-a-sluzby/provoz-reaktoru/reaktor-lr-0-12066 (visited on 2023).

[43] Nicola Burianova et al. "Measurement of the selected spectral averaged cross sections in a radial channel of the VR-1 reactor". In: *Applied Radiation and Isotopes* 154 (2019), p. 108855. ISSN: 0969-8043.

[44] Michal Kostal et al. "Validation of IRDFF-II library in VR-1 reactor field using thin targets". In: *Annals of Nuclear Energy* 158 (2021), p. 108268. ISSN: 0306-4549. DOI: https://doi.org/10.1016/j.anucene.2021.108268. URL: https://www.sciencedirect.com/science/article/pii/S0306454921001444.

[45] Zdeněk Matěj, Michal Košťál, and Václav Přenosil. "Measurement of fast neutron spectrum in the radial channel of VR-1 research reactor". In: *Radiation Physics and Chemistry* 216 (2023). DOI: 10.1016/j.radphyschem.2023.111369.

[46] Czech Technical University in Prague. *VR-1*. 2022. URL: http://www.reaktor-vr1.cz/en/about-us/vr-1 (visited on 2022).

[47] CVŘ. *Research reactor LVR-15*. 2022. URL: http://reaktory.cvrez.cz/en/research-reactor-lvr-15/ (visited on 2022).

[48] Martin Schulc et al. "Constraining high energy tail of 235U(nth,f) prompt fission neutron spectrum". In: *Applied Radiation and Isotopes* 166 (2020), p. 109313. ISSN: 0969-8043.

[49] Michal Koleska, Ladislav Viererbl, and Milan Marek. "Calibration of spent fuel measurement assembly". In: *Radiation Physics and Chemistry* (2014). DOI: 10.1016/j.radphyschem.2014.03.020.

[50] Michal Koleška, Ladislav Viererbl, and Miroslav Vinš. "Determination of IRT-2M fuel burnup by gamma spectrometry". In: *Applied Radiation and Isotopesy* (2016). DOI: 10.1016/j.apradiso.2015.10.001.

[51] L. Viererbl et al. "Mercury mass measurement in fluorescent lamps via neutron activation analysis". In: *Radiation Physics and Chemistry* 116 (2015), pp. 56–59. DOI: 10.1016/j.radphyschem.2015.03.041.

[52] Michal Koleska, Ladislav Viererbl, and Milan Marek. "Development of the MCNPX model for the portable HPGe detector". In: *Radiation Physics and Chemistry* 104 (2014), pp. 351–354. DOI: 10.1016/j.radphyschem.2014.03.035.

[53] INTERNATIONAL ATOMIC ENERGY AGENCY. *Compact Accelerator Based Neutron Sources*. IAEA-TECDOC-1981 Series. IAEA, 2021, p. 124. URL: https://www.iaea.org/publications/14948/compact-accelerator-based-neutron-sources.

[54] S Pomp. "High-energy quasi-monoenergetic neutron fields: existing facilities and future needs". In: *Radiation protection dosimetr* 161 (2014), pp. 1–4. DOI: 10.1093/rpd/nct259.

[55] A. Krása et al. "Neutron production in a Pb/U-setup irradiated with 0.7 –2.5GeV protons and deuterons". In: *Nuclear Instruments and Methods in Physics Research Section A: Accelerators, Spectrometers, Detectors and Associated Equipment* 615.1 (2010), pp. 70–77. ISSN: 0168-9002.

[56] Raffaele Esposito and Marco Calviani. "Design of the third-generation neutron spallation target for the CERN's $n_TOF facility$". In: *Journal of Neutron Research* 22 (2020), pp. 221–231. DOI: 10.3233/JNR-190137.

[57] H. Abele et al. "Particle physics at the European Spallation Source". In: *Physics Reports* 1023 (2023). Particle Physics at the European Spallation Source, pp. 1–84. ISSN: 0370-1573. DOI: https://doi.org/10.1016/j.physrep.2023.06.001. URL: https://www.sciencedirect.com/science/article/pii/S0370157323001898.

[58] ÚJF AV ČR. *Experimentální zařízení - Cyklotron U-120M*. 2022. URL: http://www.ujf.cas.cz/cs/vyzkum-a-vyvoj/experimentalni-zarizeni/ (visited on 2022).

[59] F. Křížek et al. "Irradiation setup at the U-120M cyclotron facility". In: *Nuclear Instruments and Methods in Physics Research Section A: Accelerators, Spectrometers, Detectors and Associated Equipment* 894 (2018), pp. 87–95. ISSN: 0168-9002. DOI: https://doi.org/10.1016/j.nima.2018.03.066.

[60] W. Mannhart. "Evaluation of the Cf-252 Fission Neutron Spectrum Between 0 MeV and 20 MeV". In: *Properties of Neutron Sources, IAEA TEC DOC-410* (1987), pp. 158–170.

[61] Martin Schulc et al. "Application of 252Cf neutron source for precise nuclear data experiments". In: *Applied Radiation and Isotopes* 151 (2019), pp. 187–195. ISSN: 0969-8043.

[62] Martin Schulc et al. "Validation of differential cross sections by means of 252Cf spectral averaged cross sections". In: *Applied Radiation and Isotopes* 132 (2018), pp. 29–37. ISSN: 0969-8043.

[63] Martin Schulc et al. "Spectrum averaged cross section measurements of lutetium using standard 252Cf neutron source". In: *Applied Radiation and Isotopes* 188 (2022), p. 110378. ISSN: 0969-8043.

[64] Martin Schulc et al. "Methodology of 63Cu(n,2n)62Cu Reaction Rate Measurement". In: *Journal of Nuclear Engineering and Radiation Science* 7.2 (2020), p. 024503. ISSN: 2332-8983. DOI: 10.1115/1.4048236.

[65] Martin Schulc et al. "Measurement of very high threshold reactions using 252Cf source". In: *Applied Radiation and Isotopes* 166 (2020), p. 109355. ISSN: 0969-8043.

[66] Qingfei Zhao, Qingquan Pan, and Jinbiao Xiong. “Neutron spectrum optimization for Cf-252 production based on key nuclides analysis”. In: *Radiation Physics and Chemistry* 214 (2023). DOI: 10.1016/j.radphyschem.2023.111294.

[67] Xiaobo Liu, Yaru Shi, and Jiansheng Li. “Time-dependent multiplicity for Cf-252 neutron source”. In: *Applied Radiation and Isotopes* (2023). DOI: 10.1016/j.apradiso.2023.110836.

[68] R.G. Helmer K. Debertin. *Gamma- and X-Ray Spectrometry with Semiconductor Detectors*. North-Hollan, 1988.

[69] M.J. A de Voigt H. Ejiri. *Gamma-Ray and electron spectroscopy in nuclear physics*. Clarendon Press Oxfordn, 1989.

[70] Glenn F. Knoll. *Radiation detection and measurement (third edition)*. John Wiley Sons, 1999.

[71] Vladimír Hnatowicz. *Handbook of Nuclear Data for Neutron Activation Analysis (vol. 1 – Evaluation of Gamma-ray Spectra)*. Nuclear Information Centre, 1986.

[72] Michal Košťál et al. “Measurement of various monitors reaction rate in a special core at LR-0 reactor”. In: *Annals of Nuclear Energy* 112 (2018), pp. 759–768. ISSN: 0306-4549. DOI: https://doi.org/10.1016/j.anucene.2017.10.036.

[73] A.E. Richardson and W.W. Sallee. “Coincidence summing corrections for positron emitters in germanium gamma spectrometry”. In: *Nuclear Instruments and Methods in Physics Research Section A: Accelerators, Spectrometers, Detectors and Associated Equipment* 299.1 (1990), pp. 344–348. ISSN: 0168-9002.

[74] E. Tomarchio and S. Rizzo. “Coincidence-summing correction equations in gamma-ray spectrometry with p-type HPGedetectors”. In: *Radiation Physics and Chemistry* 80.3 (2011), pp. 318–323. ISSN: 0969-806X.

[75] Nicola Burianová et al. “Spectral-average cross section validation in LR-0 reactor spectrum of 55Mn(n,2n), 90Zr(n,2n) and 127I(n,2n) reactions”. In: *ANS RPSD 2018-20th Topical meeting of the Radiation Protection Shielding Division of ANS* (2018). Santa Fe, NM (August 26-31, 2018).

[76] Michal Košťál et al. “Validation of zirconium isotopes (n,g) and (n,2n) cross sections in a comprehensive LR-0 reactor operative parameters set”. In: *Applied Radiation and Isotopes* 128 (2017), pp. 92–100. ISSN: 0969-8043.

[77] Nicola Burianová et al. “Measurement of selected differential cross sections in 235U spectrum”. In: *Journal of Nuclear Engineering and Radiation Science* (2019). DOI: 10.1115/1.4042850.

[78] Jonas Boson, Göran Ågren, and Lennart Johansson. “A detailed investigation of HPGe detector response for improved Monte Carlo efficiency calculations”. In: *Nuclear Inst. and Methods in Physics Research, A* 587.2-3 (2008), pp. 304–314. DOI: 10.1016/j.nima.2008.01.062.

[79] Michal Košťál et al. “On similarity of various reactor spectra and 235U prompt fission neutron spectrum”. In: *Applied Radiation and Isotopes* 135 (2018), pp. 83–91. ISSN: 0969-8043. DOI: https://doi.org/10.1016/j.apradiso.2018.01.028.

[80] W. Mannhart. “Validation of differential cross sections with integral data”. In: *IAEA Report INDC(NDS)435* (2002), pp. 59–64.

[81] Zdeněk Matěj et al. “Measurement of fast neutron spectrum in the radial channel of VR-1 research reactor”. In: *Radiation Physics and Chemistry* 216 (2024), p. 111369. ISSN: 0969-806X. DOI: https://doi.org/10.1016/j.radphyschem.2023.111369. URL: https://www.sciencedirect.com/science/article/pii/S0969806X23006151.

[82] Ondrej Huml, Jan Rataj, and Tomas Bily. “Application of MCNP for neutronic calculations at VR-1 training reactor”. In: (2014). Ed. by Array, p. 05103. DOI: 10.1051/snamc/201405103.

[83] Evžen Losa et al. “Validation of the Fast Neutron Field in the Radial Channel of the VR-1 Reactor”. In: *Journal of Nuclear Engineering and Radiation Science* 7.2 (2020), p. 021503. ISSN: 2332-8983.

[84] Tomas Bily et al. “Effect of kinetics parameters on transients calculations in external source driven subcritical VR-1 reactor”. In: *Annals of Nuclear Energy* 123 (2019), pp. 97–109. ISSN: 0306-4549. DOI: https://doi.org/10.1016/j.anucene.2018.09.007.

[85] Nicola Burianova et al. “Measurement of the selected spectral averaged cross sections in a radial channel of the VR-1 reactor”. In: *Applied Radiation and Isotopes* 154 (2019), p. 108855. ISSN: 0969-8043.

[86] Michal Koleška et al. “Determination of IRT-2M fuel burnup by gamma spectrometry”. In: *Applied Radiation and Isotopes* 107 (2016), pp. 92–97. ISSN: 0969-8043.

[87] Jitka Vrzalová et al. “Excitation functions of neutron-induced threshold reactions in Au, Bi, Ta measured using 30–94 MeV quasi mono-energetic neutron sources”. In: *Nuclear Physics A* 1031 (2023), p. 122593. ISSN: 0375-9474. DOI: https://doi.org/10.1016/j.nuclphysa.2022.122593.

[88] Petr Chudoba et al. “Activation Measurements of Cross Sections for Ground and Isomeric States Production in Neutron Threshold Reactions on Y and Au”. In: *Nuclear Science and Engineering* 191.2 (2018), pp. 150–160.

[89] J. Vrzalová et al. “Studies of (n,xn) cross-sections in Al, Au, Bi, Cu, Fe, I, In, Mg, Ni, Ta, Y, and Zn by the activation method”. In: *Nuclear Instruments and Methods in Physics Research Section A: Accelerators, Spectrometers, Detectors and Associated Equipment* 726 (2013), pp. 84–90. ISSN: 0168-9002. DOI: https://doi.org/10.1016/j.nima.2013.05.133.

[90] Jiří Jarošík et al. “Activation cross-section measurement of fast neutron-induced reactions in Al, Au, Bi, Co, F, Na, and Y”. In: *Nuclear Instruments and Methods in Physics Research Section B: Beam Interactions with Materials and Atoms* 511 (2022), pp. 64–74. ISSN: 0168-583X.

[91] Zdeněk Matěj et al. “The methodology for validation of cross sections in quasi monoenergetic neutron field”. In: *Nuclear Instruments and Methods in Physics Research Section A: Accelerators, Spectrometers, Detectors and Associated Equipment* 1040 (2022), p. 167075. ISSN: 0168-9002. DOI: https://doi.org/10.1016/j.nima.2022.167075.

[92] Jiří Járošík. “Studium reakcí důležitých pro pokročilé jaderné systémy”. Master thesis. České vysoké učení technické v Praze, Fakulta jaderná a fyzikálně inženýrská, 2021, p. 112.

[93] Yoshitomo Uwamino et al. “High-energy p-Li neutron field for activation experiment”. In: *Nuclear Instruments and Methods in Physics Research Section A: Accelerators, Spectrometers, Detectors and Associated Equipment* 389.3 (1997), pp. 463–473. ISSN: 0168-9002.

[94] Mitja Majerle et al. “Au, Bi, Co and Nb cross-section measured by quasi-monoenergetic neutrons from p + 7 Li reaction in the energy range of 18–36 MeV”. In: *Nucl. Phys. A* 953 (2016), pp. 139–157.

[95] V. Wagner, M. Suchopár, and J. Vrzalová. “Cross-section studies of important neutron and relativistic deuteron reactions”. In: *Journal of Physics: Conference Series* (2014). ISSN: 1742-6588. DOI: 10.1088/1742-6596/533/1/012052.

[96] NEA. *JANIS*. 2023. URL: https://www.oecd-nea.org/jcms/pl_39910/janis.

[97] Yoshitomo Uwamino et al. “Measurement of Activation Cross Sections by Using p-Be Neutrons of Energy Up to 40 MeV”. In: *Nuclear Data for Science and Technology*. Springer Berlin Heidelberg, 1992, pp. 726–728. ISBN: 978-3-642-58113-7.

[98] C. Konno Y. Ikeda E. T. Cheng and H. Maekawa. “Measurement of Neutron Activation Cross Sections for the 99Tc(n,p)99Mo, 99Tc(n,)96Nb, 99Tc(n,n)95Nb, and 99Tc(n,n)99mTc Reactions at 13.5 and 14.8 MeV”. In: *Nuclear Science and Engineering* 116.1 (1994), pp. 28–34. DOI: 10.13182/NSE94-A21478.

[99] IAEA. *IRDFF*. 2023. URL: https://www-nds.iaea.org/IRDFF/.

List of Figures

List of Tables

List of Abbreviations

ADS	Accelerator Driven System
CAS	Czech Academy of Science
CENDL	Chinese Evaluated Nuclear Data Library
CERN	The European Organization for Nuclear Research
CIELO	Collaborative International Evaluated Library Organization
CSCF	Coincidence summing correction factor
CTU	Czech Technical University in Prague
CVŘ	Research Center Řež
DEP	Double escape peak
ENDF	Evaluated Nuclear Data File
ESS	European Spallation Source
EXFOR	Experimental Nuclear Reaction Data
FEP	Full energy peak
FWHM	full width at half maximum
HLRW	High-level radioactive waste
HPGe	High Purity Germanium
HPRL	High Priority Request List
IAEA	International Atomic Energy Agency
IRDFF	International Reactor Dosimetry and Fusion File
JEFF	Joint Evaluated Fission and Fusion File
JENDL	Japanese Evaluated Nuclear Data Library
LR-0	Experimental light water reactor in Řež
LVR-15	Research reactor in Czech Republic
MC	Monte Carlo
MCA	Multi-Channel Analyser
MCNP	Monte Carlo N-Particle Transport Code
MCNPX	Monte Carlo N-Particle Extended calculation code
MOX	Mixed oxide fuel
MYRRHA	Multi-purpose hybrid research reactor for high-tech applications
NEA	Nuclear Energy Agency
NG-2	Neutron target station connected to the U-120M accelerator in Czech Republic
NODER	Calculation code
NPA	Net Peak Area
NPI CAS	Nuclear Physics Institute of Czech Academy of Science
NRDC	Nuclear Reaction data Centres network
PE	photo-effect
PET	Positron emission tomography
PFNS	Prompt fission neutron spectra
REMIX	Regenerated Mixture fuel
ROSFOND	Russian national library of neutron data
SACS	Spectral average cross-section
SCK CEN	Belgian Nuclear Research Center
SEP	Single escape peak

SF	Spent fuel
TALYS	Software and datasets for the simulation of nuclear reactions
TENDL	TALYS-based evaluated nuclear data library
ToF	Time of Flight method
US	United States of America
U-120M	Izochronous cyclotron in the Czech Republic
VR-1	School training reactor
VVER	Pressurized water reactor
XS	Cross-section

List of publications

Spectral-average cross section validation in LR-0 reactor spectrum of $^{55}Mn(n,2n)$, $^{90}Zr(n,2n)$ and $^{127}I(n,2n)$ reactions. **N. Burianová**, M. Košťál, M. Schulc, J. Šimon, M. Mareček and J. Uhlíř - ANS RPSD 2018 conference, Santa Fe, New Mexico, 20th Topical Meeting of the Radiation Protection & Shielding Division.

Validation of zirconium isotopes (n,g) and (n,2n) cross sections in a comprehensive LR-0 reactor operative parameters set. M. Košťál, M. Schulc, V. Rypar, E. Losa, **N. Burianová**, J. Šimon, M. Mareček and J. Uhlíř - Applied Radiation and Isotopes, 2017, Vol. 128, p. 92-100, ISSN 0969-8043.

Validation of differential cross sections by means of ^{252}Cf spectral averaged cross sections. M. Schulc, M. Košťál, S. Simakov, V. Rypar, D. Harutyunyan, J. Šimon, **N. Burianová**, E. Novák, B. Jánský, M. Mareček and J. Uhlíř - Applied Radiation and Isotopes, 2018, Vol. 132, p. 29-37, ISSN 0969-8043.

Measurement of various monitors reaction rate in a special core at LR-0 reactor. M. Košťál, M. Schulc, J. Šimon, **N. Burianová**, D. Harutyunyan, E. Losa and V. Rypar - Annals of Nuclear Energy, 2018, Vol. 112, p. 759-768, ISSN 0306-4549.

Validation of selected (n,2n) dosimetry reactions in IRDFF-1.05 library. M. Schulc, M. Košťál, R. Capote, E. Novák, J. Šimon, **N. Burianová** and A. Wallner - Applied Radiation and Isotopes, 2019, Vol. 143, p. 132-140, ISSN 0969-8043.

Measurement of the selected spectral averaged cross sections in a radial channel of the VR-1 reactor. **N. Burianová**, M. Košťál, T. Bíly, E. Losa, J. Šimon, M. Schulc and V. Rypar - Applied Radiation and Isotopes, 2019, Vol. 154, p. 108855, ISSN 0969-8043.

Investigation of $^{127}I(n,2n)^{126}I$ and $^{23}Na(n,2n)^{22}Na$ reactions using ^{252}Cf neutron source. M. Schulc, M. Košťál, E. Novák, J. Šimon and **N. Burianová** - ASME J of Nuclear Rad Sci., 2019, Vol. 5, Issue 3, p. 030918, DOI: 10.1115/1.4039774.

A reference neutron field for measurement of spectrum averaged cross sections. M. Košťál, M. Schulc, E. Losa, J.Šimon, **N. Burianová**, E. Novák, M. Mareček, J. Uhlíř, T. Czakoj, V. Rypar, V. Juříček, R. Capote and A. Trkov - Annals of Nuclear Energy, 2020, Vol. 140, p. 107119, ISSN 0306-4549.

Measurement of selected differential cross sections in 235U spectrum. **N. Burianová**, M. Košťál, M. Schulc, J. Šimon, M. Mareček and J. Uhlíř - NERS, 2018, DOI: 10.1115/1.4042850.

Validation of ^{55}Mn(n,2n) and ^{127}I(n,2n) LWR spectrum averaged differential cross sections. **N. Burianová**, M. Košťál, M. Schulc, J. Šimon, M. Mareček and J. Uhlíř - RRFM 2018, European research reactor conference, Munich, Germany, ISBN: 978-92-95064-29-4.

Ratio of spectral averaged cross sections measured in standard ^{252}Cf(sf) and ^{235}U(n_{th},f) neutron fields. M. Schulc, M. Košťál, R. Capote, E. Novák, **N. Burianová** and J. Šimon - EPJ Web of Conferences, 2020, Vol. 239, DOI: 10.1051/epjconf/202023919004.

Neutron field mock-up development for the fluoride salt reactors neutronic research. E. Losa, M. Košťál, T. Czakoj, J. Šimon, **N. Burianová**, V. Juříček and V. Rypar - EPJ Web of Conferences, 2021, Vol. 247, DOI: 10.1051/epjconf/202124708013.

Activation cross-section measurement of fast neutron-induced reactions in Al, Au, Bi, Co, F, Na and Y. J. Járošík, V. Wagner, P. Chudoba, M. Štefánik, M. Majerle and **N. Burianová** - Nuclear Instruments and Methods in Physics Research Section B: Beam Interactions with Materials and Atoms, 2022, Vol. 511, p. 64-74, ISSN 0168-583X.

A. Attachments

A.1 Reaction rate equation derivation

Differencial equation

$$\frac{dN}{dt} = qN_0 - \lambda N \tag{A.1}$$

describes the change in number of radioactive isotopes N in a given sample with a total number of atoms N_0, which are exposed to the neutron flux density causing the reaction rate per one atom q. λ is the decay constant. By converting this equation of the number of nuclei of the radioactive isotope on its activity and solwing this equation, we obtain

$$A = qN_0(1 - e^{-\lambda t}). \tag{A.2}$$

This radionuclide is subject to radioactive decay, where γ radiation with characteristic energy for the given isotope is emitted. This γ radiation is detected by HPGe detector. The whole photon energy is absorbed in detector during photo effect (PE). This energy is detected in PE peak in gamma spectrum of the HPGe detector. The expected number of gamma pulses $C(E_\gamma)$ with the E_γ energy in PE peak is then

$$C(E_\gamma) = \epsilon_{PEP} I_\gamma \int_0^{t_{real}} A_0 e^{-\lambda t_\Delta} e^{-\lambda t} dt = \epsilon_{PEP} I_\gamma A_0 e^{-\lambda t_\Delta} \frac{1 - e^{-\lambda t_{real}}}{\lambda}, \tag{A.3}$$

where ϵ_{PEP} is the detector system efficiency for PE peak for the given energy and geometry, I_γ is the gamma peak intensity for one decay, A_0 is the isotope activity at the and of the irradiation, t_Δ is the time between the end of irradiation and the start of the detector measurement and t_{real} is the real time of the detector measurement. Measuren number of pulses in PE peak is

$$C(E_\gamma) = S(E_\gamma)\frac{t_{real}}{t_{live}} - C_{bgr} \tag{A.4}$$

where $\frac{t_{real}}{t_{live}}$ represents the correction to detector dead time and C_{bgr} is the peak background. The combination of equations A.2, A.3 and A.4 and using $A_0 = qN_0(1 - e^{-\lambda t_{irr}})$ we can get the final reaction rate equation

$$q = \frac{(S(E_\gamma)\frac{t_{real}}{t_{live}} - C_{bgr})\lambda}{\epsilon_{PEP} I_\gamma N_0 (1 - e^{-\lambda t_{irr}}) e^{-\lambda t_\Delta} 1 - e^{-\lambda t_{real}}}. \tag{A.5}$$

A.2 Python input for cross-sections results plot

```
import matplotlib.pyplot as plt

fig, ax = plt.subplots(figsize=(8,5))
energyTalys = []
fluxTalys = []
energyENDF = []
fluxENDF = []
energy = []
flux = []
err = []
energyexfor = []
fluxexfor = []
errexfor = []
energyIRDFF = []
fluxIRDFF = []

with open("Au(n,2n)_talys.txt","r") as f:
     lines = f.readlines()
for line in lines:
        x, y  = line.strip().split()
        energyTalys.append(float(x))
        fluxTalys.append(float(y))

with open("Au(n,2n)_ENDF.txt", "r") as f:
    lines = f.readlines()
for line in lines:
        j, k = line.strip().split()
        energyENDF.append(float(j))
        fluxENDF.append(float(k))

with open("Au(n,2n)_IRDFF.txt", "r") as f:
    lines = f.readlines()
for line in lines:
        f, h = line.strip().split()
        energyIRDFF.append(float(f))
        fluxIRDFF.append(float(h))


with open("Au(n,2n)_exp.txt", "r") as f:
    lines = f.readlines()
for line in lines:
        s, l, m = line.strip().split()
        energy.append(float(s))
        flux.append(float(l))
        err.append(float(m))

with open("Au(n,2n)_EXFOR.txt", "r") as f:
    lines = f.readlines()
for line in lines:
```

```
        a, b, c = line.strip().split()
        energyexfor.append(float(a))
        fluxexfor.append(float(b))
        errexfor.append(float(c))

for label in (ax.get_xticklabels() + ax.get_yticklabels()):
    label.set_fontsize(13)
plt.plot(energyTalys, fluxTalys, c = "g", linestyle='solid', linewidth=2, label='Talys')
plt.plot(energyENDF, fluxENDF,  linestyle='solid', c = "b", label='ENDF/B-VIII.0')
plt.plot(energyIRDFF, fluxIRDFF,  linestyle='solid', c = "orange", label='IRDFF-II')
plt.errorbar(energyexfor, fluxexfor, yerr = errexfor, fmt = '+',c = "black", label='EXFOR')
plt.errorbar(energy, flux, yerr = err, fmt = '+',c = "r", label='Experiment')
plt.xlabel('Energy [MeV]', fontsize=13)
plt.ylabel('Cross section [b]', fontsize=13)
plt.xlim((0,35))
ax.legend()
plt.show()
```

A.3 TALYS output example

```
# header:
#   title: Cu0(n,x)Cu62 cross section
#   source: TALYS-2.0
#   user: Arjan Koning
#   date: 2024-01-31
#   format: YANDF-0.1
# target:
#   Z: 29
#   A: 0
#   nuclide: Cu0
# reaction:
#   type: (n,x)
#   ENDF_MF: 6
#   ENDF_MT: 5
# residual:
#   Z: 29
#   A: 62
#   nuclide: Cu62
# datablock:
#   quantity: cross section
#   columns: 2
#   entries: 142
##        E              xs
##     [MeV]           [mb]
   1.000000E-01   0.000000E+00
   2.000000E-01   0.000000E+00
   3.000000E-01   0.000000E+00
   4.000000E-01   0.000000E+00
   5.000000E-01   0.000000E+00
   6.000000E-01   0.000000E+00
   7.000000E-01   0.000000E+00
   8.000000E-01   0.000000E+00
   9.000000E-01   0.000000E+00
   1.000000E+00   0.000000E+00
   1.100000E+00   0.000000E+00
   1.200000E+00   0.000000E+00
   1.300000E+00   0.000000E+00
   1.400000E+00   0.000000E+00
   1.500000E+00   0.000000E+00
   1.600000E+00   0.000000E+00
   1.700000E+00   0.000000E+00
   1.800000E+00   0.000000E+00
   1.900000E+00   0.000000E+00
   2.000000E+00   0.000000E+00
   2.100000E+00   0.000000E+00
   2.200000E+00   0.000000E+00
   2.300000E+00   0.000000E+00
   2.400000E+00   0.000000E+00
   2.500000E+00   0.000000E+00
```

```
   2.600000E+00   0.000000E+00
   2.700000E+00   0.000000E+00
   2.800000E+00   0.000000E+00
   2.900000E+00   0.000000E+00
   3.000000E+00   0.000000E+00
   3.100000E+00   0.000000E+00
   3.200000E+00   0.000000E+00
   3.300000E+00   0.000000E+00
   3.400000E+00   0.000000E+00
   3.500000E+00   0.000000E+00
   3.600000E+00   0.000000E+00
   3.700000E+00   0.000000E+00
   3.800000E+00   0.000000E+00
   3.900000E+00   0.000000E+00
   4.000000E+00   0.000000E+00
   4.100000E+00   0.000000E+00
   4.200000E+00   0.000000E+00
   4.300000E+00   0.000000E+00
   4.400000E+00   0.000000E+00
   4.500000E+00   0.000000E+00
   4.600000E+00   0.000000E+00
   4.700000E+00   0.000000E+00
   4.800000E+00   0.000000E+00
   4.900000E+00   0.000000E+00
   5.000000E+00   0.000000E+00
   5.100000E+00   0.000000E+00
   5.200000E+00   0.000000E+00
   5.300000E+00   0.000000E+00
   5.400000E+00   0.000000E+00
   5.500000E+00   0.000000E+00
   5.600000E+00   0.000000E+00
   5.700000E+00   0.000000E+00
   5.800000E+00   0.000000E+00
   5.900000E+00   0.000000E+00
   6.000000E+00   0.000000E+00
   6.100000E+00   0.000000E+00
   6.200000E+00   0.000000E+00
   6.300000E+00   0.000000E+00
   6.400000E+00   0.000000E+00
   6.500000E+00   0.000000E+00
   6.600000E+00   0.000000E+00
   6.700000E+00   0.000000E+00
   6.800000E+00   0.000000E+00
   6.900000E+00   0.000000E+00
   7.000000E+00   0.000000E+00
   7.100000E+00   0.000000E+00
   7.200000E+00   0.000000E+00
   7.300000E+00   0.000000E+00
   7.400000E+00   0.000000E+00
   7.500000E+00   0.000000E+00
   7.600000E+00   0.000000E+00
```

```
   7.700000E+00   0.000000E+00
   7.800000E+00   0.000000E+00
   7.900000E+00   0.000000E+00
   8.000000E+00   0.000000E+00
   8.100000E+00   0.000000E+00
   8.200000E+00   0.000000E+00
   8.300000E+00   0.000000E+00
   8.400000E+00   0.000000E+00
   8.500000E+00   0.000000E+00
   8.600000E+00   0.000000E+00
   8.700000E+00   0.000000E+00
   8.800000E+00   0.000000E+00
   8.900000E+00   0.000000E+00
   9.000000E+00   0.000000E+00
   9.100000E+00   0.000000E+00
   9.200000E+00   0.000000E+00
   9.300000E+00   0.000000E+00
   9.400000E+00   0.000000E+00
   9.500000E+00   0.000000E+00
   9.600000E+00   0.000000E+00
   9.700000E+00   0.000000E+00
   9.800000E+00   0.000000E+00
   9.900000E+00   0.000000E+00
   1.000000E+01   0.000000E+00
   1.010000E+01   0.000000E+00
   1.020000E+01   0.000000E+00
   1.030000E+01   0.000000E+00
   1.040000E+01   0.000000E+00
   1.050000E+01   0.000000E+00
   1.060000E+01   0.000000E+00
   1.070000E+01   0.000000E+00
   1.080000E+01   0.000000E+00
   1.090000E+01   0.000000E+00
   1.100000E+01   0.000000E+00
   1.110000E+01   2.614165E-01
   1.120000E+01   1.498392E+00
   1.130000E+01   3.059942E+00
   1.140000E+01   6.337717E+00
   1.150000E+01   1.109808E+01
   1.160000E+01   1.799376E+01
   1.170000E+01   2.606163E+01
   1.180000E+01   3.644044E+01
   1.190000E+01   4.728537E+01
   1.200000E+01   6.079430E+01
   1.210000E+01   7.454693E+01
   1.220000E+01   8.891672E+01
   1.230000E+01   1.045893E+02
   1.240000E+01   1.195547E+02
   1.250000E+01   1.359792E+02
   1.260000E+01   1.516431E+02
   1.270000E+01   1.662230E+02
```

```
   1.280000E+01   1.825903E+02
   1.290000E+01   1.970305E+02
   1.300000E+01   2.103749E+02
   1.310000E+01   2.253692E+02
   1.320000E+01   2.381600E+02
   1.330000E+01   2.498414E+02
   1.340000E+01   2.623222E+02
   1.350000E+01   2.736393E+02
   1.360000E+01   2.836538E+02
   1.370000E+01   2.932643E+02
   1.380000E+01   3.033847E+02
   1.390000E+01   3.118374E+02
   1.400000E+01   3.192140E+02
   1.410000E+01   3.274685E+02
   1.420000E+01   3.348985E+02
```

A.4 MCNP detector model example

```
HPGe
c Activation foils
c
c New evaluation of scale factor 1.0162 +-0.026 (from film
   )
c
c coaxial HPGe detector in vertical configuration (Ortec
   GEM35 )
c
c Radiogram made - Cs source 5m from 8.24cm thick HPGe,
   film 1.5mm behind
c
c coaxial HPGe detector in vertical configuration (Ortec
   GEM35 )
c
c ******************************
c
c Experimentally determined parameters     Mean  s
c Crystal radius  ......................  3.003   0.010 cm
c Crystal lenght  ......................  5.525   0.020 cm
c Hole lenght  .........................  4.420   0.035 cm
c Hole radius  .........................  0.482   0.011 cm
c End to cap  ..........................  0.651   0.016 cm
c Cap thickness  .......................  0.143   0.013 cm
c Pin radius  ..........................  0.331   0.024 cm
c Pin cavity radius  ...................  0.222   0.003 cm
c Pin contact lenght  ..................  0.369   0.026 cm
c Gap thickness  .......................  0.480   0.018 cm
c
c Detector end radius  .................  0.4 cm
c Hole end radius  .....................  0.4 cm
c Radius of cap  .......................  4.185   0.011 cm
```

```
c Measured radius of cap   ..............  4.118   0.002 cm
c
c Divergence factor     1.016187778
c
c Dead layer front  0.158   0.003194689
c Dead layer side   0.121   0.003194689
c
c Al thicknes      0.098   0.003 cm
c Out diameter     6.325   0.049 cm
c
c low brace - middle brace      1.950   0.059 cm
c middle brace  - up brace     1.493   0.051 cm
c L brace     0.629   0.033 cm
c th. brace     0.178   0.010 cm
c
c Shielding  5 cm
c Th Pb  0.3 cm
c Th phenolic paper  0.1 cm
c Th Cu
c
c
c 1brace end -0.651 level
c  begin   -1.280 level
c 2brace end -2.773 level
c  begin   -3.402 level
c 3brace end -5.547 level
c  begin   -6.176 level
c
c Box  42 x 42 x 42
c
c Detector end cap center is in centre of midplane [0; 0;
   0]
c
c EG3 geometry position 2 is radially central  2.68 cm from
    end cap
c EG3 geometry position 5 is radially central  5.68 cm from
    end cap
c ... EG3 position X is radially central  X.68 cm from end
   cap
c in this positons 4.7 mm PMMA between source and detector
c
c EG3
c _________________________
c PMMA_PMMA_PMMA_PMMA     |
c PMMA_PMMA_PMMA_PMMA     |  1.6mm
c PMMA_PMMA_PMMA_PMMA     |
c ************************  RADIO NUCLIDE  tl 0.2mm
c PMMA_PMMA_PMMA_PMMA     |
c PMMA_PMMA_PMMA_PMMA     | 1.2mm
c PMMA_PMMA_PMMA_PMMA     |
c ----------------------------------------HPGE END CAP
```

```
c
c EG3 in holder
c -------------------------
c PMMA_PMMA_PMMA_PMMA      |
c PMMA_PMMA_PMMA_PMMA      |  1.6mm
c PMMA_PMMA_PMMA_PMMA      |
c **********************  RADIO NUCLIDE tl 0.2mm
c PMMA_PMMA_PMMA_PMMA      |
c PMMA_PMMA_PMMA_PMMA      | 1.2mm
c PMMA_PMMA_PMMA_PMMA      |
c -------------------------  plate
c PMMA_PMMA_PMMA_PMMA      |
c PMMA_PMMA_PMMA_PMMA      |
c PMMA_PMMA_PMMA_PMMA      |
c PMMA_PMMA_PMMA_PMMA      |
c PMMA_PMMA_PMMA_PMMA      |  3.5 mm PMMA holder of EG3
c PMMA_PMMA_PMMA_PMMA      |
c PMMA_PMMA_PMMA_PMMA      |
c PMMA_PMMA_PMMA_PMMA      |
c PMMA_PMMA_PMMA_PMMA      |
c -------------------------
c                          |
c                          | 22.1 mm void
c                          |
c ----------------------------------------HPGE END CAP
c
c
c
c
c EG3 is placed to detector cap by upper plate
c   thus between foil and detector is 1.2mm of PMMA
c when in distant position .... EG3 is on PMMA plate with
   hole
c in position 2
c End cap - plate = 2.21 cm
c plate botom = 3 mm
c EG3 botom = 1.2 mm
c
c
c
c ************************************
c
c -------------  Dead layer  determination  ---------
c
c measured with 241Am source (more Boson et al. Nuclear
   Instruments and Methods
c in Physics Research A 587 (2008) 304 - 314; Dryak 2006 )
c Mi calculated by MCNP6 Mi_Ge=1.8824; Mi_Al=0.167
c
c LR-0 group results:
c                     Cap
```

```
c                       1.582 mm (weigted over HPGe cap surface)
c                       1.508 mm (averaged)
c
c                       Side
c                       1.212 mm (weigted over HPGe cap surface)
c                       1.219 mm (averaged)
c
c
c
c
c **********************************************
c
c
c ------------------------------------------------
c cell card
c ------------------------------------------------
c
 1 3 -11.35 (1 -8 9 -16 17 -24) (-2:7:-10:15:-18:23) (25) imp:p,e=1 $ Pb
 2 2 -1.25 (2 -7 10 -15 18 -23) (-3:6:-11:14:-19:22) (25) imp:p,e=1 $ Phen.
 3 1 -8.96 (3 -6 11 -14 19 -22) (-4:5:-12:13:-20:21) (25) imp:p,e=1 $ Cu
 4 0 (4 -5 12 -13 20 -21) (25) #16 #18 imp:p,e=1 $ Air in box
c
 5 4 -2.7 -25 26 imp:p,e=1 $ Det. cap
c
c simplified version
c 6 5 -5.3255 (-31 32 43 -44):(-31 -41 -46 48 47) imp:p,e=1 $ detector
c 7 5 -5.3255 (-30 31 43 -44):((-30 44 -40 -45) (31:-44:41:46)) imp:p,e=1 $ insensitive
c
c detail version
 6 5 -5.3255 (-31 32 43 -48):(-31 48 47 -64):(64 -41 -62) :(-61 62 64)
      imp:p,e=1 $ detector
 7 5 -5.3255 (-30 31 43 -64):(-62 41 -40):(-60 61 62 64) imp:p,e=1 $ insensitive
c
 8 0 (-32 33 43 -48):(-47 33) imp:p,e=1 $ air in hole
c 9 1 -8.96 (-33 58 -48):(-47 48 -33)  imp:p,e=1 $ contact pin
 9 1 -8.96 (-33 58 -48 36):(-47 48 -33 36):(-36 49 -47) imp:p,e=1 $ contact pin
 17 0 (-36 58 -48):(-36 48 -49)  imp:p,e=1 $ contact pin spring
c
```

```
c Air crystal to mounting
 10 4 -2.7 (57 -40 35 -34):(34 -55 43 -53):(34 -55 52 -51)
    :(34 -55 50 -40)
      imp:p,e=1 $ Al
 11 4 -2.7 -59 33 57 -56   imp:p,e=1 $ Al ink line
 12 0 (34 -55 57 -43):(34 -55 53 -52):(34 -55 51 -50) imp:p
    ,e=1 $ air braces
 13 0 (56 33 -43 -35):(43 -40 30 -35):(62 -30 64 -40 60)
    :(57 -56 59 -35)
     imp:p,e=1 $ air in HPGe
 14 4 -2.7  58 -57 -55 33  imp:p,e=1 $  Al bottom
c
c Air in system
 15 0 (-58:55:40) (-26) imp:p,e=1 $  air inner cap to cap
c
c 16 9 -1.19 -73 imp:p,e=1 $
c
c Marinelka
  16 12 -0.98 ((101 -103 -104):(105 -101 -104 106):
     (103 -107 -102)) imp:p,e=1  $ zdroj
  18 11 -0.9101 (108 -105 -109 110):(105 -101 110 -106)
     :(100 -101 -110):
     (105 -111 104 -109):(111 -103 104 -112):
     (103 -107 102 -112) imp:p,e=1    $ Marinelka
c
 100 0 (-1:8:-9:16:-17:24) imp:p,e=0 $
c
c
c ---------------------------------------------

c ---------------------------------------------
c surface card
c ---------------------------------------------
c Shielded box
c
 1 px -26.4
 2 px -21.4
 3 px -21.1
 4 px -21
 5 px 21
 6 px 21.1
 7 px 21.4
 8 px 26.4
c
 9 py -26.4
 10 py -21.4
 11 py -21.1
 12 py -21
 13 py 21
 14 py 21.1
 15 py 21.4
```

```
 16 py 26.4
c
 17 pz -15.4
 18 pz -10.4
 19 pz -10.1
 20 pz -10
 21 pz 32
 22 pz 32.1
 23 pz 32.4
 24 pz 37.4
c
c 25 cz 4.1205
 25 RCC 0 0 -15 0 0 15 4.118   $ detector cap, top in: (0,
    0, 0)
 26 Rcc 0 0 -14.857 0 0 14.714 3.975
c
c
 30 cz 3.003  $ Crystal radius
 31 cz 2.882  $ Sensitive part of HPGe radius
 32 cz 0.482  $ Hole radius
 33 cz 0.331  $ Pin radius
 34 cz 3.163  $ Inner cap
 35 cz 3.064  $ out cap
 36 cz 0.222  $ hole in pin (avegraged - spring)
c
 40 pz -0.651  $ crystal end (Cap end - End to cap)
 41 pz -0.809  $ sensitive part end (crystal end -
    sensitive part)
 43 pz -6.176  $ crystal begin (crystal end - crystal
    lenght)
 44 pz -1.756  $ hole end (crystal end + hole lenght)
c
c
c cutted edge linearization X=(r*sqrt(2)-r)/cos(45deg)
c r Detector end radius
c
c in this case distance from crystal radius to cut beginn
    2.343mm
c sphere centre 3.026 cm below detector end center
c radius = sqrt(R^2 + (R-X)^2 )
c R Crystal radius
c
c Correction to linearized cut 5.5 %
c Area(neglected) / Area(HPGE
c Area(neglected) = area square - area circle - area cutted
c
c 45 s 0 0 -3.647 4.117
c 46 s 0 0 -3.647 3.977
c
 47 s 0 0 -2.238 0.482 $ hole cut
```

```
 48 pz -2.238  $ hole end (crystal end + hole lenght -
    radius cut)
 49 pz -2.126 $ End of pin contact
c
c
 50 pz -1.280  $ begin up brace  (end with crystal)
 51 pz -2.773  $ end middle brace
 52 pz -3.402  $ begin middle brace
 53 pz -5.547  $ end low brace   (begin with crystal)
c
 55 cz 3.243   $ inner cap brace radius
 56 pz -10.218 $
 57 pz -10.718 $
 58 pz -11.018 $
 59 cz 1.05 $
c
c detail radius model
 60 TZ 0 0 -1.051 2.603 0.4 0.4
 61 TZ 0 0 -1.051 2.603 0.242 0.242 $ insensitive layer in
    cap (=0.1580cm)
c       0; 0; DB-R DR-R  R   R
c DB - Det. begin, R - end det. radius; DR - det. radius
c
 62 cz 2.603
 63 cz 2.482
 64 pz -1.051
 65 pz -1.209
c
c
c
c EG-3 in various positions
c ... EG3 position X is radially central  X.68 cm from end
   cap
c in this positons 4.7 mm PMMA between source and detector
c
c
 70 RCC 0 0 0.01 0 0 0.3 1.25  $ EG-3 on det. surface
 71 RCC 0 0 2.21 0 0 0.6 3     $ EG3 in position 2
 72 RCC 0 0 5.21 0 0 0.6 3     $ EG3 in position 5
 73 RCC 0 0 10.21 0 0 0.6 3     $ EG3 in position 10
 74 RCC 4.13 0 -3 0.3 0 0 1.25 $ EG3 in side position
c
c geometrie marineli
 100 pz 0.01
 101 pz 0.21
 102 cz 7.2
 103 pz 1.61
 104 cz 6.0
 105 pz -6.19
 106 cz 4.5
 107 pz 1.58
```

```
 108 pz -6.39
 109 cz 6.2
 110 cz 4.3
 111 pz 1.61
 112 cz 7.4
c
c
c -----------------------------------------------------

c -----------------------------------------------------
c data card
c -----------------------------------------------------
Mode p e
 F8:p 6
 E8 0 1E-5 1E-3 2198i 2.201
c -----------------------------------------------------
c
 SDEF POS 0 0 0 axs 0 0 1 rad=D1 ext=D2 erg=D4 PAR=2 cell
    =16
c SI1 h 0 0.15
c SP1 d -21 1
c SI2 h 0.121 0.141
c SI2 h 2.68 2.70  $ position 2 cm
c SI2 h 5.68 5.70  $ position 5 cm
c SI2 h 10.68 10.70  $ position 10 cm
c SP2 d -21 0
c SI4 L 0.0595 $
c SP4 D 1
c
c Bocni poloha zdroje
c
c SDEF POS 0 0 0 axs 1 0 0 rad=D1 ext=D2 erg=D4 PAR=2 cell
   =16
c  SI1 h 3 3.18
c  SP1 d -21 1
c SI2 h 4.32 4.34
c SP2 d -21 0
c  SI4 L 0.661 $
c  SP4 D 1
c
c Marinelka
 SI1 0 6.2
 SP1 D -21 1
 SI2 -6.19 2.01 $
 SP2 D -21 0
 SI4 L 0.7955 $
 SP4 D 1
c
c
c  0.0595; 0.122; 0.1365; 0.3917 0.6616; 0.898; 1.173;
   1.332; 1.836
```

```
c ---------------------------------------------------------
c M1 - Cu
c m2 - Phenolic paper
c M3 - Lead
c m4 - Al
c m5 - Ge
c m6 Au(1%)+Al(99%)
c m7 Steel
c m8 - Ni ro= 8.908
c m9 - PMMA ro=1.19
c m11 polypropylene
c m12 silicon rubber (source matrix)
c
c Copper 8.96 g/cm3
c phenolic paper  1.25 g/cm3; Wt. comp. 1000 -0.057444 6000
    -0.774589 8000 -0.167968
c lead 11.35  g/cm3
c
c Compendium of Material Composition Data for Radiation
   Transport Modeling
c PIET-43741-TM-963
c PNNL-15870 Rev. 1
c
c ro=5.3255
c Experimental and MC determination of HPGe detector
   efficiency in the 40 2754 keV
c energy range for measuring point source geometry with the
    source-to-detector distance
c of 25 cm
c
c
c ---------------------------------------------------------
M1 29063 0.6916262
     29065 0.3082671
     47107 0.0000513
     47109 0.0000477
     33000 0.0000027
     79197 0.0000002
     27059 0.0000035
     51121 0.0000007
     51123 0.0000005
m2 6000 7 1000 8 8000 2
m3 82204  -0.014
     82206 -0.241
     82207 -0.221
     82208 -0.524
m4 13027 1
m5 32000 1
c
m6 79000 -0.01
     13000 -0.99
```

```
m7 6000 -0.0042000
        14000 -0.0027000
        15031 -0.0004000
        16032 -0.0004000
        24050 -0.0001669
        24052 -0.0033483
        24053 -0.0003869
        24054 -0.0000981
        25055 -0.0080000
        28058 -0.0026879
        28060 -0.0010710
        28061 -0.0000473
        28062 -0.0001534
        28064 -0.0000403
        29063 -0.0020550
        29065 -0.0009450
        26054 -0.0549466
        26056 -0.8944798
        26057 -0.0210262
        26058 -0.0028473  $ Fe csn12050.1 ro=-7.85
m8 28000 1
m9 6000 5 1000 8 8000 2
m11 6000 2 1000 3
m12 1000 -0.080716 6000 -0.321164 8000 -0.223545 14000
   -0.374575
c
c ---------------------------------------------------------
NPS 1e7
 PRDMP 1e6 1e6 1
 print
 cut:p j 0.01
```